École polytechnique de Louvain

Characterization and enhancement of the indentation and scratch performances of Al/Al_2O_3 nanolaminates

Authors : **Clémentine Houssiau**
Supervisors : **Hosni Idrissi, Thomas Pardoen**
Readers : **Audrey Favache, Jean-Pierre Raskin**
Academic year 2019–2020
Master [120] in Chemical and Materials Engineering

Abstract

The protection of certain materials against erosion is becoming increasingly important. Therefore, many research are currently done to build coatings with enhanced properties which can ensure a good protection of the substrates. In order to produce coatings that can sustain erosion, the goal is to have a combination of high strength and high ductility. This has been achieved through creating hybrid nanolaminates-coatings. In the context of the FNRS project: "Tough hybrid nanolaminates" several systems of crystalline/amorphous nanolaminates are studied. This work focuses on the investigation of the scratch and indentation resistance properties of several Al/Al_2O_3 nanolaminates. A comparison between several systems deposited by magnetron sputtering with various proportion of alumina, and several layers thicknesses was done. The scratch resistance, the critical load under certain loading conditions, the wear volume and the failure mechanisms were determined by a scratch test with a spherical tip of 5μm. The mechanical properties of the different systems such as the hardness and Young modulus were determine through numerical indentation simulation via finite element analysis, with the use of two different tips: spherical and Berkovitch. Due to the low number of experimental samples performed as a result of the corona virus pandemic, the results only allowed to compare general trends of the materials. In all the tests, alumina outperformed the hybrid nanolaminates in terms of scratch resistance, hardness and Young modulus. Furthermore, other tests should be performed to complete the tribological characterization of the materials. Research must go on to measure the properties specific to erosion, in order to produce coatings fitted to their function.

Acknowledgments

Ce mémoire a été difficile à écrire, de par son virage à presque 180° dû à la pandémie de la COVID-19. Je tenais à remercier toutes les personnes qui ont pu m'aider, de près ou de loin, à l'écriture de ce manuscrit.

Merci tout d'abord à mes promoteurs, monsieur Pardoen et monsieur Idrissi, pour leurs remarques toujours pertinentes, et leurs pistes pour adapter ce mémoire aux circonstances particulières.

Ensuite, et même si cette période a été hélas de courte durée, je tenais à remercier les différentes personnes en salle blanche qui ont pris de leur temps pour m'apprendre les différentes manipulations.

Merci aussi à Audrey pour sa formation à l'utilisation du nanoindenteur/nanoscratch et pour ses réponses à mes questions.

Thank you to Hui Wang for his help on making the samples. Thank you for transmitting me the knowledge you had on AJA.

Un immense merci à Paul pour son aide précieuse pour la simulation de l'indentation. Je n'y serais jamais arrivée sans lui, donc merci beaucoup.

Enfin, merci à ma famille, pour son soutien psychologique pendant la période de confinement, et pour sa relecture assidue de mon manuscrit.

Table of contents

List of symbols

Roman letters

A_c	Contact area	m^2
E	Young modulus	GPa
H	Hardness	MPa
h	Penetration depth	m
h_c	Contact depth	m
h_0	Equivalent height of tip defect	m
L_c	Critical load	MPa
m	Strain-rate sensitivity exponent	-
n	Strain-hardening exponent	-
P	Indentation load	MPa
R	Radius of the tip	m
r_c	Radius at the contact depth	m
S	Stiffness	N/m
V	Volume	m^3
W	Work	J

Greek letters

ϵ	Deformation	-
$\dot{\epsilon}$	Deformation rate	s^{-1}
μ	Shear modulus	GPa
ν	Poisson ratio	-
τ	Shear strength	MPa
σ	Stress	MPa
σ_y	Yield stress	MPa

List of Figures

List of Tables

Chapter 1

Introduction

Developing coatings that have specific properties is becoming increasingly important. New applications require more and more specific properties which are hard to achieve. Wind turbine blades for example must sustain high mechanical stresses while having a very light weight. There are some composite materials that meet most of the criteria, but still these blades are very sensitive to erosion by rain and dust winds, reducing their efficiency and durability. The problem can be countered by adding a thin coating to these blades, protecting them from erosion. The purpose of a coating is to improve the surface properties of an object, to enhance its durability. Ceramic-based coatings are often used because of their good corrosion and wear resistance. However, they break easily, compromising their durability. Therefore, many research are currently done to build coatings with enhanced properties which can ensure a good protection of the substrates.

In order to develop effective coatings, it is important to carry out research in this field. This consists of studying the behaviour of different materials, and of different material compositions according to different external stresses.

To have a high-wear resistance coating, the best solution is to have a combination of high strength and high ductility. This has been achieved through creating hybrid nanolaminates-coatings. These are systems composed of two materials of different nature (hybrid), for which a stacking (laminates) of several very small layers (nano) is realized.

Objectives

This master thesis takes place in the context of an FNRS project: "Tough hybrid nanolaminates". It is a four-year project aiming at developing effective coatings through the investigation of the properties of several systems of crystalline/amorphous nanolaminates.

The research presented in this document focuses on one of the systems: Al/Al_2O_3. The goal was initially to characterize this system in terms of scratch and erosion performances, but due to COVID-19 the initial objectives were modified. This document presents the results of the investigation on the scratch and indentation properties of the nanolaminate Al/Al_2O_3. It has two main objectives:

1. The first objective is to determine the composition of the nanolaminate for better scratch resistance. To achieve this goal, a comparison between several systems containing several proportion of alumina, and several layers thicknesses in done.

2. The second objective focuses on the simulation of the indentation properties of the same systems, in order to characterize the hardness and the elastic properties of the different models.

Outline

The outline of this thesis follows the classical structure of scientific articles which is "materials, methods, results and discussion". After this general introduction, chapter two and three set the context and develop the state of the art of methods used to characterize coatings, on the one hand, and the advantages of using nanolaminates, on the other hand. It is then followed by a description of the specific methods which were used in this master thesis to create, and analyse the Al/Al_2O_3 hybrid nanolaminates. The results of the different characterization and simulation done on the samples are then presented and discussed and directions for future research are given. Finally, chapter six gives a conclusion which wraps up the different conclusions obtained in the discussion of the results.

Chapter 2

Coating characterization

2.1 Introduction

The ideal coating is the one that protects the material from external solicitations and that has a high durability. In terms of material properties, that means that researchers try to develop coatings that have high tribological and mechanical performances.

The notions of tribology and mechanical characterization methods will be discussed later in the text, but first, as material parameters are crucial for all methods, it is important to know how to characterize the different properties of coatings. Figure 2.1 shows a classical material stress-strain deformation graph. It shows that the deformation behavior of a material for a given stress can be described by a certain number of parameters.

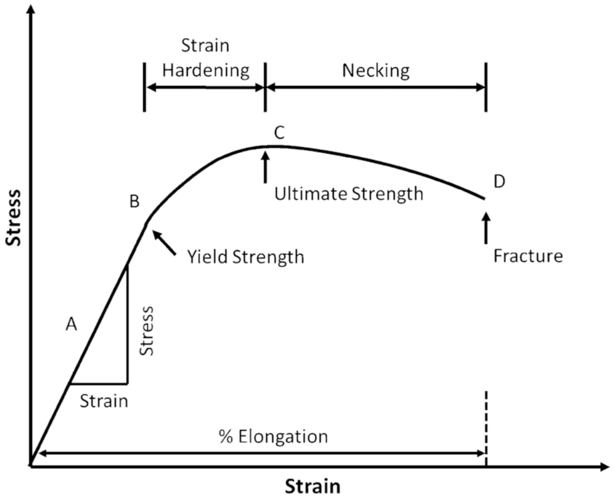

Figure 2.1: Stress-elongation classical curve showing the different tendencies for the evolution of the material properties as a function of the loading [1]

In order to characterize the mechanical properties of coatings, one way is to analyse their response to an external load. Materials have indeed several ways to respond to an external load, as illustrated in Figure 2.2. First, they can be subjected to elastic deformation which allows a reversible deformation of the material when loaded. The atoms are not permanently displaced, and they return back to their original position. It is characterized by its elastic modulus (E [GPa]), which is the slope of the linear (elastic) part of the stress-strain curve.

Secondly, some plastic deformation can be observed, after the yield stress (σ_y [MPa], point B in Figure 2.1) which is the transition between the elastic and the plastic regime. It expresses the

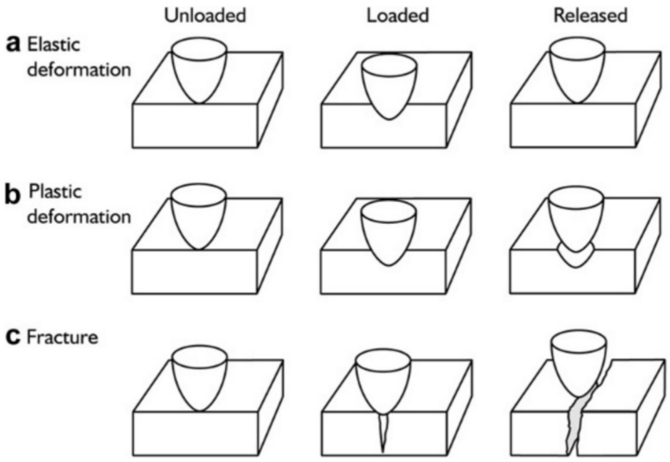

Figure 2.2: Material responses to an external load, as can be seen in indentation and scratch testing [2]

case where the deformation persists after unloading. It happens when the load-induced stress is higher than the yield stress. The material which can not accumulate the stress, will break some bonds between the atoms, and new ones will be created that are as stable as the old ones.

Finally fracture occurs in the material when the stress applied exceeds the material-dependent critical value (a value of the strain which causes fracture in the material, shown by point D in Figure 2.1). It can be caused by tensile stress or by shear stress and can be brittle (nearly no plastic deformation) or ductile (large amount of plastic deformation before crack). It is described by the fracture toughness which is the ability to resist the growth of a pre-existing crack.

If the study of mechanical properties is very well defined, the study of tribological performances is less so. Indeed, tribology is a rather broad field of study. It is the science that studies the contact interaction between two surfaces in relative motion: friction, lubrification and wear. There exist no procedure to obtain reproducible and standard datas in order to have one particular tribological profile for a material (describing all its tribological properties). [3]

In order to asset the durability of a coating, the research presented here focuses on wear. It is a mechanical or chemical damage to a solid surface causing progressive loss of material due to the relative motion between surfaces (or surface/substance). Many types of wear exist: adhesive, abrasive, fatigue, corrosive, erosion, ... Several tests can be made such as scratch, abrasion, and erosion tests in order to characterize the wear behavior of a material.

This chapter describes two very common methods that are used to derive some tribological and mechanical features of coatings. It is divided into three parts:

1. The scratch test, which is a very common method to asses the adhesion between a coating and its substrate.
2. The indentation test, which allows to extract some important mechanical properties such as the hardness and the young modulus.
3. The criterion for a material to enter plasticity are reviewed.

2.2 Scratch

The scratch test is a method allowing to quantify the adhesion of a coating on a substrate, and to identify other mechanisms appearing underneath. It works as a comparison test between several materials, but does not give an intrinsic material property value. In fact, the results depend on the loading parameters, and there are no standard procedure allowing reproducible data. This is partially due to the fact that the phenomena appearing during scratch tests are yet not well known. [4]

The principle of the scratch test is that a diamond tip is scratched over the surface of a material for a certain length, under an increasing loading force, as can be seen in Figure 2.3. The penetration depth at the beginning of the scratch track is then very small, and the tip goes deeper into the material as the loading force increases.

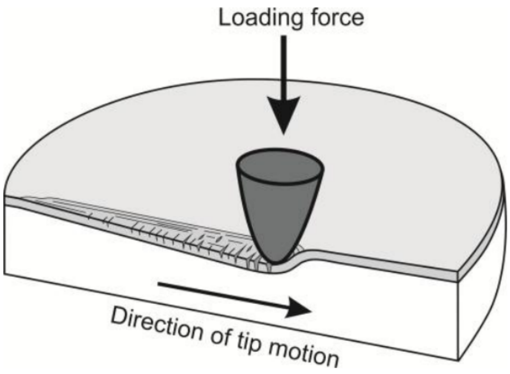

Figure 2.3: Illustration of the scratch principle [5]

2.2.1 Stress field

The phenomena occurring during scratch test are not well known due, among other things, to the complexity of the stress field. In fact, the stress field in the coated surface results from four different effects, as can be seen in Figure 2.4: [6]

1. There are some friction forces between the surface and the tip. Some compression stresses are observed due to the pushing forces in front of the tip and some tension stresses due to pulling forces behind the tip.
2. The configuration of the scratch test brings some deformations (elastic and plastic) which are spherical, groove and torus shaped and result in bending of the coating leading to some compression and tension stresses.
3. The shape of the tip can create some stresses. When a spherical tip is used, some bulk stresses concentration deform the substrate plastically. These deformation are not homogeneous and reach a peak at an angle of 45° from the plane of symmetry of the coating leading to stresses.
4. There are some residual stresses in the coating that result from the deposition of the material of from former loadings.

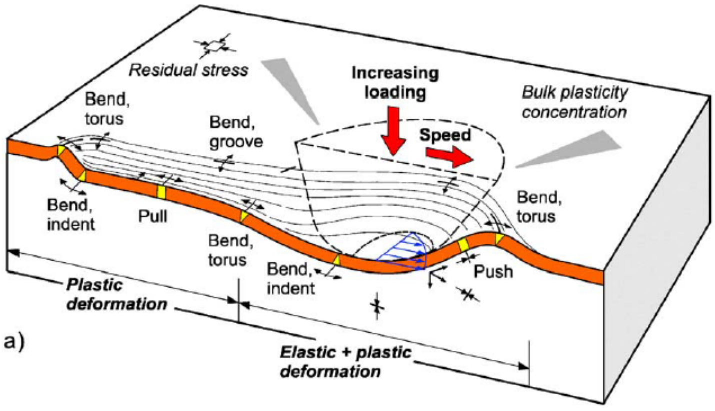

Figure 2.4: Stress field in a coated surface during the scratch test [6]

2.2.2 Critical load

The critical load (L_c) is a measure of the smallest load at which some failure of the coating occurs. It quantifies the mechanical resistance of the interface/coating to all stresses stated above. Above L_c, a lack of adhesion is observed and the load bearing capacity of the coating is lost. [4, 7]

2.2.2.1 Parameters influencing the critical load

The critical load is not an absolute value of a coating and depends on several parameters. These can be placed into two categories: first, the extrinsic parameters are the ones related to the experimental testing part only. The other parameters are called intrinsic parameters and are related to the coating and the substrate themselves. All these parameters have an influence on the interpretation of the critical load and are given in Table 2.1. [7–9]

Table 2.1: Extrinsic and intrinsic parameters that influence the critical load in a scratch test

Extrinsic	Intrinsic
Scratching speed	Substrate/Coating hardness
Loading rate	Coating thickness
Shape and radius of the tip	Coating roughness

2.2.2.2 Measure of the critical load

The critical load can be derived by several methods. The most common one is to observe the changes in the trends of penetration depth as a function of the force applied to the sample in the scratch tracks. These variations can then be confirmed by acoustic emission, and/or by optical or scanning electron microscopy and/or by the variation of friction coefficient. [7]

2.2.3 Failure modes

In order to understand the failure, it is interesting to know which mechanisms are behind it. These mechanisms can be classified into three main categories: cohesive failure, adhesive failure and chipping. Several failure mechanisms may occur during one test. [8, 10, 11].

2.2.3.1 Cohesive failure

Cohesive failure is also called cracking through the thickness. It is due to tensile forces in plane stress which induce cracks in the coating. There are three types of cohesive failure: conformal, tensile and Hertz cracking as can be seen in Figure 2.5.

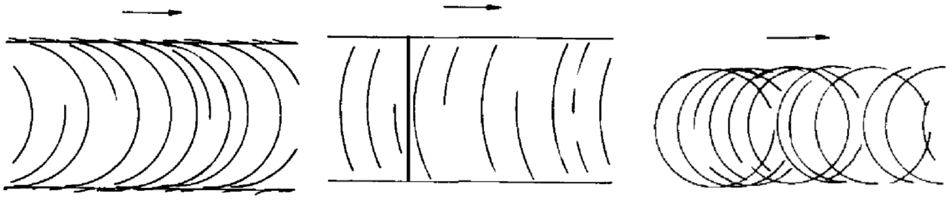

(a) Conformal cracking (b) Tensile cracking (c) Hertz cracking

Figure 2.5: Cohesive failure [12]

1. Conformal cracking (2.5(a)): This type of cracking happens when the coating remains fully adherent to the substrate. The indenter deforms the coating at the same time as the under laying substrate. This creates some tensile bending moments in the coating as pushed by the indenter. It creates cracks in the scratch track with semicircular trajectories that are parallel to the front edge of the tip.
2. Tensile cracking (2.5(b)): It is quite similar to the conformal cracking except that the semicircular cracks are now parallel to the back edge of the tip. It is formed as a result of the tensile frictional stresses that are present behind the trailing edge of the tip that balance the compressive frictional stresses ahead.
3. Hertz (tensile) cracking (2.5(c)): This type of failure mode can be seen in coatings of very brittle substrates. It is the result of a tensile radial stress caused by a normal force on brittle materials. As the indenter moves, several rings are made, and they intercept at the end.

2.2.3.2 Adhesive failure

Adhesive failure is due to compressive forces in plane stress, causing delamination of the coating. There are four types of adhesive failure: gross spallation, compressive spallation, recovery spallation and bucking, as can be seen in Figure 2.6. [11]

1. Gross spallation (2.6(a)): Also known as large area spallation, it happens when there is a total delamination of the coating. It is a sign of poor adhesion or high residual stresses in the coating. It occurs when a crack is formed at the substrate-coating interface which propagates for a long-distance on both sides of the scratch track before coming to a stop.
2. Compressive (wedge) spallation (2.6(b)): It is a very common failure mode. In order to minimize the amount of elastic energy that is stored by the large compressive stress ahead

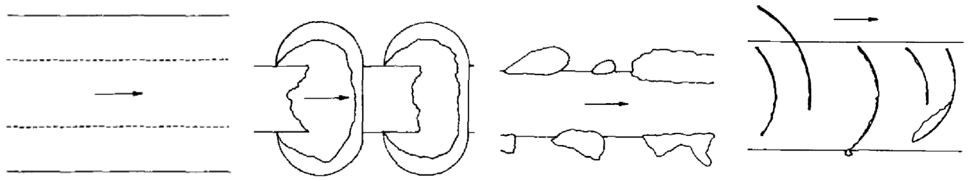

(a) Gross spallation (b) Compressive spallation (c) Recovery spallation (d) Buckling

Figure 2.6: Adhesive failure [12]

the stylus, the coating is detached. It implies then very poor adhesion. The semicircular cracks propagate outwards from the center line of the crack.

3. Recovery spallation (2.6(c)): It happens after loading in a region. It is due to the difference of elasticity between the substrate and the coating. The delimited areas are then along the side of the scratch track.

   It is sometimes hard to distinguish between recovery spallation and compressive spallation, but when the level of residual stress is high, it is more likely to see compressive spallation. [12]

4. Buckling (2.6(d)): It is the result of partial delamination. This gives cracking in roughly semicircular arcs in front of the scratch.

2.2.3.3 Chipping

Chipping is a mechanical phenomenon in which a separation of small, thin pieces of material or coating from their substrate occurs. Some small regions of the coating are removed and stand on the edges of the scratch groove, as illustrated in Figure 2.7.

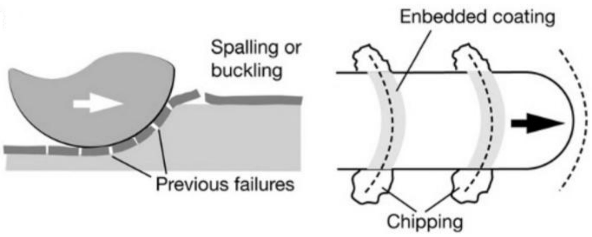

Figure 2.7: Chipping of the coating [2]

Figure 2.8 gives an example of the different failure mechanisms which can be found in the same scratch. It shows the variation of the dynamic stress field concentration at different locations.

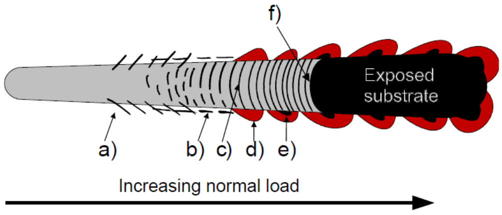

Figure 2.8: Surface crack with different failure mechanisms. (a, b and c) tensile cracking (going from a chevron or angular cracks to transverse semi-circular cracks), (d) coating chipping, (e) coating spalling and (f) exposed-substrate. [6]

2.2.4 Role of the different parameters influencing the type of failure

2.2.4.1 Influence of the hardness of coating/substrate

The failure modes differ depending whether the coating is hard or soft and is on a hard or a soft substrate. The four main cases which can occur are [13] :

1. Soft coating/soft substrate: There is mainly plastic deformation leading to some groove formation on the path of the scratch track. Nearly no cracking is observed, except at very high loads.
2. Hard coating/soft substrate: The substrate contains a lot of plastic deformation, which is felt by the coating that may then crack (due to the bending into the track created by the plastic deformation of the coating).
3. Soft coating/hard substrate: There is some plastic deformation of the coating and not on the substrate so some extrusion occurs between the stylus and the substrate. Thinning of the coating occurs instead of fracture of the substrate.
4. Hard coating/hard substrate: There is nearly no plastic deformation and fracture dominates.

In Figure 2.9 is a comparison between the failure modes that can occur depending of the nature of the substrate/coating.

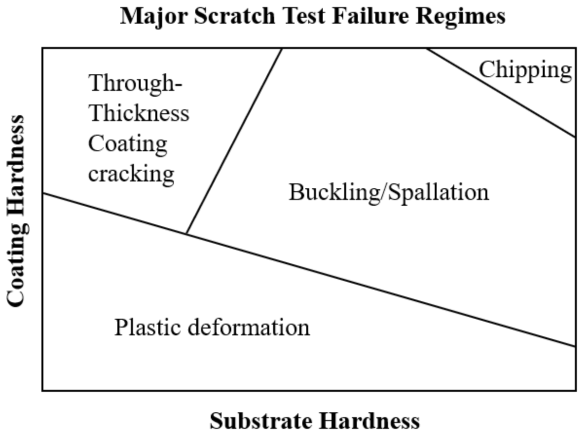

Figure 2.9: Map of the main scratch test failure modes in terms of substrate and coating hardness (reproduced from [8])

2.2.4.2 Influence of the brittle and ductile failure

The failure can be either brittle or ductile, leading to different failure behavior in the coating. Brittle cracking leads to gross, compressive and recovery spallation, and to Hertz and tensile cracking. Ductile failure mode leads to gross spallation, buckling and tensile and conformal cracking. [10, 12]

The type of failure generally depends on the type of substrate. Brittle failure is seen in hard ceramic substrate while more ductile failure is observed in soft ductile substrates. The different decohesion mechanisms (causing adhesion failure) are presented for brittle and ductile substrate in Table 2.2.

Table 2.2: Decohesion mechanisms of a brittle thin film deposited onto different substrates in case of good and poor adhesion (modified from [12])

Stress	Substrate	Good adhesion	Poor adhesion
Tensile	Ductile	Film cracking (no decohesion)	Film cracking (decohesion)
Compressive	Ductile	Buckle propagation (film)	Buckle propagation (interface)
Tensile	Brittle	Film cracking (decohesion)	Edge decohesion (interface)
Compressive	Brittle	Substrate splitting	Buckle propagation (interface)

2.2.4.3 Effect of the thickness of the coating

The thickness of the coating influences its response to an external load. Taking the more general case (which is a hard coating on a soft substrate), buckling failure mode predominates for thin flexible coating while wedge spallation occurs for thicker, stiffer coatings. In most cases, the critical load increases with coating thickness. [9] But the effect of the thickness can also be negative: there may be more tensile stresses at the substrate/coating interface of thicker coatings leading to interface crack and delamination of the coating. [14]

Some parameters that are intrinsic material properties may be more interesting to change than changing the thickness. In fact a stiffer hard coating on a soft substrate has a better load-carrying capacity than a more elastic one. It will accommodate higher tensile stresses at the same indentation depth than a more elastic one. So more importance should be given to improving the elastic properties of the coating because the influence on focusing on the Young modulus can be more effective than changing the coating thickness. [9]

2.2.5 Role of the scratch test on the measurement of the adhesion properties

The strength of the adhesive bonds between the coating and the substrate is crucial for the quality of the coating. If these bonds crack, then some parts of the coating are removed, and the substrate is visible. This failure happens when a crack is formed at the interface between the coating and the substrate and it grows until it merges a vertical-through coating crack. A piece of material is then liberated and removed after the merging of the cracks. The value of this strength can be characterized by the adhesion strength (stress that the interface can withstand without fracturing) which can be obtained by the scratch test. [2, 15]

2.3 Indentation

The indentation test consists of pushing a punch, also called indenter, of known geometry and mechanical properties into a material.

The information provided through nanoindentation are the mechanical properties of thin films such as the Young modulus and the hardness. In this section, the concepts of hardness, Young modulus and contact area are discussed, then some ways to determine them experimentally are given.

2.3.1 Definition of the hardness

The hardness H can be define as the resistance given by a surface to the penetration of a small punch. It is not an intrinsic property as it depends on the loading conditions, but illustrates the behavior of the material to resist to a deformation. It is mathematically written:

$$H = \frac{P}{A_c} \tag{2.1}$$

where P is the load at a given indentation depth, and A_c is the corresponding projected contact area. The difficulty here is to define the projected contact area. Due to the elasticity/plasticity of the materials, a certain penetration depth (h), will not give the same contact depth (h_c) for different materials. This is illustrated for a spherical tip in Figure 2.10. A bad definition of this projected area may lead to overestimation/underestimation of the hardness and the Young modulus. For example, for material having a lot of plastic deformation during indentation, there is a pile-up effect (a small amount of matter that makes a pile next to the indentation zone): when a pile-up is large, the area deduced from analysis of the load displacement curve can underestimates the true contact by up to 60%. [16]

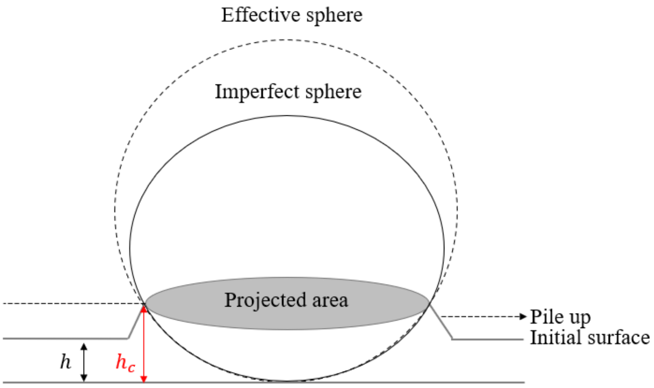

Figure 2.10: Illustration of the projected area for a spherical tip

For a Berkovitch tip, there exists several models to quantify this area: the model of Oliver and Pharr, and the model of Loubet giving some lower and upper boundaries to the contact area. The contact area can be calculated for a perfect conical indenter by:

$$A_c = \pi(tan(\theta)h_c)^2 \tag{2.2}$$

where θ is the equivalent angle of the conical indenter (for a Berkovich tip: $\theta = 90 - \beta = 70.32°$).

Oliver and Pharr This model can be consider as a lower bound of the projected contact area. For materials having a quasi-elastic deformation at contact it states that the total penetration depth can be divided into two parts: the contact depth, and a certain elastic inflexion. This is illustrated in Figure 2.11.

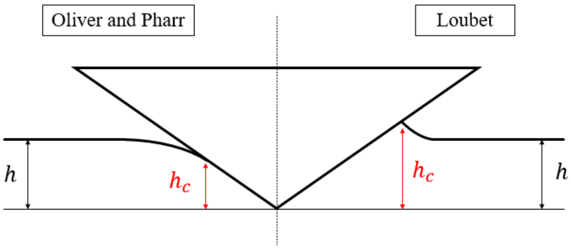

Figure 2.11: Two models representing the lower and upper boundaries of the indentation projected area. On the left image, the elastic inflexion will make the contact area smaller than the total penetration depth. On the contrary, the opposite will be seen in Loubet's model where the pile-ups make h_c bigger than h. (modified from [17])

The total contact depth can be written: [18]

$$h_c = h - \epsilon \frac{P}{S} \tag{2.3}$$

where S is the stiffness of the material and ϵ depends on the geometry of the tip, and is equal to $\epsilon = 0.75$ for a berkovitch tip. The second term of the equation represents the elastic inflexion of the indentation. In order to correct the non-perfect geometry of the indenter, the model proposed a computational projected area:

$$A_c = C_0 h_c^2 + C_1 h_c + ... + C_8 h_c^{1/128} \tag{2.4}$$

Loubet The Loubet's model, takes into account the pile-ups that are made on the edges of the materials. It is a model based on the indentation of a elastic-perfectly plastic solid and is consider as the upper bound for the contact area. It is illustrated in Figure 2.11.

The total contact depth can be written: [19]

$$h_c = \alpha_L (h - \frac{P}{S} + h_0) \tag{2.5}$$

where h_0 is the equivalent height of the tip defect (as shown in Figure 2.12) and α_L had been determined with different experimental simulations, and takes piling-up and sinking-in phenomena into account. The value for a berkovitch tip is α_L=1,2.

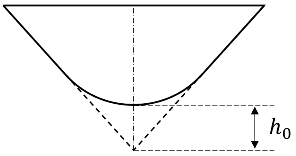

Figure 2.12: Illustration of the h_0 value in Loubet's model

2.3.2 Definition of the Young modulus

The Young modulus does not have a universal definition as there is one for hardness. However, some upper and lower values of the Young modulus for laminates materials (as illustrated in Figure 2.13) have been defined. [20]

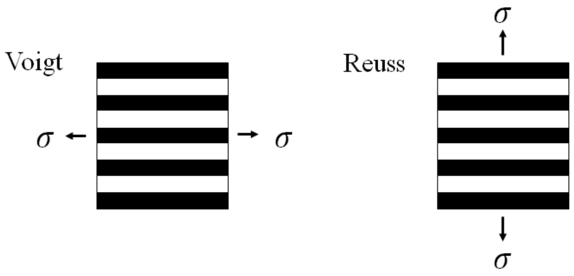

Figure 2.13: Illustration of the two boundary composite models for Young modulus measurement

The Voigt model gives an upper-bound of the Young modulus. It is obtained when the loading is parallel to the composite stacking. A postulate of isostrain is stated, and because the stress is then a volume-average of the local stress, the composite modulus is given by the rule of mixture:

$$E = fE_a + (1 - f)E_b \tag{2.6}$$

where f is the fraction of the material A in the composite, and E$_a$ and E_b are the Young modulus of material A and B respectively.

The Reuss model gives a lower-bound, and is obtained when the loading is perpendicular to the composite stacking. The two compounds carry then the same stress, giving an isostress model. The strain is the volume-average of the local strain giving a composite modulus with the following form:

$$\frac{1}{E} = \frac{f}{E_a} + \frac{1-f}{E_b} \tag{2.7}$$

When the applied forces are perfectly perpendicular/parallel to the modulus, the Reuss/Voigt model will give a perfect value for the composite modulus. In the model used in the case of this master thesis, the compression is neither perfectly perpendicular, neither perfectly parallel, so the resultant composite modulus should between these two models.

2.3.3 Mechanical properties determination

During nanoindentation, a constant measure of the reaction force at the tip, and of the displacement of the tip are done. By plotting the displacement versus the loading (as illustrated in Figure 2.14), several information can be deduced.

First, the hardness is simply measured as the maximal load at a certain penetration depth, divided by the contact area at this hardness.

Secondly, the stiffness can be measured at the onset of unloading. The slope gives the elastic recovery, so the stiffness S can be written: [21]

$$S = \frac{dP}{dh} \tag{2.8}$$

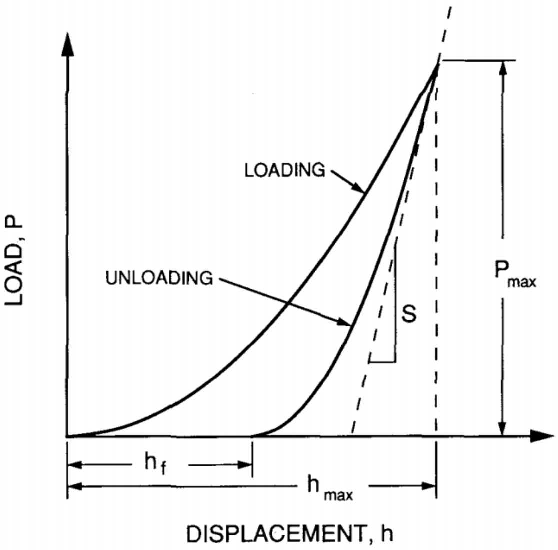

Figure 2.14: Classical plot of indentation results of the displacement vs the load [21]

There is a relation that links stiffness and Young modulus. This allows to measure the Young modulus with:

$$E_{eff} = \frac{1}{\beta}\frac{\sqrt{\pi}}{2}\frac{S}{\sqrt{A_c}} \tag{2.9}$$

where A_c is the projected contact area, E$_{eff}$ is the effective Young modulus and β is a shape factor of the indenter (the indenter geometry-dependent dimensionless parameter). The value of β is 1 for a circular tip and 1.034 for a triangular tip. [18]

Finally, by the mechanic of contacts it can be stated that:

$$\frac{1}{E_{eff}} = \frac{1-v_i^2}{E_i} + \frac{1-v_s^2}{E_s} \tag{2.10}$$

where the index i is related to the indenter, and s is related to the sample analyzed.

2.3.4 Influence of several parameters

2.3.4.1 Influence of the substrate

When measuring the mechanical properties of a film, one common problem is the substrate influence. In fact, when indenting a material at more than 10% of the film thickness, an influence of the substrate is felt, giving a false value of the Young modulus. There exists two ways to avoid this substrate effect: one is to replace the substrate material by an homogeneous material having the rule of mixture of the material properties [22], the other is to use one of the models such as the one listed hereafter. [23]

Hay-Crawford model provides an analytic mean to take into account the substrate influence. It states that the modulus is a function of the measured Young modulus (with the influence of the substrate effect), the film thickness, the Poisson ratio of the film, and the Young modulus and Poisson ratio of the substrate, and it returns a substrate-independent Young modulus of the film. It can be derived by:

$$\frac{1}{E_s} = (1-I_0)\frac{1}{E_{sub} + FI_0E_f} + I_0\frac{1}{E_f} \tag{2.11}$$

where E_s is the Young modulus of the sample found by Equation 2.10, the indices f and sub are related to the film and the substrate respectively, F is an empirical constant (dimensionless), and the function I_0 is the weighting factor for modulus. It can be written as:

$$I_0 = \frac{2}{\pi} arctan(\frac{t}{r_c}) + \frac{1}{2\pi(1-\nu_s)}[(1-2\nu_s)\frac{t}{r_c} ln(\frac{1+(t/r_c)^2}{(t/r_c)^2}) - \frac{t/r_c}{1+(t/r_c)^2}] \qquad (2.12)$$

where t is the effective film thickness (the film thickness minus the penetration contact depth), and r_c is the contact radius.

2.3.4.2 Influence of the tip

There exist several types of indentation tips. These are shown in Figure 2.15. This section discuss the use of two of these tips: the Berkovitch and the spherical tip.

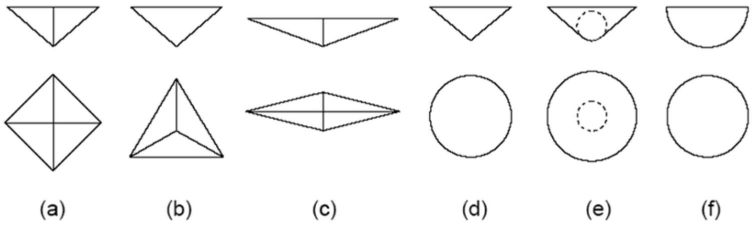

Figure 2.15: Different types of indenter with (a) Vickers, (b) Berkovitch, (c) Knoop (d) conical, (e) nearly conical (Rockwell) and (f) spherical [24]

Berkovitch tip The Berkovitch indenter is the most used tip for indentation. Its configuration gives it interesting properties. It is used for samples where the plastic deformation must be confined on small volume, which is the case for thin films. It has a three side-pyramid structure which allows to maintain a constant ratio "contact diagonal to the depth of penetration" for different penetration loads. This is particularly useful to measure hardness, where the value must be independent of the load.

In practice, the tip will not be perfectly triangular. The indenter has a non-zero tip radius that cannot be neglected. This tip rounding causes hardness to vary with indentation depth. It has been shown that having a larger tip radius and going deeper in the material gives similar effects. In fact, there exist a critical radius to penetration ratio for measuring the hardness of the coatings without this influence, which depends on the properties of the layers and the substrate. [25, 26]

Spherical tip Spherical indenters are mainly used to give information over the transition between the elastic and the plastic regions. In fact, at the beginning of indentation, the deformation is only elastic because the contact stress is initially very small. A transition from elastic to plastic occurs when the spherical tip is driven further into the surface. This transition could be used to measure the yielding of the material and its work hardening.

Its use is however limited due to difficulties to produce perfect spheres. [27]

2.4 Plasticity

In order to know when a material starts deforming plastically, the condition for the onset of plasticity must be defined. In this master thesis, the materials are taken as being isotropic, meaning that the conditions are independent of the orientation. [28]

This sections describes a criterion for the entrance in plasticity of materials, how the materials can harden with the accumulation of plastic deformation, and then describes some common plasticity models.

2.4.1 Von Mises criterion

Several models have been exposed to quantify the onset of plasticity. In isotropic solids, such as metals, the Von-Mises criterion is used, and involves all three principal stresses. To develop this model, a concept that must be introduced in the one of yield surface. It is a five-dimensional surface in the six-dimensional space of stresses. It states that when the stress is located inside the yield surface, then the deformation remains elastic. When the stress state lies on the surface the material is said to have reached its yield point. Further deformation of the material causes the stress state to remain on the yield surface. The expression of Von-Mises yield surface is given by:

$$\bar{\sigma} = \frac{1}{\sqrt{2}}\sqrt{(\sigma_1 - \sigma_2)^2 + (\sigma_2 - \sigma_3)^2 + (\sigma_3 - \sigma_1)^2} \tag{2.13}$$

where $\bar{\sigma}$ is the equivalent stress. The criterion of Von Mises (illustrated in Figure 2.16) can be resumed by stating that when the stress is larger than the equivalent stress, then the material deforms plastically.

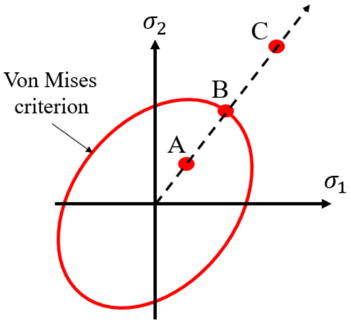

Figure 2.16: Von Mises criterion for plane stress with A, elastic behavior, B on the onset of plasticity and C, plastic behavior

2.4.2 Hardening of a material

With the accumulation of plastic deformation, the yield stress of a material increases, so to deform the material any further, the stress must be increased. The relationship between the plastic strain that is accumulated and the yield stress is called the hardening law of a material, and explains how a material can harden with the plastic flow. The hardening tendency of a material is defined by its strain hardening exponent (n). A strain hardening of n=0 shows an elastic-perfectly plastic behavior while a n=1 shows a perfectly-elastic behavior. For metals it generally ranges between 0.05 and 0.5. A material which has a sensitivity to strain-hardening will have a model on the form:

$$\sigma_y = f(\sigma_0, \epsilon^n) \tag{2.14}$$

A coefficient similar to the one developed for strain hardening can be developed for the average strain sensitivity of a material: m. The yields stress is then in the form of:

$$\sigma_y = f(\sigma_0, \epsilon^n, \dot{\epsilon^m}) \tag{2.15}$$

Figure 2.17 resumes some different situations that may occur in materials.

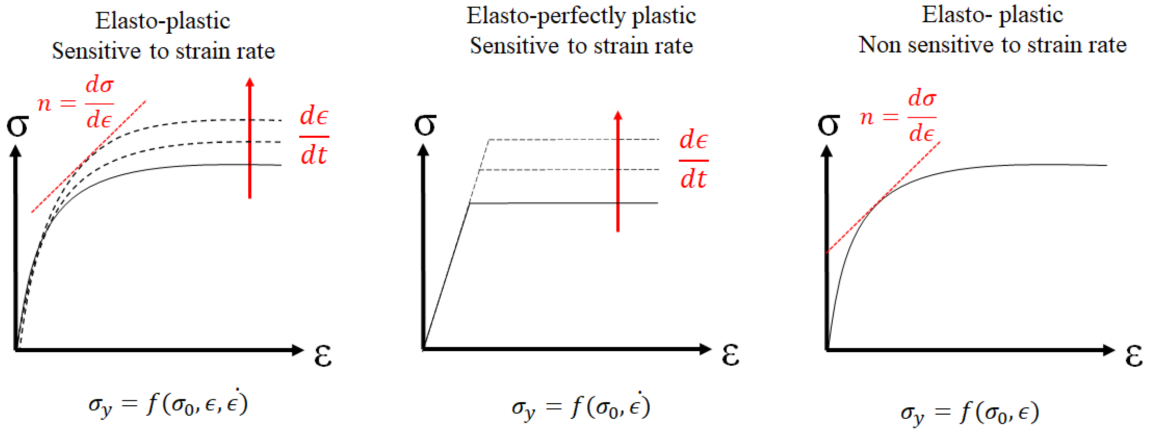

Figure 2.17: Influence on the yield stress of the strain-hardening exponent (n) and the strain-rate hardening exponent (m) for different types of modeled materials

2.4.3 Common plasticity models

There exist several plasticity models which can be used to determine the evolution of the yield stress with an influence of the strain hardening and the strain hardening rate. Some classical models describing the influence of strain-hardening on the yield stress are: [28, 29]

- Ludwig law:

$$\sigma_y = \sigma_0 + \sigma_0 k_L \epsilon^{p^{n_L}} \tag{2.16}$$

- Swift law (generalized power law):

$$\sigma_y = \sigma_0 (1 + k_s \epsilon^p)^{n_s} \tag{2.17}$$

- Voce law:

$$\sigma_y = \sigma_0 [k_1 - (k_2 - 1) exp(-N\epsilon^p)] \tag{2.18}$$

These models can also be used when the materials have a sensitivity to the rate of deformation. In fact, during plastic deformation, dislocations accumulate and the material hardens. The hardening can be quantified by the accumulation of plastic strains (which is the sum of the absolute value of the plastic strain increments). The accumulated stress is given by:

$$\epsilon^p_{acc} = \int |\dot{\epsilon}^p| dt \tag{2.19}$$

By replacing ϵ^p by ϵ^p_{acc} in the different equations, the stress evolution can be related to the total strain hardening evolution, including the influence of the strain-rate sensitivity. This dependence can also be included by modifying the models, as shown in [30].

In practice, many additional plasticity models are used for different purposes. Some of them, used in simulations, are developed in subsection 4.3.2.

Chapter 3

Nanolaminates

3.1 Introduction

The goal followed in this master thesis is to develop a coating that has high strength (capacity to withstand an applied load without plastic deformation/failure), high ductility (capacity to undergo plastic deformation before failure) and high toughness (capacity to plastically deform without fracturing by absorbing energy) properties with a good resistance to wear.

As stated in the introduction, ceramics are good candidates because they have a good corrosion and wear resistance, an enhanced thermal and chemical stability, high flexural strength and hardness. But they are often limited by their brittle behavior. However, having both properties of strength and toughness is essential for many structural materials. Toughness can still be generated in ceramics with extrinsic strategies (such as crack deflection, grain of fiber bridging, ...) which develop fracture resistance, but it is always far from the one of metals. On the contrary, metals are ductile, but their strength is limited compared to the one of ceramics.

It is then not possible to have both the properties of high strength and high ductility in common bulk materials. In fact these two properties are mutually exclusive. [31, 32]

For this reason, scientists have developed some techniques to enhance material properties. They have done it through two ways: mixing materials, and reducing their scale.

Creating composites was already done a long time ago. The earliest reference in improved properties using laminate metals can be found in "The Iliad" of Homer. This story describes Achille's shield as having five layers: bronze/tin/gold/tin/bronze. During his fight, Aenea's spear only penetrated the two first layers but got stucked in the gold layer. Laminates are also found in some Viking blades, Japanese and Chinese swords. [33, 34]

With time, these laminates have been widely studied, and their size has been decreased down to the nanoscale in order to develop new properties.

This chapter reviews the state of the art of nanolaminates. It is divided in two parts:

1. The first part reviews the advantages of thin films by explaining first the properties of crystalline (in the form of metals) and amorphous materials (in the form of metallic glasses) and then their enhancement at the nanoscale.

2. The second part describes the properties of thin films as hybrid materials combining layers of crystalline and amorphous materials.

3.2 Nanoscale

The nanoscale for materials describes materials with a layer thickness of maximum 100 nm. These materials often show very different mechanical properties compared to their bulk form due to their high interfacial area and their dramatically smaller length scale. Some new mechanisms are observed at the nanoscale. [35–37]

3.2.1 Deposition methods

To deposit thin films, some specific techniques have been developed. Two important characteristics of these methods are the achieved coating thickness and deposition temperature. There are wide ranges of techniques. Several classifications exist, either the classical classification which divides the process depending on the state of process (gaseous, solution, molten/semi-molten or solid-state process) [38] or others such as dividing the process whether they are chemical or physical processes. Some of these processes are shown in Figure 3.1. Solid-state methods are not shown in the figure because they tend to produce thicker coatings, and are therefore not relevant when talking about thin films.

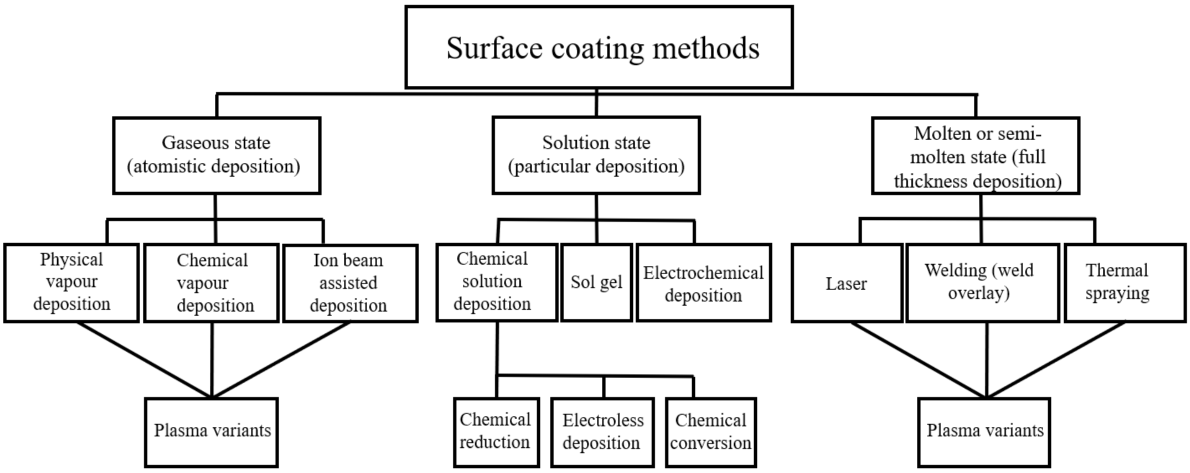

Figure 3.1: Different engineering techniques for the deposition of thin films (reproduced from [2])

The microstructure and mechanical properties are strongly related to the production technique. So when choosing a processing route, it is important to look at the chemical reactivity of the compounds, at the desired properties, and at the compatibility of the chosen technique with the whole system. (Example: if metals and ceramics need to be deposited to make a layered composite, then the technique must allow to deposit both.)

3.2.2 Metallic materials

3.2.2.1 Mechanical properties of metals

Metallic materials have a crystalline structure. The origin of their strength and ductility is totally understood and is described by the creation and motion of dislocations. These are linear defects which correspond to a discontinuity in the crystal structure allowing a change in the arrangement of atoms. It is the number and the arrangement of dislocations that allows plastic flow in metals and thereby controls the properties of metallic materials.

Several deformation mechanisms can take place in crystalline materials. These are: [39]

1. Glide of interface dislocations (Figure 3.2): the movement of a dislocation is brought about by an applied shear stress on the slip plane. It is the "normal way" that dislocations move when a material is plastically deformed. It is the movement of dislocations that allows the atoms to slide over each other. The crystalline order is restored on either side of a glide dislocation but the atoms on one side have moved by one lattice position.

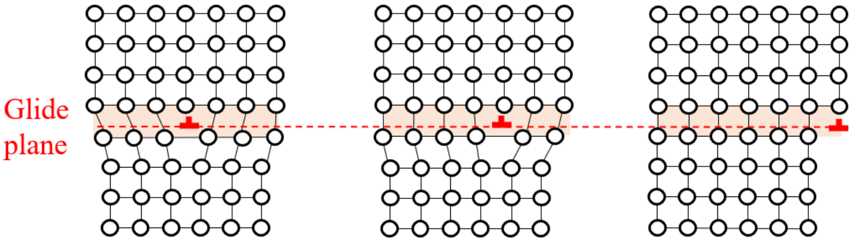

Figure 3.2: Glide dislocation (modified from [40])

2. Climb of interface dislocations (Figure 3.3): dislocations can climb along the interface plane because of the low formation energy and low migration energy of point defects in interface. It is a movement that is perpendicular to the slip plane and happens when a dislocation absorbs or emits a vacancy.

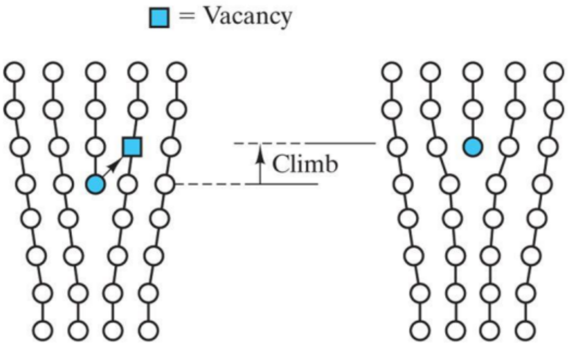

Figure 3.3: Climb dislocation [41]

3. Twinning (Figure 3.4): there exist also partial dislocations. They do not result from slipping between equivalent positions in the unit cell. The crystalline order is not fully restored with a partial dislocation.

   There exist a certain energy above which these partial dislocations can be observed. In fact, the energy of formation of a single dislocation must be more important that the energy needed to create two half (partial) dislocations. [42]

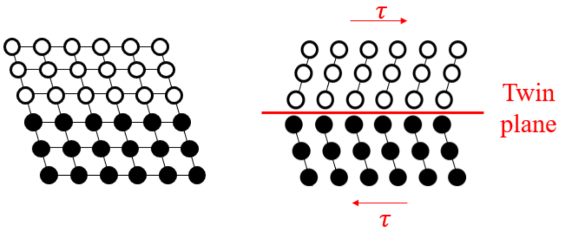

Figure 3.4: Twinning

The critical shear stress needed to nucleate a perfect dislocation is given by:

$$\tau_N = \frac{2\alpha\mu b_N}{D} \tag{3.1}$$

where D is the grain size, b_N the magnitude of the burger vector for a normal dislocation, μ the shear modulus and α reflects the type of dislocation (α=0.5 for edge and α=1.5 for screw dislocation).

Also, the energy required for a partial (twinning) dislocation is given by:

$$\tau_P = \frac{2\alpha\mu b_P}{D} + \frac{\gamma}{b_P} \tag{3.2}$$

where γ is the stacking fault energy and b_P the burger vector of a partial dislocation.

When the grain become smaller than a certain value D_c, then τ_P becomes smaller than τ_N. Therefore there will be some partial dislocation mechanisms when the grain size is below:

$$D_c = \frac{2\alpha\mu(b_N - b_P)b_P}{\gamma} \tag{3.3}$$

Due to the movement of dislocations, metallic materials have a middle strength value, and good ductility properties. In order to develop ultrahigh strength crystalline materials, the motion of dislocations that are required for plastic deformation must be limited.

3.2.2.2 Nanoscaling

In order to develop ultra high strain, people have thought about decreasing the scale of the materials by developing thin films, nanocrystalline materials and nanolaminates. The influence on the properties has been studied through the Hall-Petch effect.

Hall-Petch effect [28, 43]

The Hall-Petch effect, also known as grain boundary stenghtening, explains how metallic materials acquire higher strength by changing their grain size.

When a stress is applied to a material, dislocations move through a crystal lattice until they face a grain boundary. Grain boundaries can be seen as walls that can not be crossed by dislocations, stopping their propagation. In fact, the lattice structure from the neighboring grain differs in orientation and the grain boundaries are disordered compared to the grains so dislocations encounter a repulsive stress field, that is opposed to their motion. Therefore, the dislocations cannot go across this grain boundary.

However, when more and more dislocation arise, a phenomenon called ”dislocation pile-up” can be seen (Figure 3.5) which is a cluster formed of all the dislocations unable to cross the boundaries. Each of the dislocation generates a small field which is opposite to the repulsive fields of the grain boundaries. The sum of all of these small fields coming from all the gathered dislocations acts as a driving force against the energy barrier for diffusion across the boundary. An additional pile-up could then cause dislocation to cross the grain-boundary. Therefore, the size of the grain has an influence. In fact, by changing the size of the grains, the number of the dislocations piled up at the grain boundary can be decreased (Figure 3.6), limiting the diffusion. Stopping the movement of the dislocation will not allow the onset of plasticity thus the material will have an increased strength.

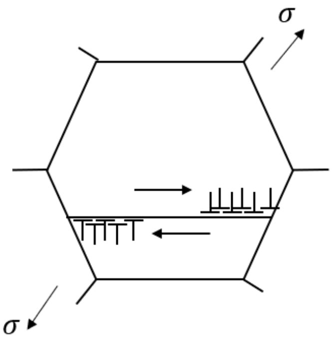

Figure 3.5: Pile up mechanism (reproduced from [44])

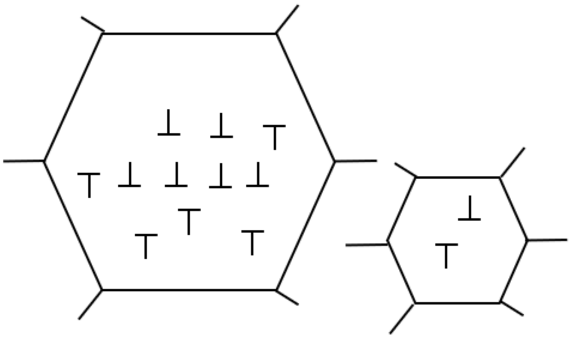

Figure 3.6: Different concentration in dislocations (reproduced from [43])

The relation between the yield strength and the grain size can be written: [45, 46]

$$\sigma = \sigma_0 + k_y d^{-1/2} \tag{3.4}$$

where d is the size of the grain, k_y is the strengthening coefficient (specific to a material) and σ_0 is the minimal stress that must be applied to activate dislocation motion.

Inverse Hall-Petch effect Following Equation 3.4, a material could be infinitely strong by decreasing the grain size to very small values. In practice, it is not happening. It has been shown that under a certain size limit, the grain will undergo other mechanisms and the increase of strength will be much lower that the one predicted by Hall-Petch. An inverse Hall-Petch effect is observed after a certain critical grain size: the abnormal grain size d*. [36] There are many models that describe this effect. [47–49] For example, the two-phase based model [50] states that the crystalline materials act as composite with two phases: the bulk and the grain-boundaries phases. The transition to an inverse Hall-Petch effect then comes a change from grain bulk to grain boundaries deformation mechanisms.

Influence of the grain size on the properties The mechanical properties are affected by the size of the grains. Several regimes can be established for the plastic deformation in metals as a function of the grain size. [51, 52] They are all illustrated in Figure 3.7.

1. For grain sizes down to about 100 nm, dislocations control plasticity as in bulk metallic materials. An increase of the strength with the grain size is observed, which is described by Hall-Petch relationship, as can be seen in zone I.

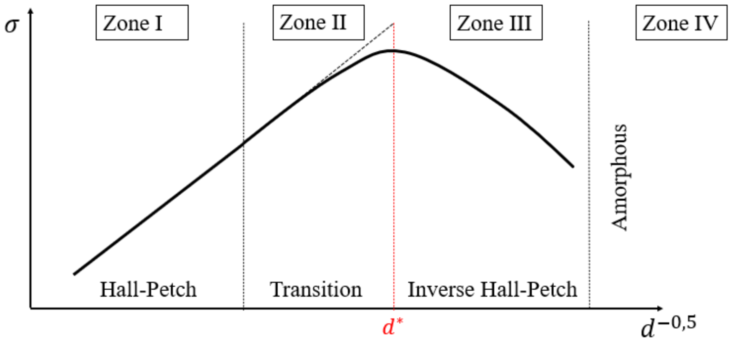

Figure 3.7: Evolution of the strength in metallic materials when lowering the grain size from bulk down to a few nanometers

2. At a nanometer length scale (between 10 and 100 nm), the dislocation activity becomes difficult due to the increased annihilation of dislocations at the grain boundaries (as can be seen in Figure 3.8). This transition starts when the traditional intra-granular dislocation mechanisms become limited and that grain boundaries start playing a more prominent role. The behavior of the strength is still increasing, with mixed mechanisms, up to a certain value d*. An estimate of this size can be made by assuming that it is the smallest grain size that can sustain a dislocation pile-up. After that, inter-granular sliding becomes important. [53]

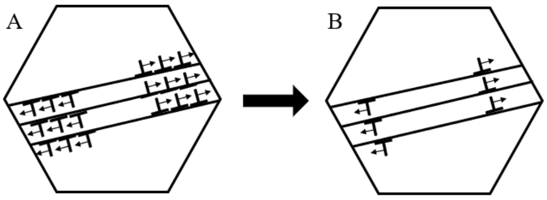

Figure 3.8: Transition from a dislocation pile up mechanism at the grain boundary to an absorption of the dislocation at the grain boundary (reproduced from [54])

3. By decreasing the grain size further (zone III), a decrease of the strength is observed, know as the inverse Hall-Petch effect. In this size range, the grains cannot generate and contain dislocations. They can then be considered as rigid bodies. The deformation occurs by grain boundary mediated mechanisms, such as intergrain sliding (Figure 3.9).

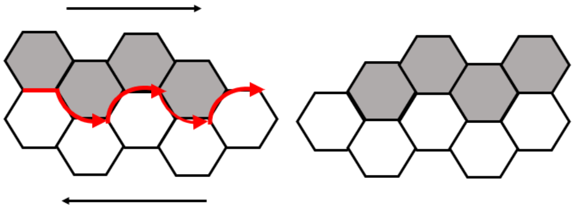

Figure 3.9: Grain boundary sliding (reproduced from [54])

4. Their is a physical limit to the grain size which is a unit cell of a material after which the grain are no longer crystalline but amorphous (zone IV).

3.2.2.3 Properties of nanoscale metals

Strength Due to a high density of grain boundaries and interfaces between layers the dislocation glide is not allowed. Therefore, ultra-high strength can be achieved in nanoscale metals, up to a certain size limit (the abnormal size). [39]

Hardness It can be shown [55] that the hardness also follows a Hall-Petch model giving:

$$H = H_0 + k_H d^{-1/2} \tag{3.5}$$

Also, as for the strength, it follows an inverse Hall-Petch relationship below a certain grain size. [56]

Ductility Nanocrystalline metals show limited ductility far behind the one of the ductile metals at conventional grain size. [57] This limited ductility comes from both an early localisation of the plastic deformation (known as necking) and an early failure.

First, thin metallic film have low strain hardening (n) and low strain hardening rate (m) because of an increased difficulty for dislocation storage at small sizes. Some localisation of the plastic deformation occurs in the material when the strain in the material is above a certain value called the onset of necking [28]:

$$\epsilon = \frac{n}{1-m} \tag{3.6}$$

Therefore, having a small n and a small m leads to non-uniform elongation and more plastic instabilities such as inhomogenous and localized deformations. Also, some failure before this plastic localisation can happen due to a rapid accumulation of damage. In fact, some fracture mechanisms (such as the nucleation, growth and coalescence of voids) can happen between the grains along grain boundaries. [30, 58]

However, the property of ductility can be optimized by several methods:

1. In nanolaminates made of several layers of metal, the interfaces can act not only as obstacles but also as a source for dislocation multiplication which improves ductility. This is developed in subsection 3.2.4. [48, 52]

2. Opting for an appropriate grain size distribution and the introduction of a second phase particle can also increase the ductility. [52] This can be done by using a bi-modal grain distribution in which the finer grains provide strength and the coarser grain sustain the dislocation activities and maintain or even enhance ductility, as can be see in Figure 3.10.

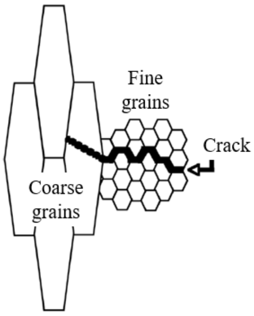

Figure 3.10: Bimodal distribution [48]

3.2.3 Metallic glasses

This parts aims at describing the behavior of amorphous materials, on the bulk form, and when reduced to the nanoscale. Metallic glasses are presented here because their study at the nanolaminate level in the literature is very rich. The same phenomena will take place in amorphous ceramics.

3.2.3.1 Bulk metallic glasses

Metallic glasses are solid metallic materials with an amorphous structure due to a fast cooling rate. The atoms occupy a more-or-less random position in the structure, giving them a non-crystalline structure. For long it has been a topic of interest to understand their behavior related to strength, ductility and plasticity at the micro-and-atomic scale. If it is not as clear as for crystalline materials, it has been shown that the mechanical properties of metallic glasses are related to the chemical and physical properties of their elements. [59]

The properties of bulk metallic glasses are a ultra-high strength and hardness and large elastic strain at temperatures much lower than T_g. In fact, they do not have crystalline defects such as dislocation that govern the plasticity in metallic materials, so the materials can be much stronger. However, they suffer from a high lack of ductility.

The plastic deformation of metallic glasses does not follow the scheme of dislocation motion as in metals. It is a nonhomogenous deformation due to the formation and propagation of shear bands. These are zone embedded in undeformed matrix, in which large shear plastic deformation has taken place. There are two theories concerning the creation of shear bands. These are the free volume theory and the STZ theory, as illustrated in Figure 3.11 [59, 60]

1. The free volume theory is based on the idea that the total volume of amorphous metal can be divided into two parts: the one occupied by the atom, and the empty space. The free volume regions are good spot to initialize structure destabilization, and where inelastic relaxation can take place. This model gives a simple and clear explanation for the strain-softening but not for the deformation itself.

2. Shear transformation takes place by spontaneous and cooperative reorganization of a small cluster of randomly close-packed atoms (between a few and perhaps 100 atoms). These clusters of atoms undergo cooperative shear displacements (called the shear transformation zones (STZs)) and enable material deformation. [61]

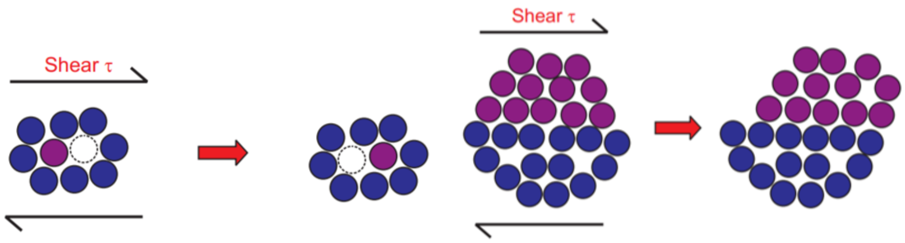

(a) Free volume theory (b) STZ theory

Figure 3.11: Two models to explain shear banding [60]

The formation and propagation of such shear bands induces strain localization and leads to large strain softening and abrupt fracture of the metallic glasses (as represented in Figure 3.12). This causes the lack of ductility of metallic glasses. [62–64]

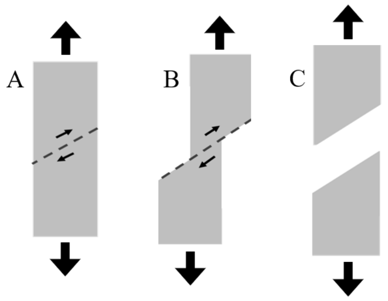

Figure 3.12: Shear bands leading to catastrophic failures with (A) shear localization, (B) propagation of shear bands and (C) abrupt fracture.

In principle, strain localization can be mitigated by generating profuse shear bands, obstructing shear bands propagation or inhibiting shear bands formation by reducing the size. This can be done through several channels, and one of them is reducing the sample dimensions to the nanoscale.

3.2.3.2 Nanoscale metallic glasses

It has been demonstrated that a radically different behavior is observed in monolithic metallic glasses when decreasing the sample dimensions up to 100 nanometers. In fact, due to the small volume, some interesting phenomena are observed such as a delayed catastrophic localization and an increased failure resistance. This can be seen from different angles: [65]

1. The size of the stressed metallic glass region must exceed an incubation length scale in order for STZs to develop into mature shear bands. As they need a sufficiently long distance to accelerate to their full propagation speed, they do not become as dangerous as in big samples. [62]

2. The sample dimensions are bellow the normal shear banding spacing. The major instabilities do not have enough space to grow, and the small sample volumes have less chances to contain flaw or predammaged sized defaults which can initiate severe localization shear bands.

3. If localization begins, then failure does not follow directly. In fact, these amorphous materials at the nanoscale have a tendency to break in a ductile way because the size of the plastic area at the tip of the developing crack is much larger than the size of the layer.

Without these severe shear bands concentrating all the strain on one plane, other phenomena can happen which are called ”dislocation-like” shear events. These are individual STZ throughout the sample, and local redistribution of free volume. So at small-volume specimens, the catastrophic localization and failure are deleted, leading to ductile metallic glasses. When brought into the submicrometer to nanometer range, metallic glasses behave such as metallic materials: uniform elongation, stable shear, necking, ... All of this leading to homogeneous deformation in metallic glasses under a certain size, as can be seen in Figure 3.13. [65]

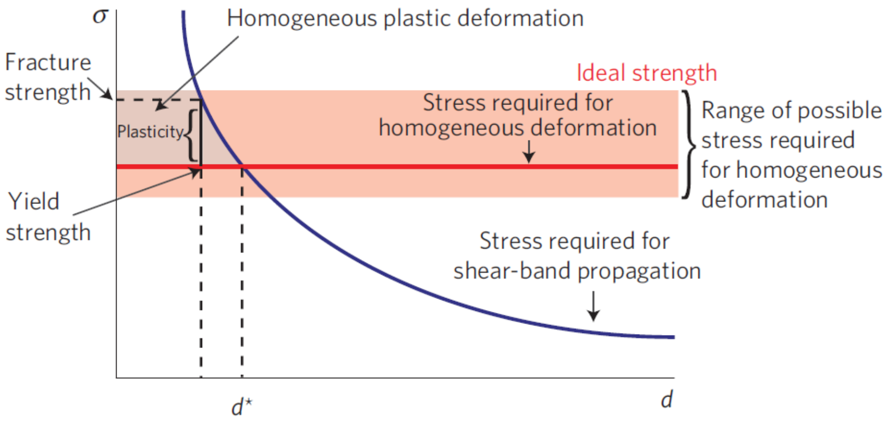

Figure 3.13: Transition from an homogeneous to a non-homogeneous plastic deformation. Bellow a certain layer size, d, the stress required for shear band propagation becomes higher than the one for homogeneous deformation, leading to some plasticity in the material. [63]*

3.2.3.3 Properties of nanoscale metallic glasses

Ductility As explained above, due to the small volume of the amorphous glass, the formation and propagation of shear bands is avoided, leading to an enhanced ductility through dislocation-like mechanisms.

Strength Unlike for metallic materials, the stress required for homogeneous deformation varies with the size (as can be seen in Figure 3.13 where the orange zone shows the range of possible homogeneous deformation). This is because the amorphous structures contain some internal fluctuations, and the biggest clusters of internals defaults are dependent of the size. The smaller the sample, the less chances to have internal defaults. So as in metals, an infinite strength could be obtain by decreasing the sample size, because no defaults would be present in the sample. However, there is a critical size at which the maximum strength is obtained, which can be compared to the inverse Hall-Petch relationship (even if the phenomena underlaying are totally different). In fact, the surface itself is an imperfection, and by decreasing the sample size, the surface-to-volume ratio increases, leading to a lower strength.

The stress required for homogeneous deformation related to the strength can be divided in three sections (see Figure 3.14): [66]

- In zone A, the surface-to-volume ratio is really high because of a large area of interfaces. The surface diffusion controls the strength.
- In zone B, some critical sized flaws begin to be observed, but with a low density. The strength is controlled by the shear band nucleation. It is in this zone that the maximal strength is found: when the interfacial area has decreased enough, but no critical sized flaws are yet in the sample.
- In zone C, critical sized flaws are inevitably present so the strength is controlled by shear band propagation.

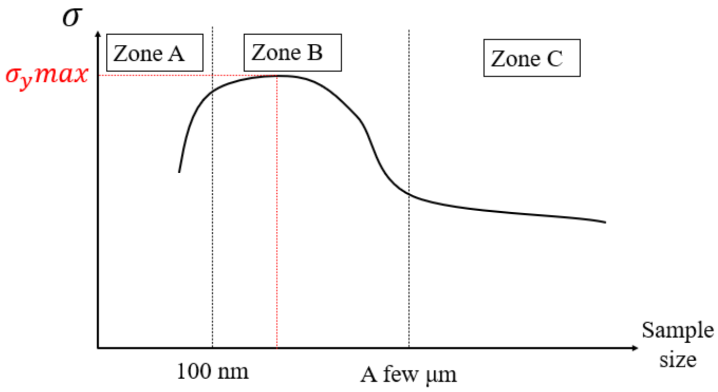

Figure 3.14: Strength of metallic glasses with regards to the size of the sample (reproduced from [66])

3.2.4 Nanolaminates

As it has been seen in the former subsections, lowering the scale of materials down to the nanoscale gives them interesting properties. However, it has some drawbacks. For example, the ductility of metals is decreased due to a lack of motion of the dislocations. These defaults can be corrected by composing laminates of these materials.

The mechanical behavior of nanolaminates is controlled by the interfaces. Their high density yields some special properties to nanolaminates. The interfaces have two main roles: [39]

1. They act as a source for nucleating plastic deformation carriers: dislocations, twins and shear bands, leading to high ductility.
2. They are a barrier which suppress the propagation of these carriers, leading to high strength properties.

Several systems of laminates have been proposed in literature, some of them are summarized in Table 3.1.

Table 3.1: Attributes of some multilayered materials at nanoscale. (Inspired by [67])

Nanolayered materials	Attributes	Exemple
Metal/metal	Magnetic properties	Cu/Nb [68], Fe/Co/N [69]
Ceramic/ceramic	Toughness, thermomechanical resistance	TiN/AlN [70], TiN/NbN [71]

3.3 Hybrids nanolaminates

In the previous sections, the nanoscale behavior of metallic glasses and metals have been described. While reducing them to the nanoscale provide them some advantages, they still aren't perfect for the required application. To enhance their properties, a combination of amorphous and crystalline material has been suggested.

In fact, by alternating layers of amorphous and crystalline structures in the form of nanolayered composites an improvement of the ductility has been observed, while keeping the strength of the amorphous layer. These composites usually results in a compromise between the higher strength of the metallic glasses and the higher ductility of the crystalline layers. [33, 72, 73]

3.3.1 Properties of hybrid nanolaminates

3.3.1.1 Ductility

Bulk metallic glasses exhibit terrible ductility properties due to the spread of catastrophic shear bands but this problem is avoided when the thickness of the metallic glass is below an intrinsic length parameter. On the contrary, metals have a good ductility, but reducing them to the nanoscale reduces their ductility. Layering the two materials produces some interesting ductility properties. Confining the metallic glasses between metallic layers leads to large tensile ductility, and to some extent to near perfect plastic behavior. It can be shown [62] that the amorphous crystalline interfaces (ACI) are the main reasons for the ductility enhancement in the two phases.

1. By looking first at the amorphous phase it appears that some of the large defects that normally evolve in the phases are stopped by the nanocrystalline layers before they reach maturity (for example, the thick metallic glass layers are thinner than a typical shear band in bulk glass (as can be seen in Figure 3.15)).

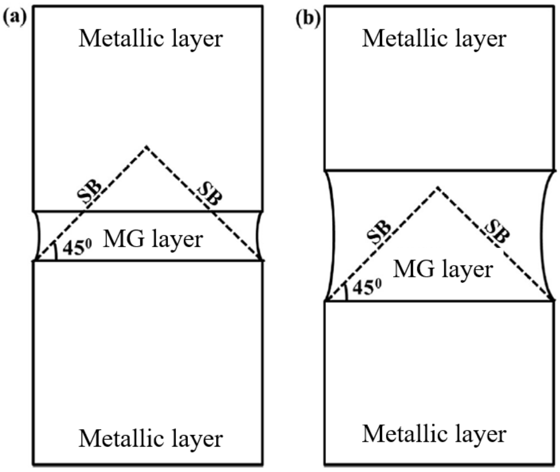

Figure 3.15: Effect of the ACI on the behavior of the metallic glasses with (a) a good example of the quarantine principle where the shear bands (SB) do not have enough place to grow and (b) an example where the quarantine principle is not efficient and SB have enough space to grow leading to bad ductility properties (adapted form [74])

2. Meanwhile, in the crystalline phase, the deformation is done through a few deformation twinning which are stopped by the grain boundaries and by the amorphous crystalline interfaces (ACI). The ACI also act as sources for dislocation nucleation, which are necessary

for the plastic behavior of the layers. Because of the comparable density of ACI and grain boundaries, ACI can be considered as having a great role in enhancing the ductility of the sample. [62]

It is the combination of these two effects (known as the quarantine principle, because it is the fact of separating the layers of a certain material by another one) which gives this ductile property to hybrids nanolaminates.

3.3.1.2 Strength

Nanolaminates exhibit a high strength. This is due to both the nanolayers which allow to have ultra high strength properties, and to the lamination. Following the quarantine principle, the ACI can act as a source for the dislocations enhancing the ductility, but they are also a barrier for dislocation motion, enhancing the strength of the crystalline layers. Hybrid nanolaminates exhibit a strength of the order of the strength of the hard layer while introducing benefits from the metal layer. [75]

3.3.1.3 Hardness

According to the rule of mixture, the hardness of a composite should be:

$$H = f_1 H_1 + f_2 H_2 \tag{3.7}$$

where f is the volume ratio of one constituent. However, this results does not fit to the experiments, so the hardness must be modified by an adapted rule of mixture. This has been done through several models. [76] The global trends that nanolaminates are following are:

1. There is an effect of the amorphous layer: the hardness is decreased when reducing the amorphous layer thickness. This is due to the fact that localized plastic deformations are suppressed as amorphous layers thicknesses reduce up to the scale of tens of nanometers. The deformation modes of the amorphous layer transform from localized shear banding to homogeneous flow.

2. There is also an effect of the spacing between these amorphous layers (which is equal to the thickness of the metallic layers). The hardness of nanolaminates for the crystalline/amorphous laminates shows a Hall-Petch dependence on the metal layer thickness: [45]

   $$H = A + B\lambda^{-0.5} \tag{3.8}$$

   where λ is the spacing between the amorphous layers, and A and B constant that have to be derived experimentally.

3.3.1.4 Elastic response

The Young modulus depends on the direction from where is it measured. As explained in section 2.3, the composite will follow an isostrain or isostress model depending on the loading conditions. However, by indentation, it has been shown that the Young modulus of hybrids nanolayers is lower than the one obtained by a simple rule of mixture of the materials. This is due to nanodefects or texture that lowers down its value. [67, 76–78]

Also, going deeper in the material will give a more accurate value of the Young modulus because the effect of the multilayers is more felt at high penetration. [35]

3.3.1.5 Toughness

High fracture toughness often requires a good strength/ductility balance.

The composite arrangement significantly increases the crack growth resistance of the glass. Growth of voids in the monolithic glass is catastrophic, whereas in the composite, it is stable. It has been shown that the crack growth resistance of metallic glass in metal laminate composites is higher that the one of the monolithic form. The toughness can be increased by both extrinsic and intrinsic parameters (these two different phenomena are illustrated in Figure 3.16). [79]

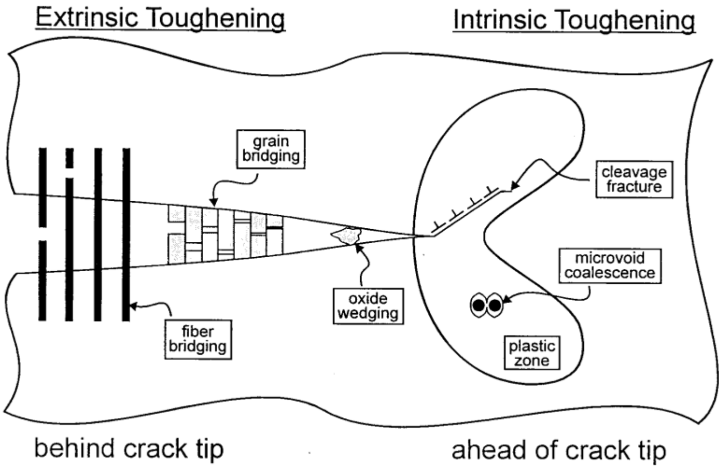

Figure 3.16: Extrinsic and intrinsic toughening [80]

The toughening of hybrids laminates has two main origins: [32, 81]

1. The confinement of the amorphous brittle layers into metallic layers gives some extrinsic toughening. The metallic ductile phase, after an initial crack propagation in the amorphous layers, tends to remain intact and bridges the opening crack increasing the crack-propagation resistance of the material.

2. The enhanced ductility properties of the amorphous phase gives some intrinsic toughening. In fact, enhanced glass deformation in the crack tip region is allowed.

3.3.1.6 Wear

The wear resistance of nanolaminates combining hard and tough phases exceeds the one of both their phases. [82] In fact, abrasive wear, fatigue strength and crack resistance are correlated to the relation between toughness and strength (hardness) of the material. Since hybrids nanolaminates have an enhanced toughness and strength, the result in term of wear resistance should also be improved. Several theories for the wear equation in multilayer materials have been developed [83, 84].

The enhanced wear resistance is attributed to the interfacial zone. The low hardness of the metal lamella allows the abrasive to penetrate easily to produce deep scratches. Meanwhile, the high ductility keeps the amount of material removed small compared to the size of the scratch. Close to the amorphous lamella, the penetration is limited due to the high hardness which supports the zone over the amorphous lamella. Therefore there is a small penetration depth and a high ductility: high wear resistance. This is illustrated in Figure 3.17.

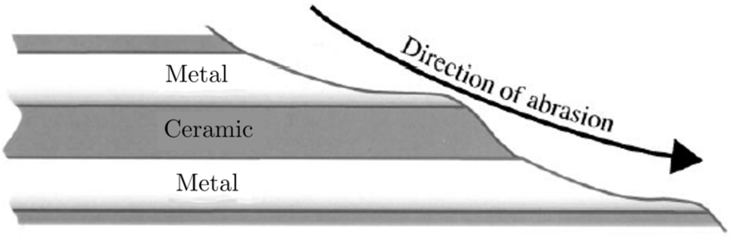

Figure 3.17: Wavy surface profile which illustrates the interfacial zone. The penetration of the abrasives in the metal layers is reduced close to the interface with the amorphous layers. (modified from [82])

The model on the interfacial zone suggests that in order to optimize the wear resistance of a material, two fundamental design rules should be followed:

1. The ductile layer should be thin, so that the entire layer is within the interfacial zone. (The ductile layer should have a thickness less than the one plastically deformed when scratching the unsupported layer.)
2. The hard supporting phase has to be kept thin since it has a lower wear resistance than the interfacial zone.

3.3.2 Al/Al_2O_3 nanolaminates

As explained in the former sections, reducing the size of materials to the nanoscale gives them specific properties. When using laminates of these small-scale materials, some new properties arise. And finally, when combining amorphous and crystalline layers at the nanoscale, some hybrid materials are created with enhanced mechanical and wear properties.

This study of crystalline/amorphous layered composite using several materials has been of a wide interest in literature. While the crystalline phase is always made of metal, the amorphous layers can have different nature: either made of metallic glasses or amorphous ceramics.

Several systems used metallic glasses as amorphous phase such as in [60, 62, 64, 65, 72] where Cu/CuZr is one of the most commonly studied system and has shown enhanced ductility (up to a nearly elastic-perfectly plastic behavior under certain conditions) and toughness properties.

Other systems used amorphous ceramics instead, such as systems like W/ZrN [85], diamond like carbon (DLC)/Ti [86], Al/SiC [34, 67], Ti/TiN[87] which have shown some interesting properties enhancement. The system Cr/CrN has achieved a regime of co-deformation of the layers and particularly good wear resistance. [82]

This master thesis focuses on the study of the nanolaminate Al/Al_2O_3 deposited by physical vapor deposition. The mechanical properties of Al/Al_2O_3 laminates at the micro scale have been studied in [32, 88]. Some mechanical characterization of its tensile properties under certain conditions has also been made [77, 89]. Its wear resistance under certain conditions has been studied in [90]. The various experiments carried out in these articles indicate that the Al/Al_2O_3 system has interesting mechanical and tribological properties. Therefore the study of its resistance to erosion is relevant.

Herunder in a small description of the crystalline and amorphous phases used in this laminate.

3.3.2.1 Crystalline phase: aluminum

The crystalline phase is made of aluminum. It is an FCC metal which is sensitive to the strain rate. It has the highest strength-to-weight ratio and is one of the more abundant material on earth which makes it a common used material. It is widely used in an alloyed form.

One of the main feature that has an influence on its properties is its grain size. It has been shown that the average grain size in the aluminum films varies linearly with the film thickness in films were it is one grain thick. The grain size in aluminum is controlled by the deposition technique. [77]

3.3.2.2 Amorphous phase: alumina

The amorphous layers are composed of alumina, in the form of an amorphous ceramic. Alumina is used in a wide range of applications because it has a good hardness, transparency and electrically-insulating properties. The most common oxide form is the amorphous form. However, crystalline alumina exists in different forms: $\alpha, \kappa, \theta, \nu$ and γ phase which are formed under specific deposition conditions. [91]

One of the main feature that has an influence on its mechanical properties is its porosity. This is controlled by the deposition technique. [92–96]

Chapter 4

Materials and methods

Now that the basics of coating characterization methods have been developed, as well as the advantages of using nanolaminates, it is time to dive into the heart of the research of this thesis. This thesis focuses on the realization of Al/Al_2O_3 samples and on the characterization of their scratch resistance and mechanical properties. This chapter describes the methods used to produce the samples and to characterize them.

4.1 Deposition method

4.1.1 Sputtering

Sputtering is one of the most common physical vapor deposition (PVD) process which are techniques to deposit thin film of a material into a surface under vacuum.

4.1.1.1 General principle

The principle of sputtering (as illustrated in Figure 4.1) is a phenomenon in which ions created in a gaseous plasma are accelerated and then hit the target material ejecting some atoms that are then redeposited.

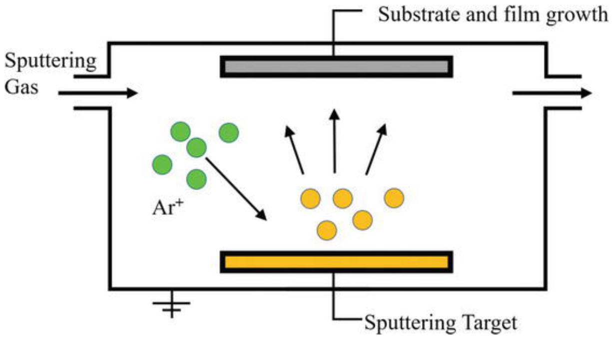

Figure 4.1: Illustration of the sputtering principle [97]

A target of the desired material is held in a high vacuum chamber. Argon is injected continuously in the chamber to obtain a low pressure argon atmosphere. Inert gases, specifically argon, are usually employed as sputtering gas because they tend not to react with the target material or combine with any process gases and because they produce higher sputtering and deposition rates due to their high molecular weight.

When the vacuum in the chamber is well established the plasma is ignite by applying a negative voltage (by a DC electrical current) to the target. It is composed of Ar atoms, positively charged ions Ar^+ and electrons. The positively charged Ar^+ are continuously generated by the electrons hitting the argon atoms.

In fact, the target is negatively charged and acts as a cathode while the chamber is connected to the ground and acts as an anode. This creates an electrical potential which will cause the free electrons to accelerate. When they collide with a process gas atom, they strip an electron from the gas atom and create a positively charged gas ion.

Since the sputtering target is negatively charged, the positively charged argon ions are then accelerated towards the target. When they collide with the target, they transfer their energy to some atoms of the desired material. If this energy is larger than the bonding energy, then atoms are liberated from the target. They are sputtered atoms. These sputtered atoms will then redeposit all around the chamber. If a substrate is placed in front (or in the path) of the sputtered atoms, it will be coated by a thin film surface.

A permanent magnet structure is located behind the target serving as a deposition source and allows plasma confinement on the target surface. In fact, this magnet results in a magnetic field that forms a close-loop annular path. This will reshape the trajectory of the secondary electrons, increasing their probability to hit an ionize argon atoms. This process of using a permanent magnet to help ionizing the argon is called magnetron sputtering. [98, 99]

4.1.1.2 Deposition of an oxide by sputtering

The general principle described above is the case of non-reactive sputtering. When the thermodynamics and kinetic of the chemical reaction have an influence on sputtering an alternative method has to be found.

In the case of oxide target materials, some preferential sputtering will occur. Oxygen will sputter faster than the metallic atoms, leading to an enriched in oxygen deposition on the substrate and a reduced target. The target is then enriched in metal, and the deposited oxide is non homogeneous and will become richer and richer in metal the more the reduction of the target takes place. To avoid this reduction, it is possible to use a metallic target and to add a reactive gaz (such as oxygen to create Al_2O_3). The process is then called reactive sputtering. [98]

This sputtering can be divided into two phases: the metal target mode region, and the compound mode (as illustrated in Figure 4.2). When there is no oxygen in the sputtering gas, only metal will be deposited. At a critical flow of reactive gas, the deposition mode changes abruptly from the metal mode to the oxide (compound) mode.

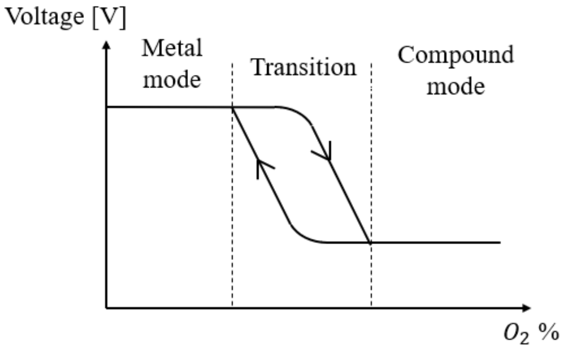

Figure 4.2: Hysteresis curve of the reactive sputtering

4.1.1.3 Parameters

Several parameters have an influence on the deposited samples:

- The sputtering yield depends on the target material and on the angle of incidence.
- The voltage can either be RF (for insulating targets) or DC (for conductive targets). RF is necessary for insulating targets because otherwise the Ar^+ ion would charge the target and it would then repel the Ar^+ so no sputtering would occur.
- The target-substrate distance and rotation also influence the quality of the deposition. If the distance is too short, some heating of the substrate could be observed. Also, if there is no rotation of the target, some compositional gradient could appear.

4.1.2 Deposition of the samples

Layers of Al and Al_2O_3 were deposited successively by RF (13.56 MHz) magnetron sputtering on silicon wafers (cleaned by standard cleaning [1]). The sputtering experimental method that was used in the context of this master thesis was AJA (ATC Orion 5 Sputter System from AJA International).

As stated in the state of the art, the properties of the aluminum and the alumina layers strongly depend on the deposition parameters:

- The main property in aluminum that has an influence on its properties is the size of its grains. This can be controlled by the magnetron power: as the power increases, the grain size will be reduced. [100]
- All deposition parameters (such as the deposition pressure, the gas pressure, ...) have an influence on the resulting properties of alumina. The ideal properties would be high-density, stress-free and hard aluminum oxide thin film with a high deposition rate and excellent adhesion on substrate. [91, 96, 101, 102]

4.1.2.1 Deposition conditions

The deposition parameters were chosen following [96] to minimize the porosity in the sample and are shown in Table 4.1.

Table 4.1: Details of sputtering conditions (inspired by [103])

	Al layers	Al_2O_3
Sputtering gas	Ar	Ar and 12% of O_2
Gas flow	25 SCCM	22/3 SCCM
Working pressure	1.2mTorr	1.2mTorr
Target	Al (99.99% purity)	Al (99.99% purity)
Deposition rate	5.88 nm/s	8 nm/s

A DC current was used, and was regulated at 300mA. A 400 V voltage was chosen, giving a power of 125 W. To achieve a uniform deposition, the holder was rotated at 45 rmp and was maintained at a distance of 122 mm of the target.

The selected partial pressure of oxygen was taken following the hysteresis curve of alumina.

Before deposition, the substrate were cleaned for 5 minutes with Ar plasma. Then, between the deposition of the different layers, the gas were mixed during 3 minutes to ensure an homogeneous gas flow.

---

[1] Details about this procedure can be found in section A.2.

4.1.2.2 Deposited samples

In nanolaminates, three main ”layering” features have an influence on the properties:

1. The proportion of aluminum/alumina
2. The bi-layer thickness
3. The top and bottom layers

In this thesis, only the two first parameters were studied. Table 4.2 shows the expected layer thicknesses and proportion of the different materials in the samples which were deposited to carry out the analysis. They all have a top layer made of alumina an a bottom layer made of aluminum. The real layer thicknesses were determined by SEM and are presented in the results.

Table 4.2: Expected layer thicknesses and proportion of the deposited sample

Sample	Total % Al_2O_3	Number of layers	Al_2O_3 layer thickness (nm)	Al layer thickness (nm)	Total thickness (nm)
E7014	16.6	16 (2*8)	14	70	672
E7035	33.3	14 (2*7)	35	70	735
E7070	50	10 (2*5)	70	70	700
E3535	50	20 (2*10)	35	35	700
Pure Al_2O_3	100	1	700	-	700

With these samples, three ”batches” of analysis have been carried out:

1. The first batch studies the influence of alumina proportion by using E7014, E7035 and E7070.
2. The second batch studies the influence of aluminum proportion by using E7035 and E3535.
3. The third batch studies the influence of the bi-layer thickness by comparing E7070 and E3535.

Note that other samples were deposited during this master thesis but were not used in the analysis. First because the scratch tests performed on the samples were not deep enough, so they could not be used in the analysis. Also, because some of them varied 2 parameters at the same time. The complete list can be found in section A.3.

4.2 Characterization

4.2.1 Scratch

To assess the adhesion properties of the coating, a scratch test was used. This was performed using a scratch tester fitted with a diamond stylus. The tip was a spherico-conical tip, with an angle 90 °, and a tip radius of 5 μm. The same loading parameters were used for the different tests, in order to have comparable data.

First of all, a pre-scan of the surface was carried out in order to know the initial morphology of the surface. This makes it possible, among other things, to know the inclination of the surface, and to recalculate the effective values of the tip penetration afterwards. The scratches were then carried out over a length of 750 microns, with a force increasing linearly from 0 to 45 mN. The velocity was of 30 μms^{-1}. The parameters used for the scratch test were first chosen following [89]. Then, in view of experiments carried out with a load such as in this article which did not go far enough into the material and therefore did not give the values of L$_c$, the load was increased. After the scratch, a post-scan was performed to measure the residual penetration, so that the elastic recovery of the material could be calculated.

The movements of the tip are summarized in Figure 4.3.

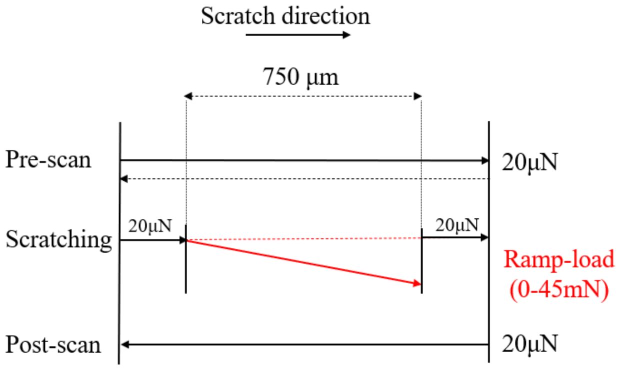

Figure 4.3: Different displacements of the tip. The pre-scan starts at the left end and goes to the right end. It then returns to its initial position (shown here by dotted lines). Then the scratch is performs with an increasing load (in red on the graph). The small scans before and after the scratch are to stabilize the tip before the scratch test, and to measure the size of the pile up or the behavior just after the scratch test. The post-scan is done directly from the right edge to the left edge. (Inspired by [104])

The friction force and the penetration depth were measured continuously along the scratch track. A measure of the cross-profile was made at 20mN. For each set of parameters, 8 parallel scratches were made, with enough space between them to avoid pile-up effects.

4.2.2 SEM

The scanning electron microscopy (SEM) is a method that allows to visualize the surface of a sample. It produces images of a sample by scanning the surface with a focused electron beam. It was used in this research because it allows to see details up to the nanometer scale. It can provide information about the surface topography (whether there are some cracks on the surface), and about the surface composition.

Its principle is to use the behavior of electrons to create topographic images. As illustrated in Figure 4.4, it has three parts: first the electron source where the electrons are created thanks to an electron gun. Then some electromagnetic lenses which focus the electron beam on the sample. And finally some electron detectors.

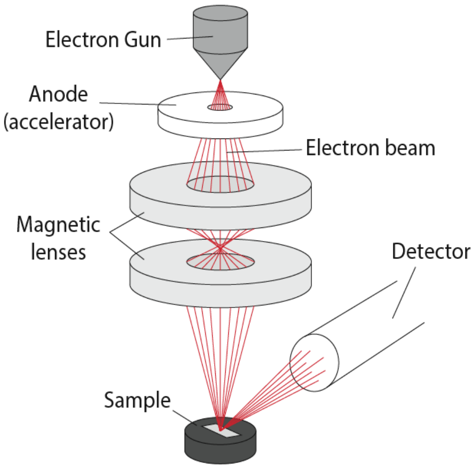

Figure 4.4: SEM [105]

For the images two types of detectors were used: the secondary electrons (SE2) detector and the InLens detector. They both collect secondary electrons which are generated from inelastic scattering events of the primary electrons with electrons present within the atoms of the sample. There are two types of these electrons (as illustrated on Figure 4.5): SE1, which are produced by the scattering of some electrons due to the incident beam on the surface and SE2 which are produced indirectly when the back-scattered electrons (created by the elastic scattering in the sample, and emerging out of the surface) inelastically scatter electrons, near the surface. The SE1 electrons, collected by the In-lens detector are used to image surface details at the highest resolution at the expense of compositional information. The images given by the SE2 electrons take advantage of a higher landing energy and deeper specimen interaction, including more compositional and less topographical information.

SEM samples have to be small enough to fit on the specimen stage. They may need special preparation to increase their electrical conductivity and to stabilize them, so that they can withstand the high vacuum conditions and the high energy beam of electrons.

The samples were mounted on rigidly specimen holder using a conductive adhesive. To make the samples with an alumina top layer usable for SEM, they were coated with a thin layer of gold.

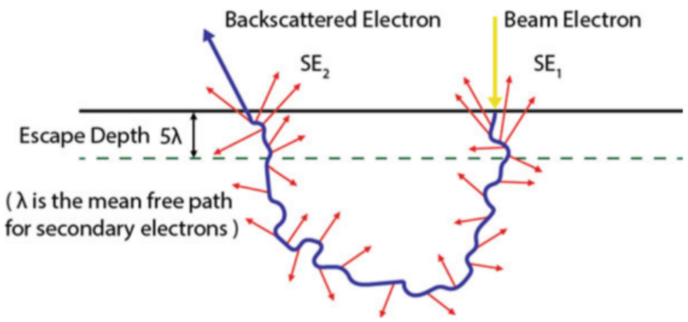

Figure 4.5: Illustration of the secondary electrons. The SE1 are generated close to the beam of electrons and have a high resolution signal. The SE2 are generated further away and have therefore a lower signal resolution. The secondary electrons are represented in red. Note that the SE are produced only near the surface of the sample (only 5 λ). [106]

4.3 Indentation

The mechanical properties of the materials such as hardness and the Young modulus were derived by numerical simulation using finite element methods. The program Abaqus (version 2019) was employed in all calculations.

4.3.1 Models

To simulate the different results, three different models were designed. The two first models were ran using the graphical interface of Abaqus, known as the Abaqus CAE (Complete Abaqus environment). The other model was designed at UCLouvain [107] and used matlab to generate an inp (the input file that is read by Abaqus) directly.

Three models were necessary, because they have different objectives:

1. The first model aims at comparing the stresses and strain produced by the scratch and the indentation test. Therefore the model was build using a 5 μm tip, which is the same diameter as the one used for the scratch test.

2. The second model uses a Berkovitch tip. It gives more accurate results when measuring the mechanical properties of the samples. Also, it is more sensitive to the strain rate in the samples.

3. Finally, the last model, developed at UCLouvain [107] was used to confirm the former models. Writing the inp directly is a technique which is more difficult and less intuitive than using the graphical interface directly. But once build, it is a more versatile tool, and will allow to compare many different systems in the future.

The different system studied are listed in Table 4.3. The geometry of the nanolayers in the simulation were the same as in the experimental samples. Note that the top layer was Al_2O_3 for all the systems, except for the pure aluminum.

Table 4.3: Different systems modeled in Abaqus

Sample	Total % Al_2O_3	Number of layers	Al_2O_3 layer thickness (nm)	Al layer thickness (nm)	Total thickness (nm)
Pure Al	-	1	-	700	700
S7014	16.6	16 (2*8)	14	70	672
S7035	33.3	14 (2*7)	35	70	735
S7070	50	10 (2*5)	70	70	700
S3535	50	20 (2*10)	35	35	700
Pure Al_2O_3	100	1	700	-	700

4.3.1.1 General considerations of the models

For all three models, 2D axial symmetry was used to reduce computational time without compromising accuracy. The movement of the indenter was simulated as a downwards displacement of 70nm. This corresponds to a deformation of around 10% of the coating height.

It was assumed that the coatings perfectly adhered to the silicon substrate and that the interfaces between the different layers were perfectly bonded. A friction coefficient between the top layer and the indenter was taken as being 0.1, which is a typical value for diamond/metal contact pair. [35, 108]

The layers were taken as homogeneous materials. In fact, the crystals in Al possess a high degree of isotropy, and the Al_2O_3 layers are amorphous. It is then a good approximation to use a continuum approach.

The input mechanical properties of the materials used is the simulation are given in Table 4.4. The alumina was taken as a perfectly-elastic material and the aluminum as an elastic perfectly-plastic material. The values chosen were taken following sources [96, 109–115] and measurement made on pure aluminum and pure alumina [116].

Table 4.4: Mechanical properties of the materials involved in the modeling

Parameters	E modulus (GPa)	Poisson's ratio	Yield strength (MPa)
Al	70	0.33	350
Al_2O_3	185	0.22	-
Substrate (Si)	187	0.28	-
Indenter (diamond)	1141	0.07	-

4.3.1.2 First model: spherical tip

As stated above, the first model used a spherical tip with a radius of 5 μm. The substrate was simulated using a rectangle of 25 μm width and 24.3 μm high, to obtain a perfect square with the layers on top.

Boundary conditions The following boundary conditions were used:

1. The left-hand side of the complete structure, including the indenter, coating and substrate served as the axial symmetry axis. They were only allowed to move in the vertical direction.
2. The bottom was encastred (unable to move in any direction).
3. Due to the fact that the model dimension was considerably larger than the coating thickness, the resultant edge effect from the boundary constrain was negligible, so the right-side was free to move.
4. The top boundary, when not in contact with the indenter was also free to move.

All these conditions, and the model can be seen in Figure 4.6.

Meshing A total of 105.000 four-noded rectangle elements were used in the model, with a finer mesh size near the upper left corner, as illustrated in Figure 4.7.

Projected contact area To calculate the projected area, a Matlab model was used. This model takes as input the position of the top layer as a function of the penetration depth, and the position of the reference point of the indenter. It then redraws the shape of the indenter mathematically, and calculates the difference between the position of the tip and the surface. When the difference is below a certain value, the two point are considered in contact.

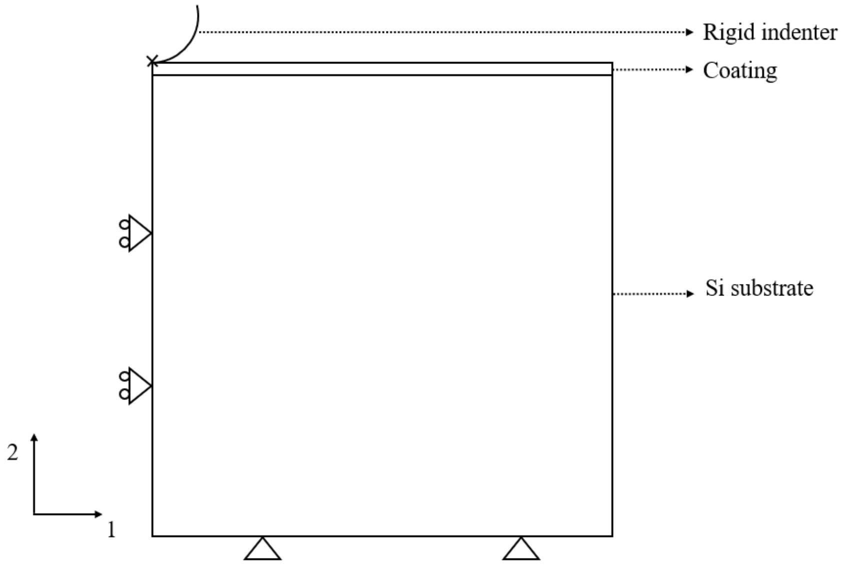

Figure 4.6: Boundary conditions of model 1

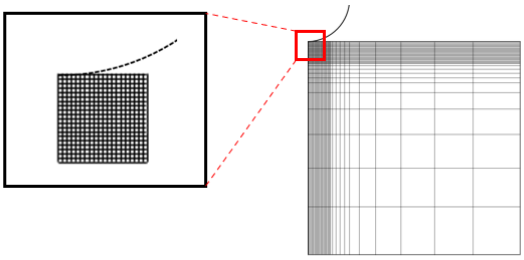

Figure 4.7: Illustration of the meshing in model 1

4.3.1.3 Second model: berkovitch tip

The second model implements a Berkovitch tip and was developed to measure the hardness and the Young modulus of the laminates. It also allows to see the influence of the deformation rate in aluminum.

It is the most commonly used tip for indentation testing. However, it is more complicated to simulate because it has a discontinuity at the end of the tip. To avoid this discontinuity, a small-rounded part has to be added. The construction of the tip is detailed in section A.1.

A smaller model was used is this simulation. With small penetration depth, the edges of the substrate were not influenced by the penetration, showing that this choice was relevant. The model is illustrated in Figure 4.8.

The same boundaries conditions as in model 1 were used. A total of around 12500 four-noded rectangle elements were used in the model, with a finer mesh size near the upper left corner.

4.3.1.4 Third model: realized via the inp generator

The last model was the one developped at UCLouvain [107] and used an inp (the input file that is read by Abaqus) generator created on Matlab directly to create the inp instead of using the graphical interface. This has the main advantage of being adaptable once done, but is harder to implement in the first place. This is why the graphical interface was used at first.

The same construction parameters as in the two models presented before was used.

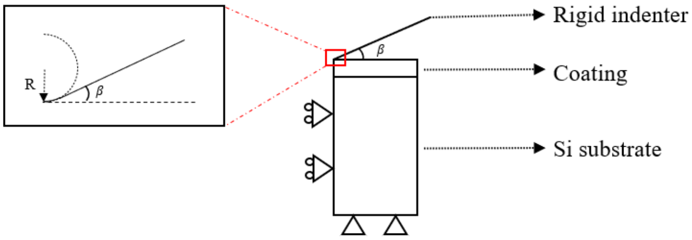

Figure 4.8: Abaqus berkovitch model with zoom on the tip showing its rounded part

4.3.2 Modeling the influence of the strain-rate sensitivity

When a material is strain-rate sensitive, its yield stress changes as a function of the deformation rate. Aluminum has a medium-sensitivity to strain-rate, but is not very sensitive at room temperature.

4.3.2.1 Exponential charging

In order to see the influence of the deformation rate on the properties of a material, deformation must be done at a constant deformation speed. This induces:

$$\dot{\epsilon} = \frac{\dot{h}}{h} = C \tag{4.1}$$

where $\dot{h}$ is the loading rate. By integrating this expression, it gives that the loading must have an exponential form:

$$h = h_i e^{Ct} \tag{4.2}$$

where h_i, is the initial indentation value.

In Abaqus, this was implemented using the function decay which is define by:

$$a = A_0 + Aexp(-\frac{t - t_0}{t_d}) \tag{4.3}$$

In order to use this decay function to simulate Equation 4.2, the different values of the constant are described as shown in Table 4.5.

Table 4.5: Values of the constant in the decay model

Name	Constant	Value
Initial amplitude	A_0	0
Maximal amplitude	A	h_i
Starting time	t_0	0
Decay time	t_d	$\frac{-1}{C}$

A range of deformation rate values from 10^{-5} to 10 [s^{-1}] was chosen, in order to see a real evolution on the material properties. Figure 4.9 shows a logarithmic plot of the exponential charging at these different loading rates.

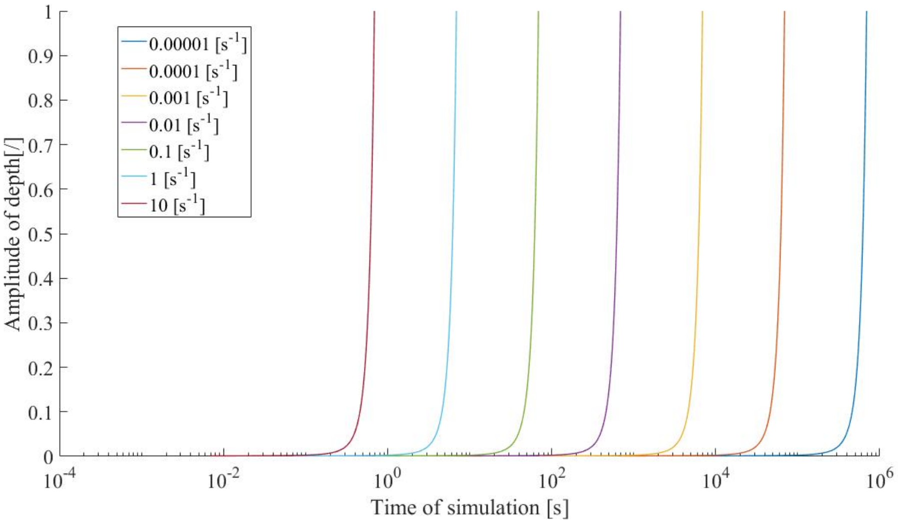

Figure 4.9: Time required to run the simulation for exponential charging with different deformation rate for an initial amplitude of 0.1%.

4.3.2.2 Plasticity models used in Abaqus

In section 2.4, several common plasticity models were presented. These are the ones closest to material reality, but they are not the easiest models to implement in Abaqus. There are indeed models that are already programmed in Abaqus and that allow to take into account the sensitivity to the deformation rate. These are the Jonhson-Cook and Cowper-Symonds models.

Jonhson-Cook This is a particular type of von Mises plasticity model with analytical forms of the hardening law and rate dependence. It takes into account the effect of the deformation rate, and also of the temperature. It is written:

$$\sigma_y = [A + B(\epsilon_{pl})^n][1 + Cln\frac{\dot{\epsilon}}{\dot{\epsilon_0}}](1 - T^{*m}) \tag{4.4}$$

where A,B,C,n,m,T* and $\dot{\epsilon_0}$ are constants that must be defined for the material properties.

Cowper-Symonds The power-law, also called the Cowper-Symonds overstress power law has the form: [117]

$$\dot{\epsilon} = D(R - 1)^p \tag{4.5}$$

Or this can be rewritten by:

$$\sigma_y = \sigma_0 \left((\frac{\dot{\epsilon}}{D})^{1/p} + 1 \right) \tag{4.6}$$

In Abaqus, the following parameters needs to be entered: D and p which can be measured experimentally.

User's chosen model If, however, a more common plasticity model wants to be chosen, there is a way to enter manually the evolution of the yield stress for different strain rate. It is then interpolated by Abaqus.

In the simulation, aluminum was chosen as being an elastic-perfectly plastic material sensitive to strain rate. The model chosen to simulate plasticity was the Cowper-Symonds model. The values of the constant comes from [118]. The strain rate sensitivity of the alumina was not taken into account. Figure 4.10 shows the evolution of the yield stress in aluminum for different strain rates.

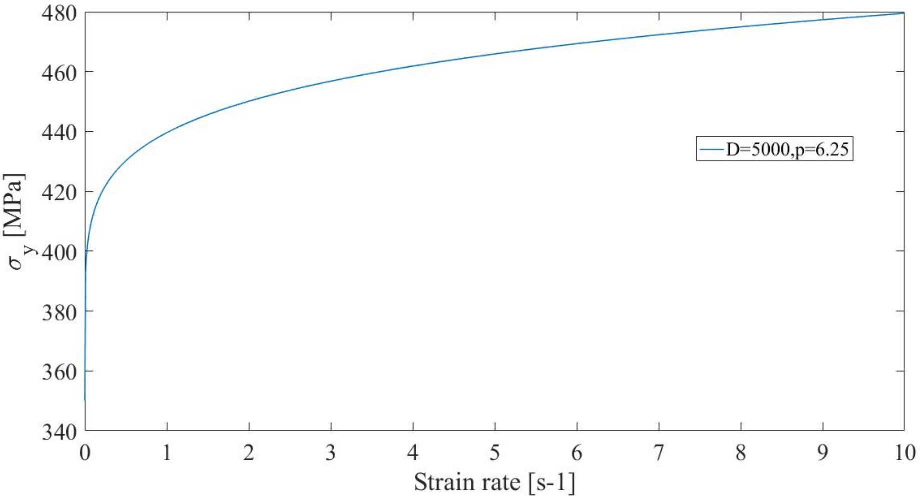

Figure 4.10: Evolution of the yield stress for different strain rates following Cowper-Symonds model for aluminum [118]

Chapter 5

Results and discussion

This chapter describes the different investigations made to characterize the experimental samples and the numerical simulations. It is divided into three parts: firstly, the microstructure and the scratch resistance of the deposited nanolaminates are studied. Then, their mechanical properties are derived by indentation simulation. Finally, some parameters such as the strain rate sensitivity are studied, also by indentation simulation.

5.1 Microstructure

This sections aims at describing the appearance of the material on the nanometer/micrometer scale. The main information required here are the arrangement of the different layers, the layer thicknesses and the structure of the different phases.

5.1.1 Cross section SEM

To obtain the modulation structure of the Al/Al_2O_3 nanolaminates, some SEM images of the cross-section were carried out. These are shown in Figure 5.1.

The cross-sections of the different samples show a ductile fracture. The samples were cut following the cleavage plans of the silicon substrate, which breaks on a brittle way so the cut should be clean. However, due to the ductility of aluminum in the nanolaminates, the coating will not break as fast as the silicon underneath and will undergo some plastic deformation before breaking, giving this ”dirty” aspect to the cut of the multilayer.

These pictures clearly show that the materials are laminates. The darkest zones show the alumina layers, while the brighter zones are made of aluminum. In fact, in SEM, the heavier a compound, the brighter it will appear on the screen. This is due to a larger scattering of the electrons for heavier compounds.

The layer thicknesses are not of the same height as the one predicted. This is due to a wrong estimation of the deposition time. This error is due to the fact that the aluminium target is damaged (probably hollowed out in the centre) which influences the deposition time.

5.1.2 Further investigations

To gather information over the overall composition, and over the structure of the different phases, some further investigations should be done. To have a better idea of the composition, and to see if some poisoning has occurred during the sputtering depositing, a low-angle X-ray diffraction device could be used. This is a special type of XRD for thin films.

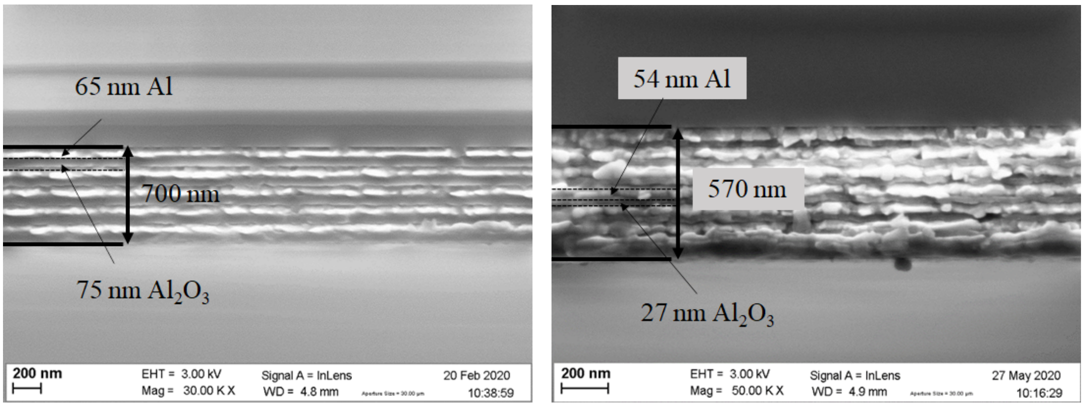

(a) E7070 (b) E7035

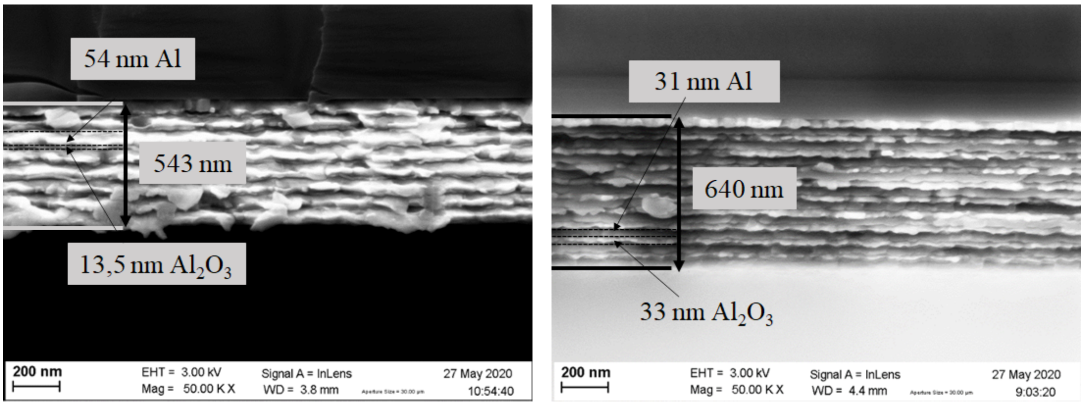

(c) E7014 (d) E3535

Figure 5.1: SEM images of the cross sections of the nanolaminates

Also, by taking TEM images of the surfaces and of the cross sections, some information such as the grain size and the crystalline structure of aluminum or the phases in alumina could be measured giving some interesting features to discuss.

5.2 Scratch analysis

This section presents the scratch profiles of the different samples. It studies their scratch resistance, and their failure mechanisms. Several parameters are observed: the penetration depth, the critical load, the deformation process and the different scratch mechanisms responsible for failure.

5.2.1 Reproducibility of the results and extraction of the average trends

5.2.1.1 Reproducibility of the scratch test

For each sample, 8 subsequent scratches were made. Figure 5.2 shows an example of the scratch tracks all together. This figure shows a good reproducibility of the scratches. However, the different peaks are not perfectly aligned (for example the ones at 700 μm), so using a mean value of these curves will have a tendency to hide the different phenomena happening during scratch, and tend to smooth the defaults. This is why one single curve analysis is preferred. Also, using the scratch distance or the normal force as the abscissa axis gives the same curve, because the load applied is proportional to the scratch distance.

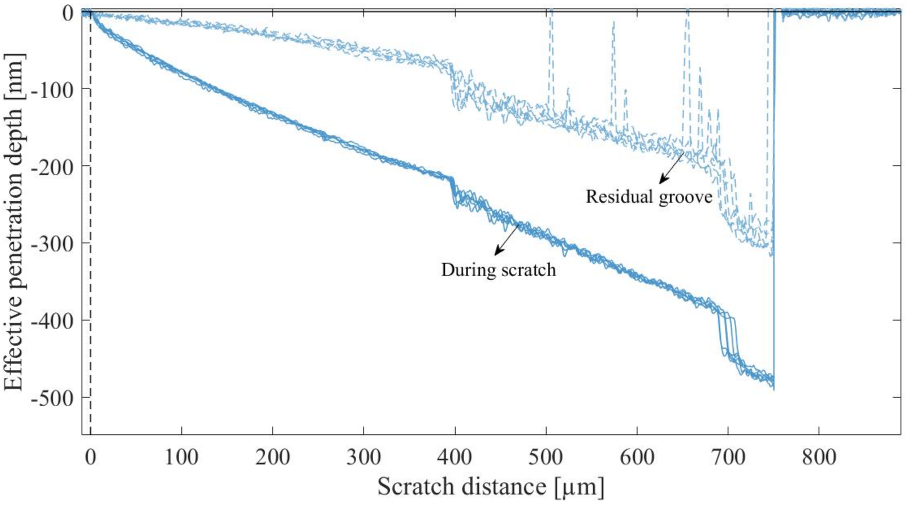

Figure 5.2: Penetration depth profile for all the different scratches made on sample E7070, demonstrating the reproducibility of the measurements

5.2.1.2 Trust in the samples and the datas

Due to the COVID-19 pandemy, the number of sample studied is limited. The datas here are not extensive. For two of the studied parameters only two different nanolaminates composites were compared. However, the resulting tendencies were studied and compared with the literature to see their relevance. It is evident that all experiments should be repeated to confirm the results and draw statistically relevant conclusions.

5.2.2 Analysis of the penetration depth behavior

The first, and basic analysis which can be made relies on the penetration depth. It is the easiest way to measure the scratch resistance of a material. The smallest penetration depth shows the highest scratch resistance of the coating.

5.2.2.1 Influence of the alumina content

The first parameter studied here is the influence of the proportion of alumina in a coating by changing the thickness of its layers. The general tendency which can be seen in Figure 5.3 is that the more alumina in a coating, the less the penetration depth so the better scratch resistance achieved. This is due to the difference of hardness between alumina and aluminum thin films. Following the basic rule of mixture, the more alumina in a compound, the higher its hardness. However, it will be shown in the indentation analysis that the hardness does not exactly follows a rule of mixture. But still, it will be higher when increasing the alumina content. The penetration depth and thus the scratch resistance is then inversely proportional to the proportion of alumina in a coating.

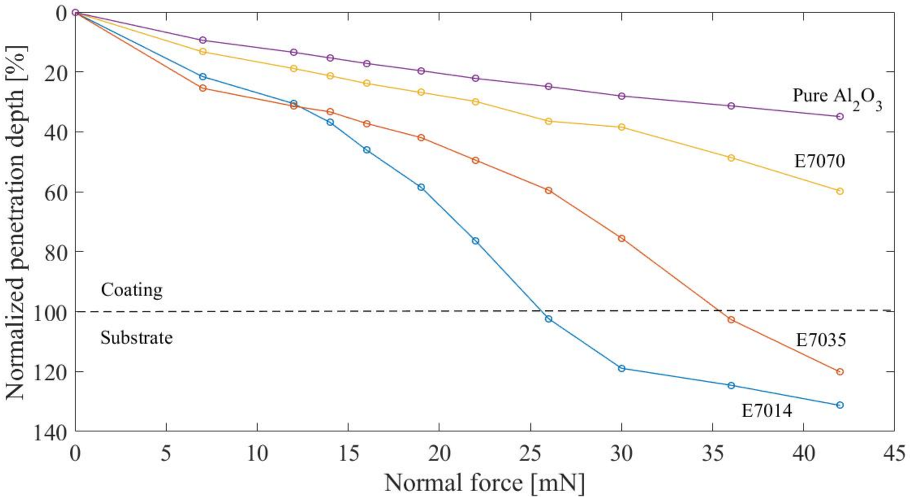

Figure 5.3: Normalized penetration depth with the total thickness of the coating vs normal loading force for different alumina content in the coatings

However, to achieve a good wear resistance, a coating should have not only a good hardness but also good toughness properties. [119] The abrasion resistance does not only relies on having a high L_c (leading to yield initiation) but materials must also have a good resistance to cracking after this initiation. In the present case, alumina shows the best scratch resistance properties which is coherent with literature stating that the materials with the highest material index[1] $\frac{H^3}{E^2}$ tend to show the best yield resistance. However, with other scratch tests input parameters, or other wear tests, the failure mechanisms could be dictated by cracking instead of yielding. The best material indices are then related to the fracture toughness, and metals seems to outperform ceramics. So further investigations on the fracture toughness properties of the different samples and other scratch tests would allow to compare the results to see if they match the literature. [20, 119]

---

[1] "Components have functions: to carry loads safely, to transmit heat, to store energy, to insulate, and so forth. Each function has an associated material index. Materials with high values of the appropriate index maximize that aspect of the performance of the component" - Ashby methods [20]

By looking more deeply at the curves, some interesting features can be seen. First, the pure alumina has a constant slope of penetration depth with increasing normal force, which is a normal behavior for elastic materials, showing that the alumina stays in an elastic regime.

Also, as these curves are normalized curves (the penetration depth is divided by the total thickness of the different films), it is shown that the samples E7035 and E7014 have higher penetration than their total coating thickness. They reach the substrate underneath. This is also seen on the curves by a change of the slopes when getting closer to the substrate.

Finally, the different laminates have several changes of slope in their penetration curve. In general, there is quite a big change of penetration slope before and after L_C (as shown further in this analysis), suggesting a change of deformation behavior in the laminates.

5.2.2.2 Influence of the aluminum content

The second parameter studied here is the influence of the proportion of aluminum in a coating by changing the thickness of its layers, and keeping the thickness of alumina layers constant. As for the difference between alumina proportion, changing the thicknesses of the aluminum layers shows the same tendency (as can be seen in Figure 5.4). Decreasing the thickness of all aluminum layers but not of the alumina layers de facto results in a higher proportion of alumina in the coating, giving a higher hardness value, and leading to a better scratch resistance.

However, it would be interesting to have more tests, in order to see how the layer thicknesses of aluminum really influence the results. As stated in the state of the art, there will be a certain layer thickness of aluminum for which the hardness will reach a maximum. Following equation Equation 3.8, the hardness follows a Hall-Petch relationship on the space between two ceramic layers. In order to see this effect, some tests at the extremes should be done.

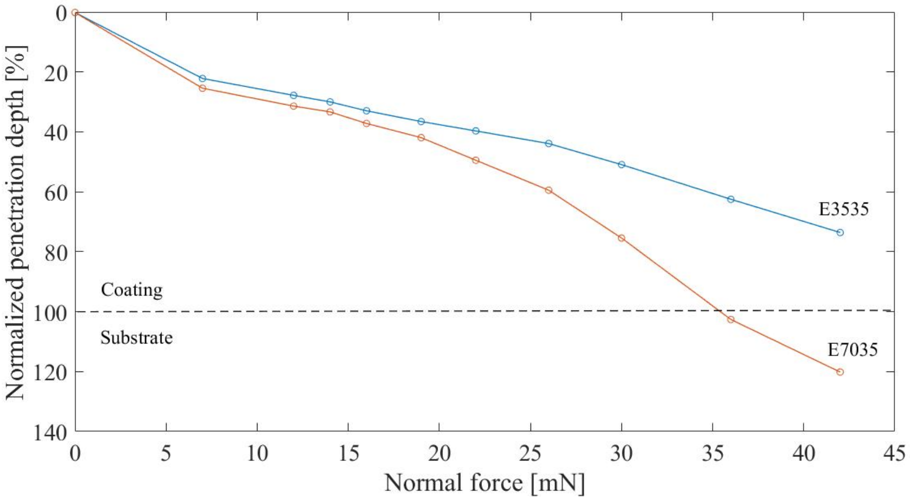

Figure 5.4: Normalized penetration depth with the total thickness of the coating vs normal loading force for different aluminum content in the coatings

5.2.2.3 Influence of the layer thickness

The last studied parameter is the influence of the bi-layer thickness. This is the thickness of one alumina and one aluminum layer together. Figure 5.5 compares two samples with different layer thicknesses, the thickness of all layers being 70 nm for sample E7070 and 35 nm for sample E3535. It shows that thinner layer thicknesses result in a higher penetration depth and thus is a lower scratch resistance.

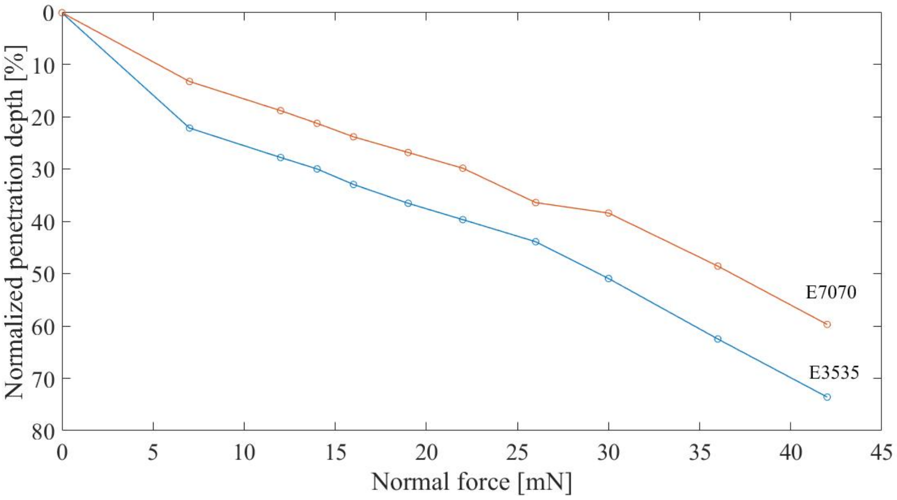

Figure 5.5: Normalized penetration depth with the total thickness of the coating vs normal force for different bi-layers thicknesses

In literature, scratch resistance of nanolayers diminishes with decreasing layer thickness, confirming the results obtained experimentally. Several explanation can be given to this layer-thickness dependence: [72]

1. The first explanation is related to strain hardening. As explained in the state of the art decreasing the grain size/layer thickness below one hundred nanometers in crystalline metals changes the mechanisms of dislocation motions. Grain boundary sliding starts to dominate over dislocation plasticity, lowering down the strain hardening associated with dislocation interactions. [120] This gradually decrease of dislocation activity, and consequently the gradually decrease of strain hardening in the range 10-100 nm gives that a 70 nm layer as a better strain hardening than a 35 nm layer.

2. The second explanation comes from an interface-dominated wear mechanism that occurs. Two main reasons lead to this promotion of interfacial sliding. Firstly, during the scratch test the compressive strain experienced by the coating increases. This induces large compressive stresses requiring excessive plastic flow. It is accommodate by the edges of the scratch track and thus geometrically promotes interfacial sliding. Secondly, the deformed cross-sections have some variations in layer thicknesses inducing a non-uniform compressive strain.

   The interfacial sliding increases with increasing number of interfaces. It is thus more important in sample E3535 in which the proportion of interfaces is higher than in sample E7070.

5.2.3 Critical load

As stated before, the critical load L_c is not a intrinsic value of the coating. It depends on the different extrinsic conditions used to measure it. However, for the same scratching conditions, it gives a good comparison value of the scratch resistance for different coatings. In order to find L_c a combined analysis with the graphs given by the nano-scratch and the SEM images was made. The general idea was to analyze the tendency of the scratch slopes and to match them with SEM images. The critical loads were taken as being the first discontinuity in the curve of the penetration depth versus scratch distance/normal force.

5.2.3.1 Finding L_c

The critical loads were found by looking at the simplified scratch tracks. These were made by taking a representative scratch, and can be seen in Figure 5.6. The first discontinuity is marked with a red line. These jumps correlates with the SEM observations in Figure 5.7. They also correlate with the friction jumps. The complete raw scratch track graphs and friction jumps can be seen in section B.1.

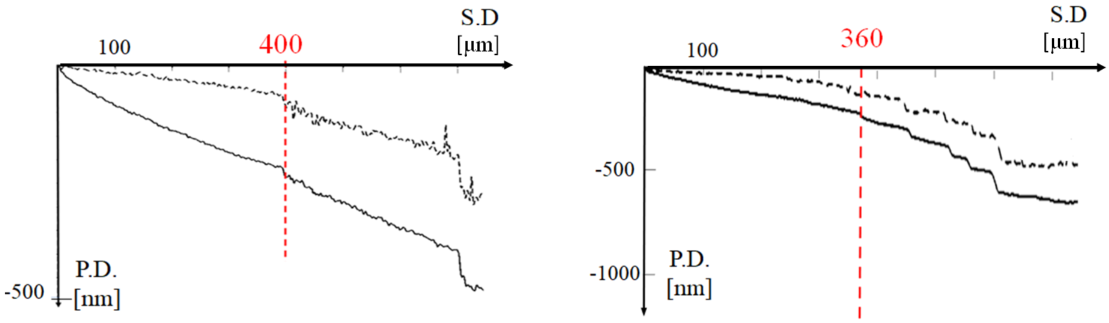

(a) E7070 (b) E7035

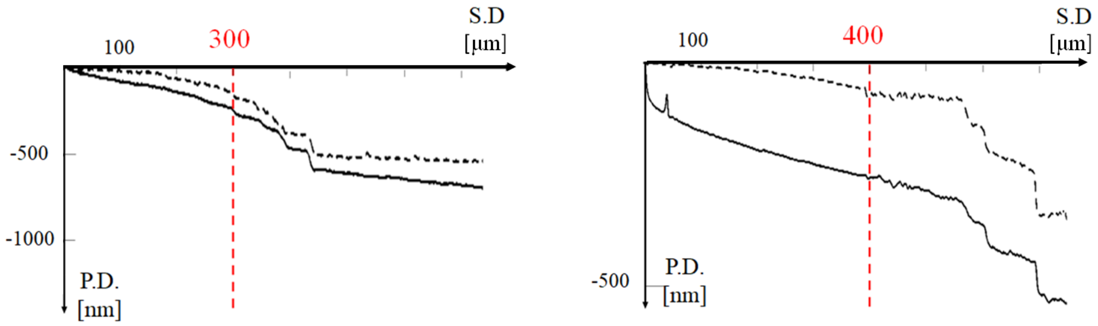

(c) E7014 (d) E3535

Figure 5.6: Simplified scratch tracks of the penetration depth (PD) versus the sliding distance (SD). The dotted lines represent the residual penetration depth while the normal lines represent the penetration depth during the scratch test. The red lines indicate the critical load of the different systems.

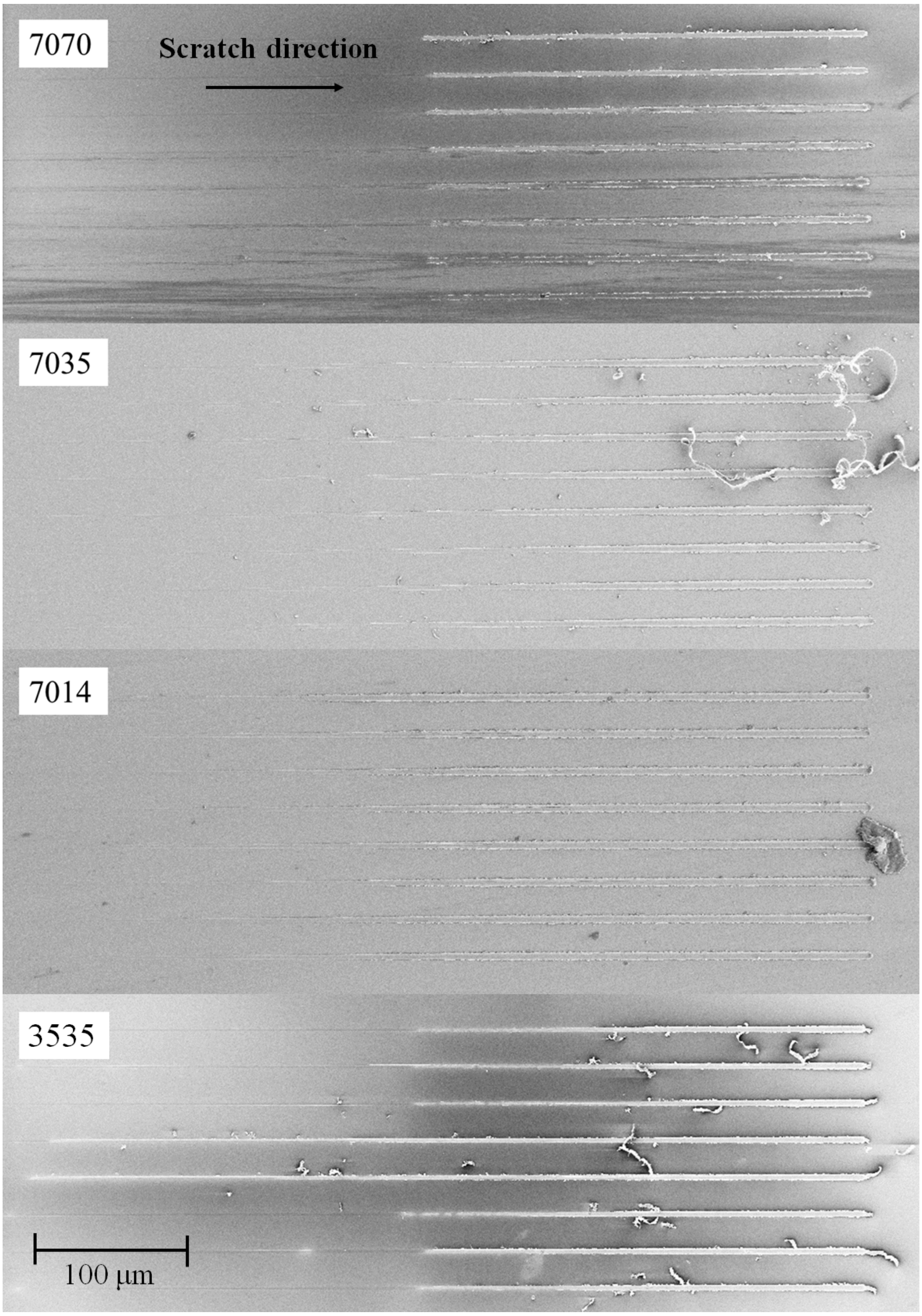

Figure 5.7: Scratches profiles of four different sample , taken with a magnitude of 150x and with an EHT of 4 kV. The detector used were in-Lens and SE2, and the images shown here are the best between the two.

5.2.3.2 Comparing the L_c

The mean values of Lc (obtained from the different scratch curves) are resumed in Table 5.1.

Table 5.1: Values of the critical load

Sample	L_c [mN]
Al_2O_3	/
E7070	24
E7035	22
E7014	18
E3535	24

Figure 5.8 shows a plot of the different L_c found for different proportions of alumina in the coatings.

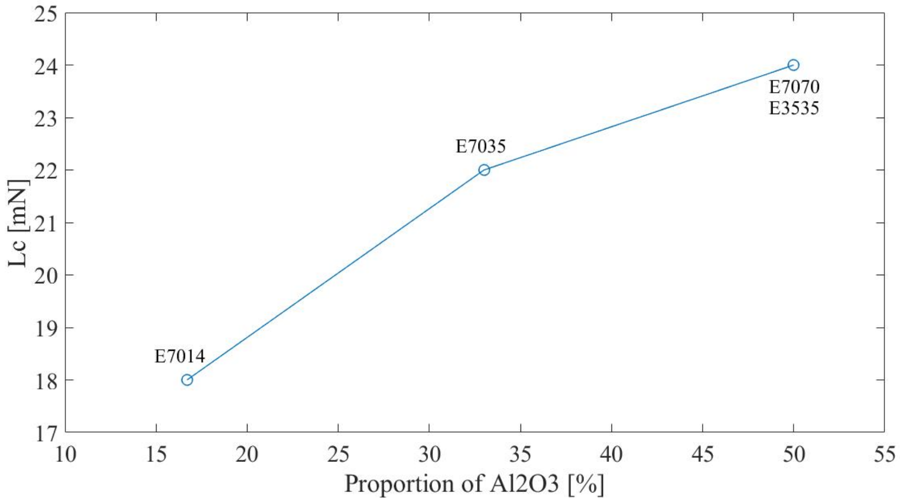

Figure 5.8: Critical load as a function of the proportion of alumina

The following observations can be made:

1. By increasing the alumina proportion in a coating, its critical load increases. This correlates to the scratch resistance found before. The reason is the same as for the scratch resistance: a higher alumina content brings a higher hardness leading to a better resistance to yield initiation.
2. The same L_c is obtained for E3535 and E7070. This was not expected as they do not have the same scratch resistance. More experiments are required to confirm of infirm this result.

5.2.4 SEM observations

To characterize the different scratch mechanisms which cause failure, some SEM observations were carried out. This subsection describes the phenomena appearing before and after the critical load along the scratch track on sample E7070. The scratches shown are taken after the post-scanning of the tip. The behavior of the coatings at the end of the scratch tracks are then compared.

5.2.4.1 Analysis of the scratch track

By looking at the scratch tracks, the different deformation mechanisms appearing during the tests can be observed. Figure 5.9 illustrates some phenomena appearing during the scratch test of the sample E7070. After a small elastic regime, where no residual deformation remains, some plastic deformation is observed. A bit further away, and near the critical load in the graph, there is some conformal cracking (5.9(a) [2]). The top layer remains fully adherent to the underlying one. As the indenter deforms the layer, it deforms the under laying layer at the same time, giving a lot of deformation to handle. After a while, the top layer cannot sustain the deformation anymore, and breaks (5.9(b)). This can be seen by the small jump on the graph of the penetration depth versus the sliding distance, and corresponds to the critical load. After this jump, some chipping occurs (5.9(c)). In fact, the top layer is taken of of the scratch track.

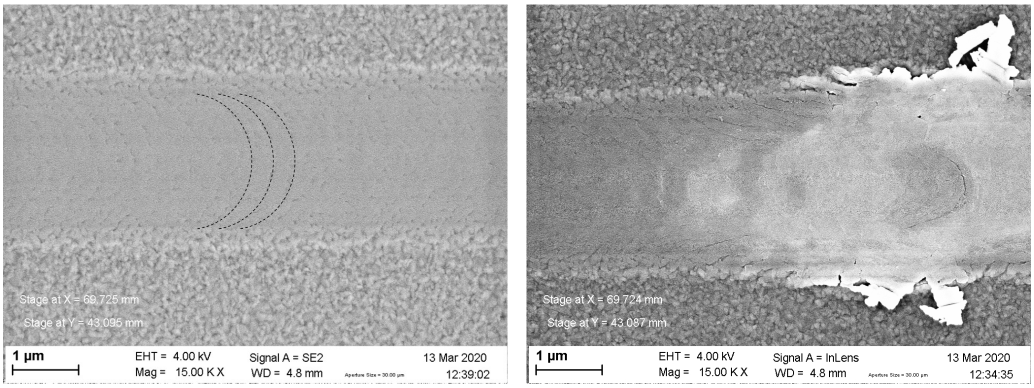

(a) Conformal cracking (b) L_c

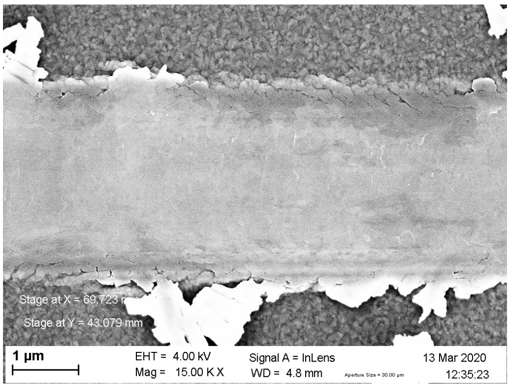

(c) Chipping

Figure 5.9: Different scratches mechanisms happening in sample E7070

---

[2] The three dotted lines have been added to the image to emphasize conformal cracking.

The same phenomena are observed in samples E7035, E7014 and E3535. The images can be found in section B.1

5.2.4.2 Analysis of the phenomena appearing at the end of the scratches

By looking at the end of the scratches, some information can be derived. In the figures 5.6(b) and 5.6(c) several jumps are observed in the tracks of samples E7035 and E7014. This can be explained by the breaking of the different layers of alumina. In fact, as can be seen on Figure 5.10 several layers of alumina and aluminum can be seen.

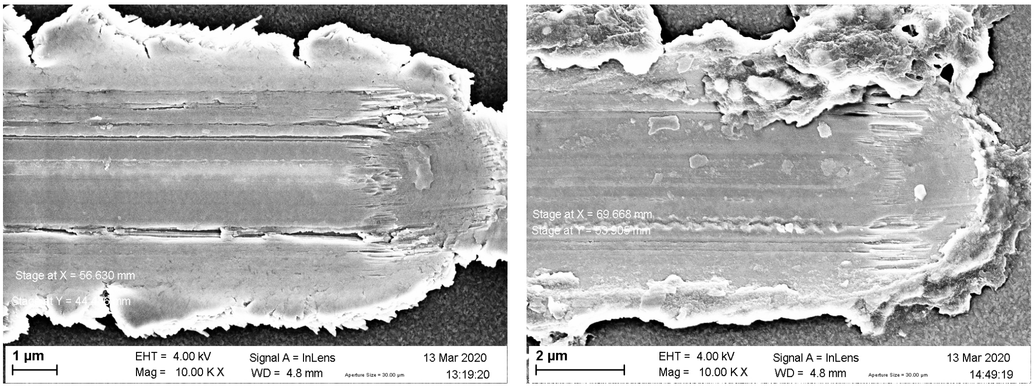

(a) Sample E7035 (b) Sample E7014

Figure 5.10: End of the scratch track with a view of the several layers

This phenomenon is not observed in E7070 and in alumina (as can be seen on Figure 5.11). While it is logical for alumina (not delamination and no L_c because the 700nm alumina layer was not broke during the scratch test). But for the aluminum layer, it would be interesting to see whether it is reproducible or not.

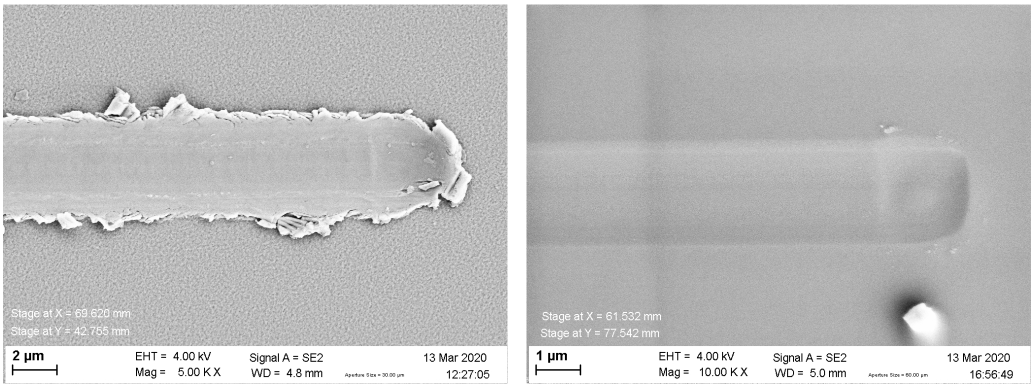

(a) Sample E7070 (b) Sample Al_2O_3

Figure 5.11: End of the scratch track with no view of the several layers

5.2.5 Plastic and elastic deformation

When looking at the scratch track in order to assess the scratch resistance, it is interesting to know whether the coating is deformed elastically or plastically. The scratch track can be divided into three main parts: elastic, plastic and damaged. In the first part of the scratch (above 90% of elastic recovery) the scratching can be considered as being fully elastic, and the wear resistance as perfect. The phase two begins when some plastic deformation occurs. To handle the deformation, the material deforms in a plastic way, until the deformation is too high for the coating to withstand. Some delamination or fracture is then observed, and the scratching is in phase three. This phase happens just after L_c. [104]

When looking at scratches, it is interesting to see which proportion of the deformation is elastic, and which one is plastic. The higher the elastic proportion of the deformation, the better the scratch resistance. In order to quantify this, three parameters were looked at: the elastic recovery, the elastic and plastic work at L_c and the volume of material that was taken away during the scratches.

5.2.5.1 Elastic recovery

The first parameter studied was the evolution of the elastic recovery. It measures the ability of a material to return to its original shape after the load is removed. It is given by:

$$\text{Elastic recovery} = \frac{\text{Total Penetration depth - Residual Penetration depth}}{\text{Total Penetration depth}} \tag{5.1}$$

where the residual penetration depth was measured by back-scanning of the track, and shows the plastic deformation in the material.

Figure 5.12 shows the evolution of the elastic recovery with the normal force for different proportions of alumina in the coatings. The global tendency is that a higher alumina proportion in a coating gives a higher elastic recovery.

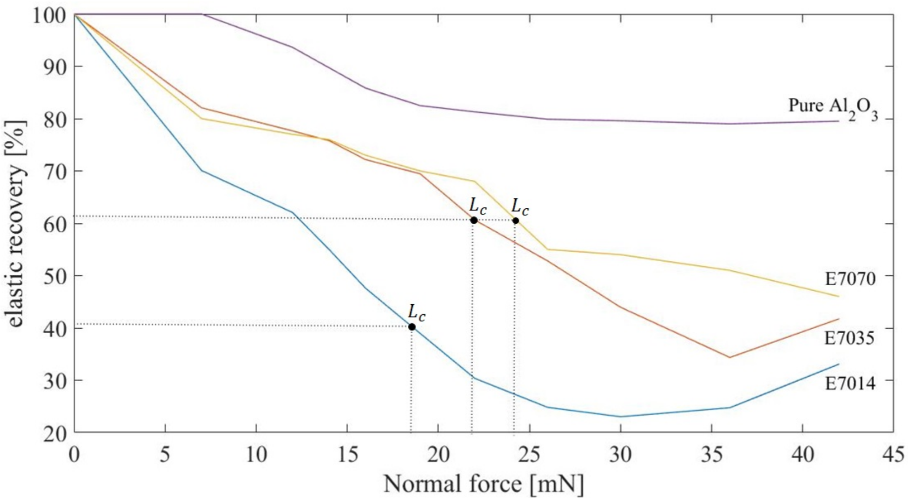

Figure 5.12: Elastic recovery vs normal force for different alumina content

By looking more closely at the graphs, some features can be seen. First, for pure alumina, the curve seems to reach a plateau value. Then, for the composites, some breaks in the curves with different slopes are observed. These are probably due to the different layers in the composite, and the elastic recovery is better when the tip is feeling the influence of an alumina layer.

Also, the critical load of the different sample are shown in the graph. If the difference in elastic recovery between just before L_c and just after L_c does not seem important, it is interesting to see that the critical load is generally located on the steepest slope, showing an important plastic deformation around L_c.

Finally, for the samples E7014 and E7035 the elastic recovery increases after a certain normal loading force, which is around 25 mN and 35 mN respectively. By comparing this to the penetration depth for a certain normal load (Figure 5.3), it is found that this increased value is due to the penetration of the tip in the substrate, where the elastic recovery is better than in the nanolaminate because the substrate is harder.

The other two parameters (difference in aluminum content and in bi-layer thickness) did not show any relevant comparison. They are therefore not shown here, but can be seen in Appendix B.

5.2.5.2 Work done during the scratch

The elastic and plastic work that was done just before the critical load is presented. It gives an idea of the total energy required to damage the sample. This was done by measuring the area under the load versus displacement. [121] It is given by:

$$W = \int P(x)dx \tag{5.2}$$

The total work done at the critical load is shown in Figure 5.13. The expected behaviour is that the higher the critical load, the greater the work to induce failure in the material. Also, the value of the total work depends mainly on two parameters: the ability of a material to deform elastically and plastically. For pure ceramics, for example, the total work to be done is mostly elastic, while for a metal, the work is elastic, then becomes plastic until failure occurs. This is what is observe here: the proportion of plastic work decreases when the proportion of alumina increases.

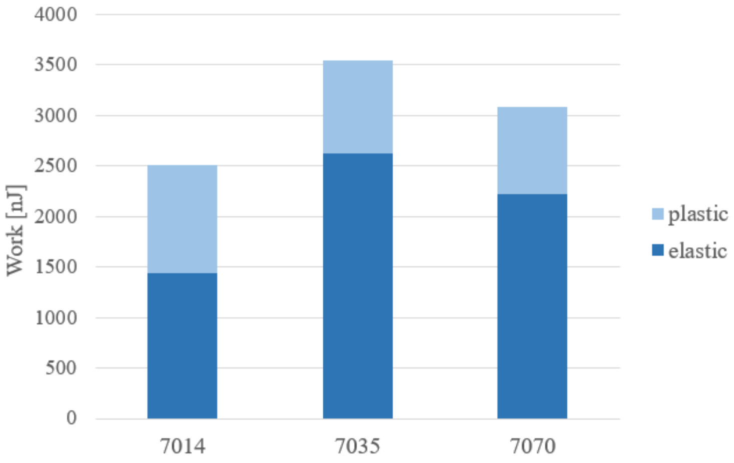

Figure 5.13: Work required to deform laminates up to their critical load value

The work done to induce damage in sample E7014 is lower than in E7070 due to the lower alumina layer on top of the sample. The reason why the sample E7035 is higher than the sample E7070 is due to a higher penetration depth with close L_c values. No conclusions were drawn from this observation, due to the imprecision of the model used to calculate the work, and the non-extensive number of results.

5.2.5.3 Wear volume

Measuring the wear resistance of a material by scratching allows to deduce an interesting feature: the volume that is taken away during scratch (the wear volume). It is a value which can easily be compared to the erosion of a particle under certain conditions. The largest volume remove, the worst erosion properties for the same eroding conditions.

The volume removed during the scratch can be derived from the measurement of the penetration depth as:

$$V = \int_0^x A(x)dx \tag{5.3}$$

where A is the contact area of the tip with the coating at a certain scratch distance x. One difficulty encountered to measure the wear volume is a precise definition of this contact area. During scratch, the deformations were made by a spherical tip so the contact area is the half of a spherical cap:

$$A(x) = \pi Rh(x) \tag{5.4}$$

where R is the radius of the spherical tip. However, in practice, there is some elastic recovery, so the quantity of matter removed is not as much as the one that could be measured with the total penetration depth. The contact area is then harder to define because it is a hypothetical one, relating to the remaining penetration depth.

Two theories can be taken in order to estimate this area. The first one, relatively basic, is to consider the same spherical tip, with only a smaller penetration (i.e the residual penetration).

The second one, estimates the contact area as having a ellipsoidal form. As can be seen on Figure 5.14, while the initial penetration follows the sphericity of the tip, the back-scratching (after the elastic recovery) is represented as being ellipsoidal.

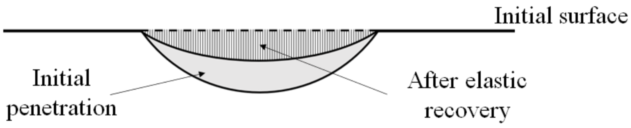

Figure 5.14: Cross-profile of the deformation shape due to the tip before and after elastic recovery

This can be derived mathematically as being:

$$A_e = A_s\alpha \tag{5.5}$$

where A_e and A_s are respectively the area in contact with the scratch of the residual scratching (ellipsoidal) and the initial scratching (spherical) and α is a correlation coefficient. This can be taken as being the elastic recovery at a certain distance x. However, this is an approximation because it assumes than the correlation between the sphere and the ellipse is constant.

The different scratch volumes removed for the two different methods are shown in Figure 5.15 and show similar curves.

If this gives a good overview of the volume of material that is removed during scratch, the interpretation must be done carefully. In fact, this theory is made of many approximations: the way of calculation the integral on a finite number of point and making the trapeze method or by estimating that all the volume is taken off of the scratch track when some of it is just plastically deform. However, it gives a good approximation, which can be used in further erosion investigations.

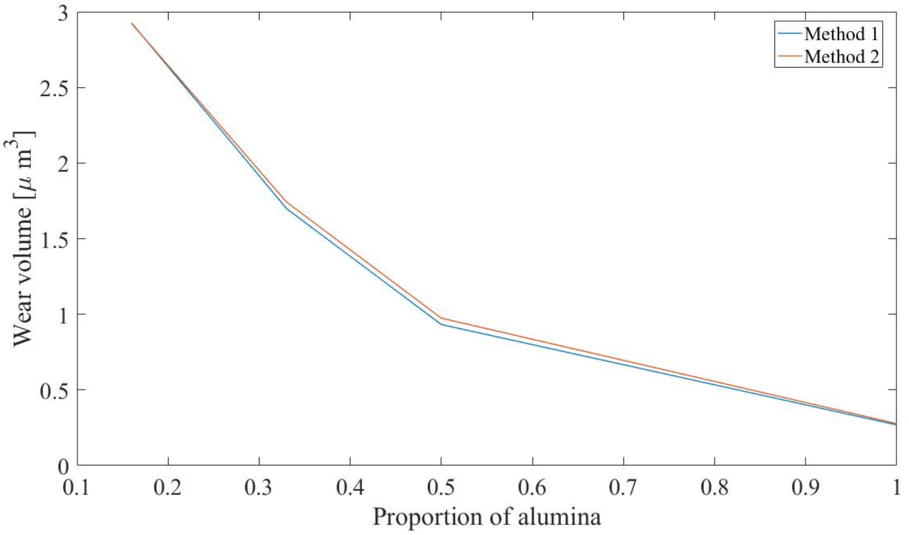

Figure 5.15: Approximation of the volume taken away during the scratch test following the two approximations of contact area calculation

5.2.6 Conclusions about the scratch analysis and plans for further investigations

This section presents the resistance to scratch of different experimental samples. The number of tested sample is very limited, but it still allows to gives some trends of the behavior of the nanolaminates. The results of this section can be summarised as follow: for all of the parameters studied here, the sample with the higher alumina content had the best properties.

Firstly, the penetration depth as a function of the load was investigated showing that the more alumina in a sample, the better its scratch resistance for the set of parameters chosen here. A comparison between two systems having an equal proportion of alumina but different bi-layer thickness indicates that thicker layer thicknesses show the best scratch resistance.

Secondly, the critical load, corresponding to the smallest load for which some failure occurs was determined for the different systems for specific loading conditions. The same tendency as for the penetration depth was found, giving that a higher alumina content gives a higher critical load. On the different bi-layers thickness however, the same L_c was found. As this was unexpected, the experience should definitively be repeated in order to take conclusions.

Thirdly, the failure of the systems was analysed via SEM observations. At the penetration depth investigated, the different coatings seem to keep fully adherent to the substrate, and to the underneath layer. In fact, the failure mechanisms observed were due to cracking in the layers and not to adhesion cracking modes.

Finally, the amount of material removed during the scratch test was investigated. This is the closest measure to an erosion test, and allows to quantify the wear resistance of a material. It shows that the more alumina in a sample, the less volume of material removed.

In order to obtain more information of the scratch test, further analysis should be made. One step is to go deeper in the material by applying a higher loading force. This would allow to go down to the substrate for all the systems, and to test the coating substrate adhesion directly. Also, changing the scratching speed, could give an overview of the scratch resistance under different loading conditions. These two steps would prepare the test of the coating on the erosion bench which represents a more realistic situation of wear.

5.3 Indentation analysis

Due to the COVID-19 crisis, the mechanical properties of the nanolaminates by indentation could not be gathered. Therefore, a simulation tool was used in order to have a more complete characterization of the nanolaminates, especially their hardness and their Young modulus.

In addition to providing these valuable data, the use of a numerical simulation makes it possible, after verification of the reliability of the tool, to study the variation of several parameters in order to guide to new experimental manipulations. In fact, it allows a more versatile, fast and cheap way of testing many different parameters.

In this section, the assessment of the reliability of the different used models is done. It is then followed by the analysis of the stresses and strain appearing during indentation and the determination of hardness and Young modulus of the different systems. An analysis of the influence of strain-rate sensitivity on the results in then discussed. The section finishes with a small review of the used models, and provides ways for improvement.

5.3.1 Reliability of the models

The results of the simulation will be usable, only if it is proven that the simulation can be trusted. First a convergence analysis has to be performed, and then the simulation results must be compared with experimental data.

5.3.1.1 Confidence in the first model through convergence analysis

When modeling finite elements, a finer mesh usually produces a more accurate solution. On the other hand, finer meshing increases the computation time. One question can therefore be asked: how to obtain a mesh that offers a good compromise between accuracy and consumption of computational resources? The solution is to perform a mesh convergence study. The meshing properties of the model are shown in Figure 5.16.

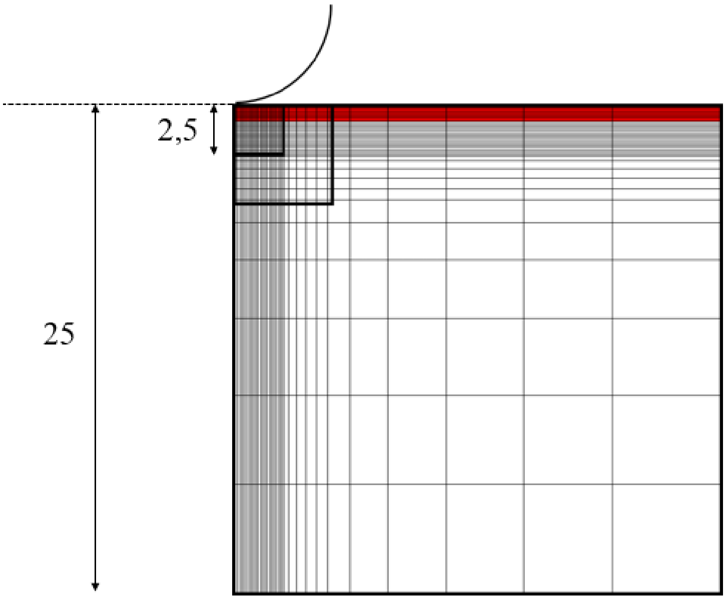

Figure 5.16: Meshing of the model (the red part represents the coating)

The meshing size of the different elements in the sections can be defined as follow: the central square has a meshing of x^2, the middle one from x to 0.1 and the bigger square from 0.1 to 10.

The tip is meshed with $2x$ in order to maintain the relation that the meshing of the top surface of the contact should be bigger than the one of the bottom surface (note that all the numerical values are given dimensionless). Figure 5.17 is a plot of the reaction force to the number of nodes. The simulation time was also plotted in order to have a idea of which model is the more efficient for this simulation. The number of nodes compared to the smaller mesh size x are shown in Appendix C.

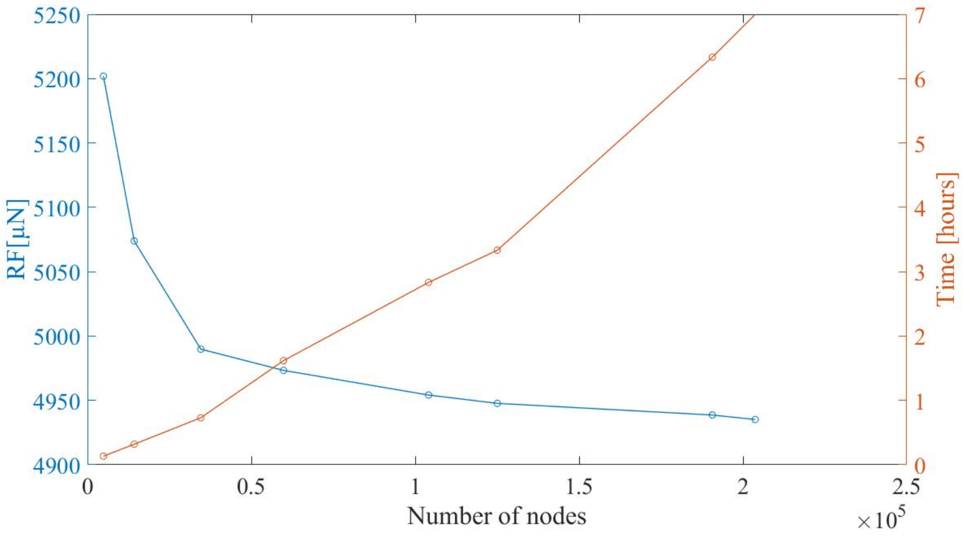

Figure 5.17: Convergence of the reaction force when refining the number of nodes

As expected, when the number of nodes increases, a refinement of the reaction force value is observed. In this master thesis, the minimal node size that was chosen was $x = 0,01$. Using this mesh, a total of 105,000 nodes were used, for a simulation that ran for about three hours, and an error in reaction force of less than one percent. The accuracy that can be achieved depends on the value being analysed. There will generally be a better accuracy on a force at a given location than on a main stress or hydrostatic pressure, because these sum the values of all individual elements, so they accumulate all the small differences.

To give a more solid foundation to the convergence study, the same work must be done for other quantities that will be analyzed later. There is no point in doing it on irrelevant quantities because the idea is to show that the results are reliable. In order not to start from scratch to perform this task, the simulation with the chosen mesh must be ran, and compared with the value of a more finely meshed model.

In this analysis, the parameters studied were those such that hardness and Young modulus could be determined. These were the reaction force as mentioned earlier, and the contact area. However, the measured value for the contact area in the convergence study, although showing less than one percent error and confirming the confidence in the mesh used, was performed with an Abaqus area calculation method which is not clearly defined (more information on this can be found in Appendix C).

5.3.1.2 Trust in model 2: Comparison with experimental datas

No convergence analysis was made on this model. However, some berkovitch indentation were done experimentally to compare them with the simulation results. These can be found in Appendix C.

The plot in Figure 5.18 shows that until 5% of penetration (35 nm into the surface), the two curves have the same behavior. After that, the experimental results show a higher load than the simulation for the same penetration depth, leading to a difference of about 30% at 10% of penetration (70 nm into the surface). These differences may be due to an incomplete definition of the material input parameters in the simulation (there is a certain strain hardening in aluminum which is not taken into account in the simulation).

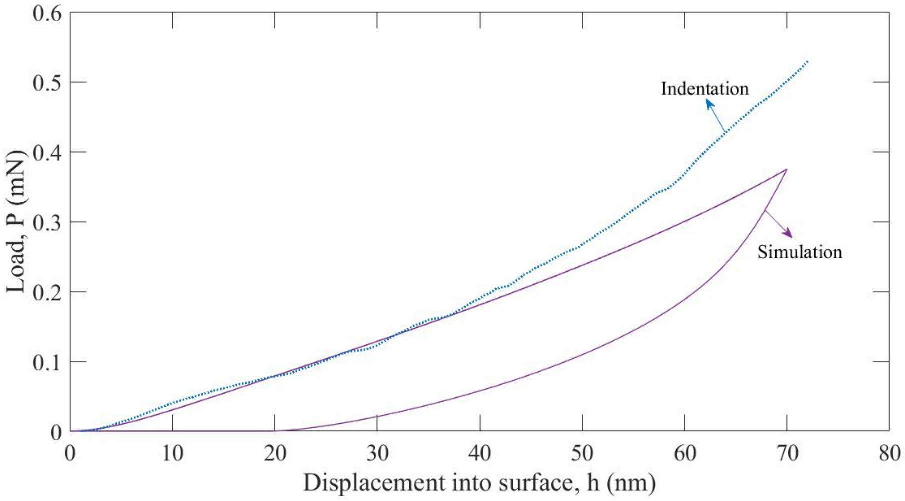

Figure 5.18: Comparison between the experimental indentation in the sample E7070 and the simulation realised (S7070)

In order to obtain a better correlation between experimental results and simulation, a few points should be improved. On the one hand, the simulation input data and parameters should be slightly modified in order to better fit the experimental model (indeed, it was seen in the microstructure analysis that the alumina and aluminium layers were actually 65 nm and 75 nm thick respectively). On the other hand, in order to be able to compare the measured data, the experimental system and the numerical model should be indented at the same depth.

5.3.2 Spherical analysis

The first indentation simulation was performed using a spherical tip of 5 μm. This was the same tip as the one used for scratch in order to compare the deformation mechanisms appearing during scratch and indentation.

In this section, the values plotted are the one obtained with the model developed at UCLouvain [107] because a better determination of the contact area was achieved. However, the comparison of the indentation loads for a certain displacement of the two models are shown in Appendix C, and show that both simulations can be used with confidence because the results are very similar.

5.3.2.1 Projected area

The projected area plays a very important role in the determination of the properties of a material. For a spherical tip, the Hertz model gives a lower boundary to the model and describes the contact between two elastic objects. It states that the surface area increases with the penetration due to the geometry which is initially a punctual contact and increases with depth. The projected area radius can be approximated by:

$$r_c^2 = Rh \tag{5.6}$$

Several assumptions are made whien using this model. Hertz model describes the deformation of two spheres of radius R_1 and R_2. The present case represents the limit case of a ”rigid sphere indenting an elastic half-space.” Also, Hertz calculation is based on the assumption that the contact radius r_c is small compared to the radius of the sphere, that is $r_c < R$, implying that the deformation of the sample must be much smaller than the radius of the sphere, $h < R$. This is the case for a 5 μm sphere, so the Hertz model can be used to obtain an idea of the indentation value which should be found. [122, 123]

However, in practice, the laminates are not perfectly elastic materials. There is some plasticity in the multi-layers, which creates some pile-ups at the edges of the indenters, increasing the contact area. The pile-ups are due to the deformation in the aluminum layers, leading to higher projected surface area for the sample with more aluminum. This is shown in Figure 5.19.

5.3.2.2 Evolution of the load

As explained earlier, the two main measurements taken in an indentation test are the reaction force of the material against the penetration of the tip at a certain indentation depth. Figure 5.20 shows the plot of the load as a function of the penetration depth.

The first observation that can be made on this graph is that for the same indentation depth, the force to be exerted by the indenter will be higher when there is more alumina in the sample.

5.3.2.3 Evolution of the hardness

Figure 5.21 shows a plot of the hardness as a function of the penetration depth for a spherical tip.

At the very beginning of the indentation, the different systems follow the same linear indentation curve. This is due to a very small contact of the spherical tip. Further in the graph, the systems show an linear evolution of the hardness with indentation depth.

In the films studied here, no visible stable region of constant hardness is observed. This is due to the geometry of the tip. Indeed, during spherical indentation, the hardness is never constant even for a homogeneous material because the tip is not geometrically similar. The

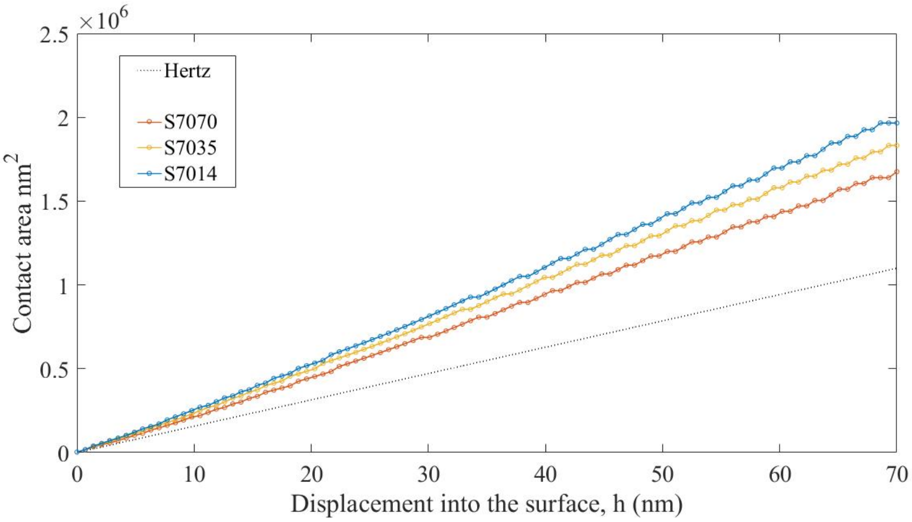

Figure 5.19: Projected area of contact for the different simulation systems, compared to the Hertz's model

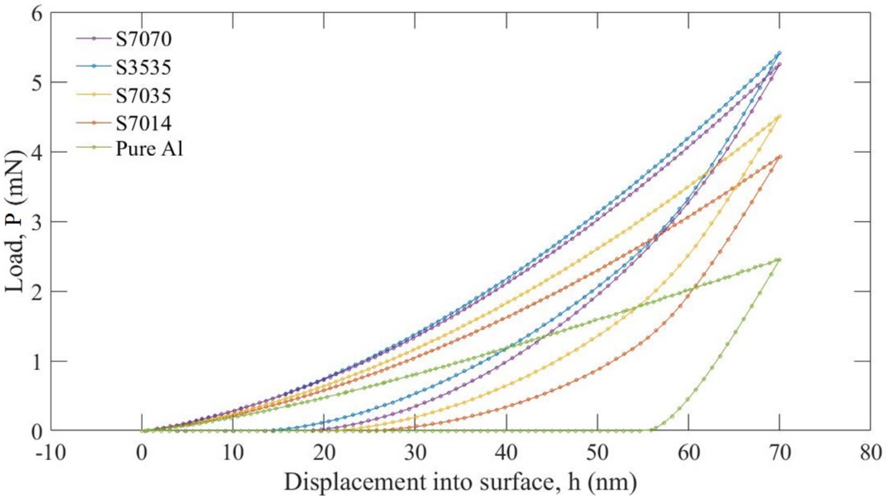

Figure 5.20: Load as a function of the penetration depth for different alumina contents and bi-layers thicknesses for a spherical tip

representative deformation increases with the depth of indentation, whereas for a conical or pyramidal (Berkovitch) tip it will have the same geometry regardless of the depth of contact. In the latter case, if the material is homogeneous, the hardness will be constant.

To confirm this theory, a larger displacement into the surface was made to see if the hardness values tends to reach a plateau. At 50% of indentation the hardness was still increasing linearly. Also, several indentation were made with a smaller tip radius, leading to the same conclusions. (All of these graphs can be found in Appendix C). This shows the interest of using a Berkovitch tip in order to obtain more accurate values of the hardness and the Young modulus.

5.3.2.4 Stress and deformation field under indentation

The following paragraphs present the evolution of stress and deformation fields inside the layered system during indentation loading. The purpose is to have a better understanding of the field

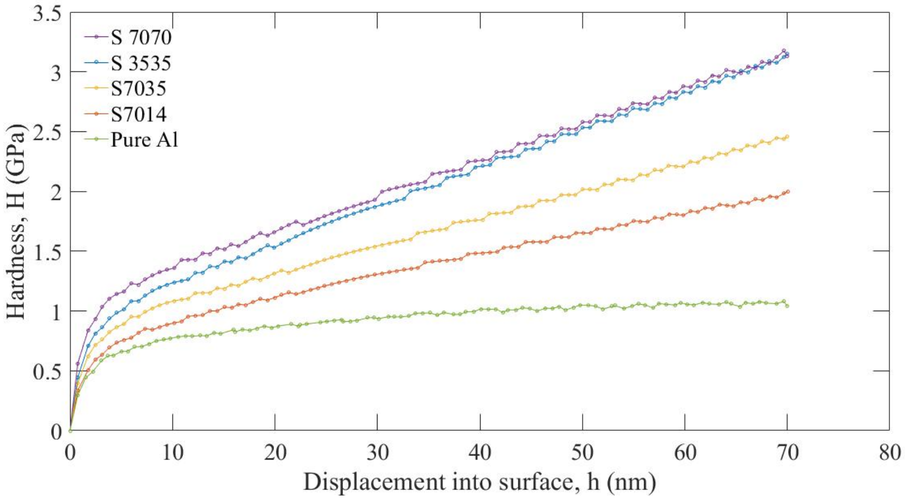

Figure 5.21: Hardness as a function of the penetration depth for different alumina contents and bi-layers thicknesses for a spherical tip

taking place in the heterogeneous structures.

Stress under indentation Directly under the indentation contact, large compressive hydrostatic stresses were generated within the Al layers. The hydrostatic stress can be defined as the average of the three normal stress components of any stress tensor:

$$\sigma_h = \frac{1}{3}(\sigma_{11} + \sigma_{22} + \sigma_{33}) \tag{5.7}$$

As can be seen in Figure 5.22, the compressive magnitude stress in the Al layers are much greater than those in Al_2O_3 due to the difference in plastic yielding response of the two materials.

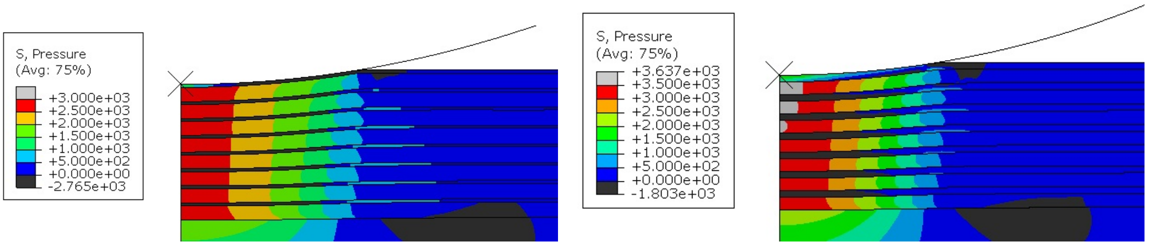

(a) System 7014 (b) System 7035

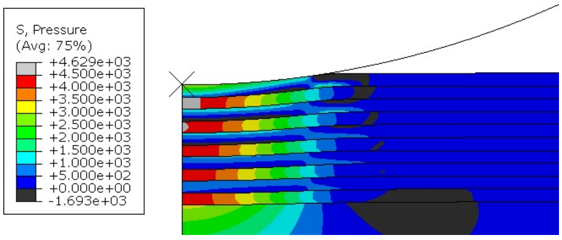

(c) System 7070

Figure 5.22: Hydrostatic stress in MPa near the indentation site. Due to a higher aluminum content the compressive stresses in the layers are lower in (a) than in (c).

However, if the Al layers are under high compressive stress under the indenter, significant tensile stress have developed in the Al_2O_3 layers (they bend due to elastic plate bending). These tensile stresses have contributed reducing the hydrostatic compression compared to Al.

Figure 5.23 shows the Von-Mises stress field at a penetration of 10 % of the total depth, having set a threshold at the plastic level of aluminum (350 MPa). It is clear that the aluminum is in a completely plastic state below the indenter, and that the stresses present in the alumina are very high. Also, the substrate encounters large stresses, showing its influence on indentation data.

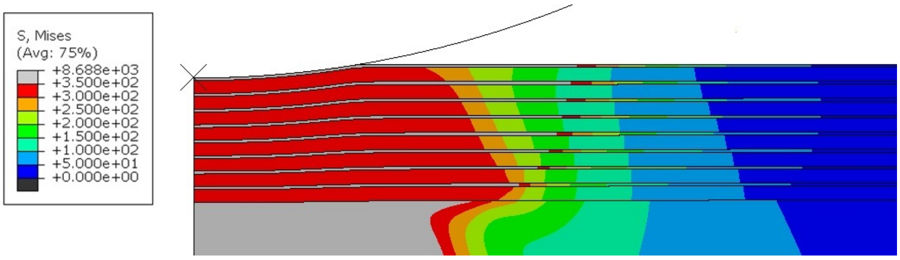

(a) System 7014

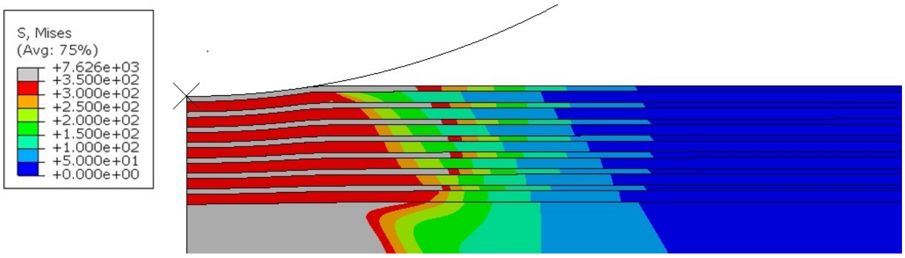

(b) System 7035

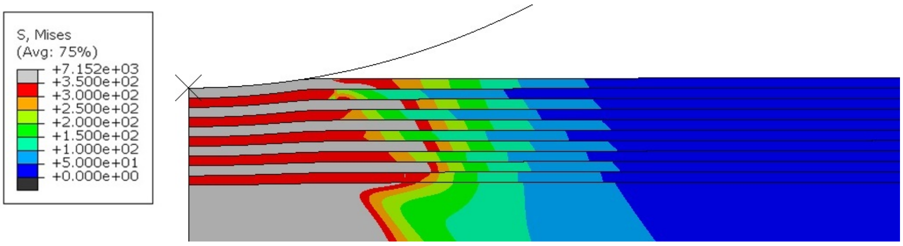

(c) System 7070

Figure 5.23: Von Mises stress in MPa near the indentation site

The value of the equivalent stress $\bar{\sigma}$ is higher in alumina for the system with the smallest alumina proportion (5.23(a)). If alumina was not simulated as a perfectly-elastic material, some cracking would occur firstly in this system. However, it has been shown in the state of the art that lowering the layer thicknesses of the amorphous layers tends to enhance their ductility. So further investigations are required to study this dependence.

Plasticity under indentation The soft layers have undergone severe plastic deformation, as can be seen in the Von-Mises constrain analysis. At the beginning of the indentation, the plastic strain is concentrated under the tip. After a certain penetration depth, the plastic strain tends to concentrate at the interfaces between alumina and aluminum, but not just under the tip. The higher concentration in plastic strain is between the substrate and the bottom layer of the multilayer.

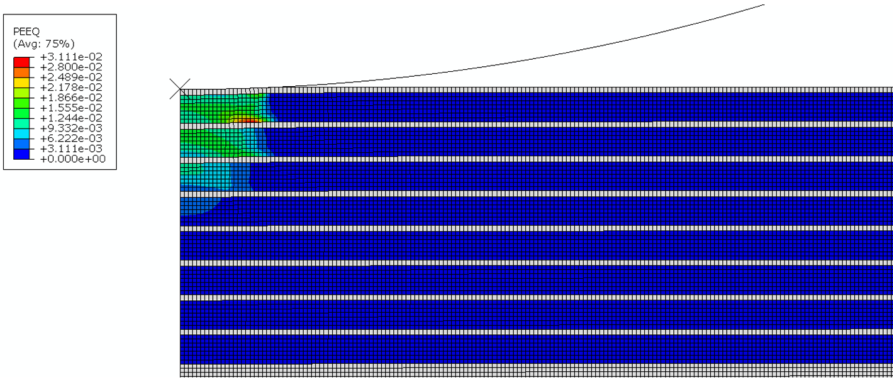

(a) Beginning of indentation

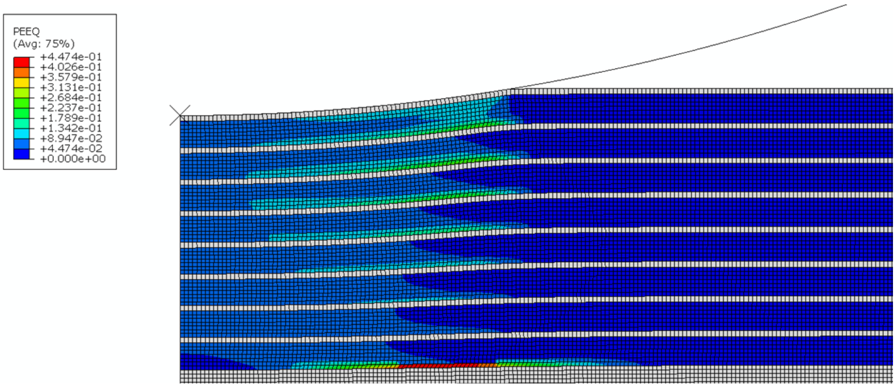

(b) After 10% of indentation

Figure 5.24: Equivalent plastic strain (PEEQ) near the indentation site for the simulation on S7014

The equivalent plastic strain is useful to understand the mechanisms appearing in scratch. Indeed, the concentration of strain at the interface is the reason why some adhesion failure occurs in scratch. However, in the results presented for the scratch test, no adhesion failure was shown. To have an overview of the total plastic strain at the interface during the scratch test, some deeper penetration into the material in indentation are required.

5.3.3 Berkovitch analysis

The Berkovitch indenter gives some more accurate values of the hardness and the Young modulus than a spherical indenter. In fact, the plastic deformation is more localized than in spherical analysis, as illustrated in Figure 5.25, and can be seen with simulation in Figure 5.26.

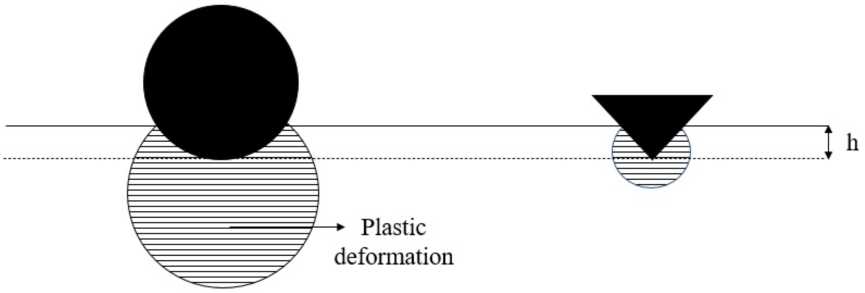

Figure 5.25: Influence of the tip on the plastic zone in the material induced by indentation

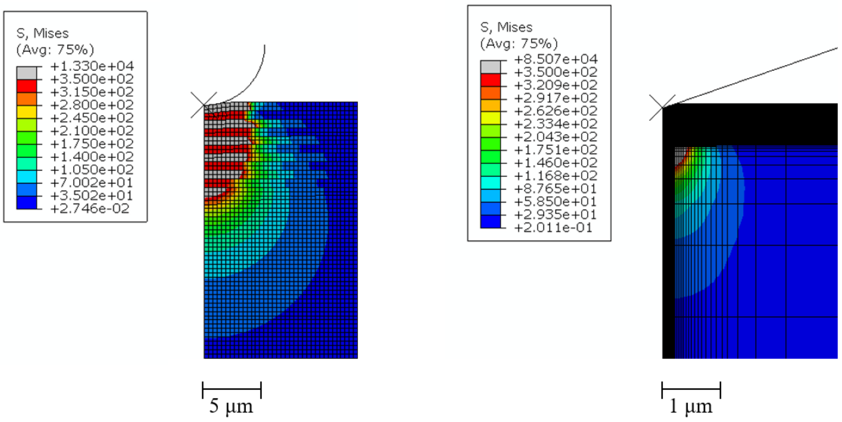

Figure 5.26: Influence of the tip on the plastic zone in the material induced by indentation for a same penetration depth for the system S7070 showing a larger plastic deformation with the use of a spherical tip

As for the spherical analysis, the graphs presented here were made by the models made with the inp generator. The accuracy of the model was verified with the system S7070, which will be used for further analysis. The comparison may be found in Appendix C.

5.3.3.1 Evolution of the load

In Figure 5.27, the load as a function of the penetration depth is shown.

As for the spherical simulation, a higher alumina content in the sample induces a higher deformation load to have a same displacement into the surface. The load is much lower than for a spherical indenter due to a much smaller surface area in contact with the material.

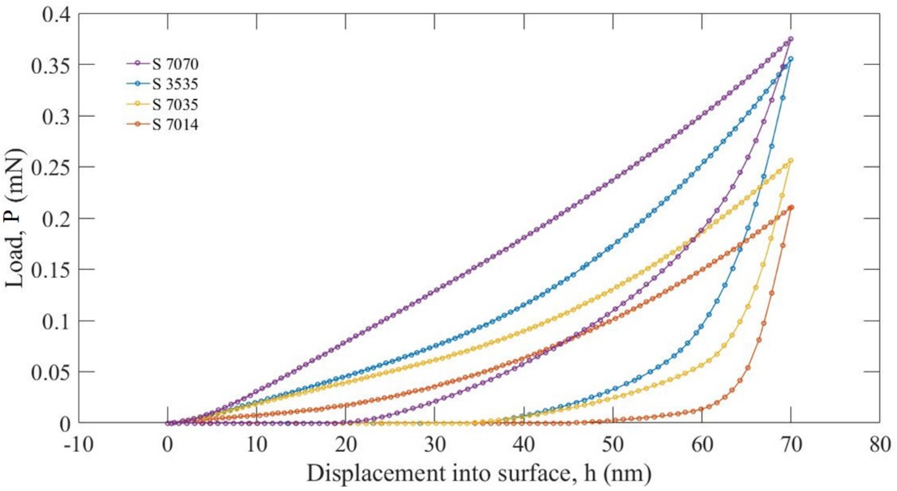

Figure 5.27: Load as a function of the penetration depth for different alumina content for a berkovitch tip

5.3.3.2 Projected area

Here-under is a plot of the projected area obtained by simulation made with the graphical interface, with the inp generator, and the two boundaries (Loubet and Oliver) comparing them.

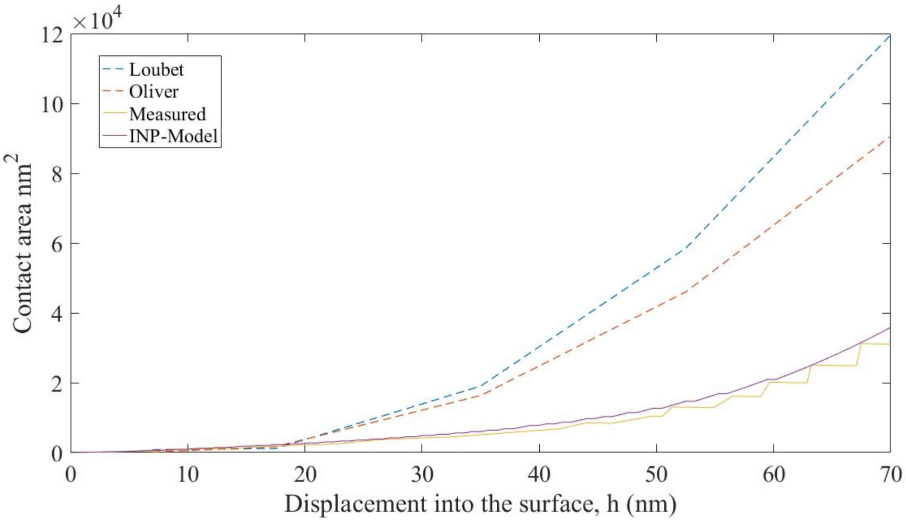

Figure 5.28: Projected contact area for the different simulation systems, compared to Loubet and Oliver and Pharr's models

The results seem surprising because in two different simulations, the contact area is not between the two models when normally this should be the case. This is due to a special case. Indeed, in the situation with the model containing 70 nm alumina and 70 nm aluminium layers, the situation is similar to that of an elastic membrane on a soft substrate. In this case, neither Oliver and Pharr nor Loubet work. This is normal because the main assumption for these models to be applied is that the material is homogeneous on the scale of the indentation, which is not the case here. Better comparisons should be obtained by looking at simulations on pure aluminum.

5.3.3.3 Evolution of the hardness

Figure 5.29 shows the evolution of the hardness with the penetration depth, and Figure 5.30 shows the evolution of the hardness with a penetration depth normalized by the top alumina layer. These graphs also show the hardness of pure aluminum and alumina. In the simulations the hardness of alumina is around 30 GPa because the model of the material is taken as purely elastic. In reality this is not the case. The hardness of PVD pure alumina has been determined experimentally, and the value of around 10 GPa has been found. [96, 116] The hypothesis of purely elastic behavior of the alumina film is then not verified.

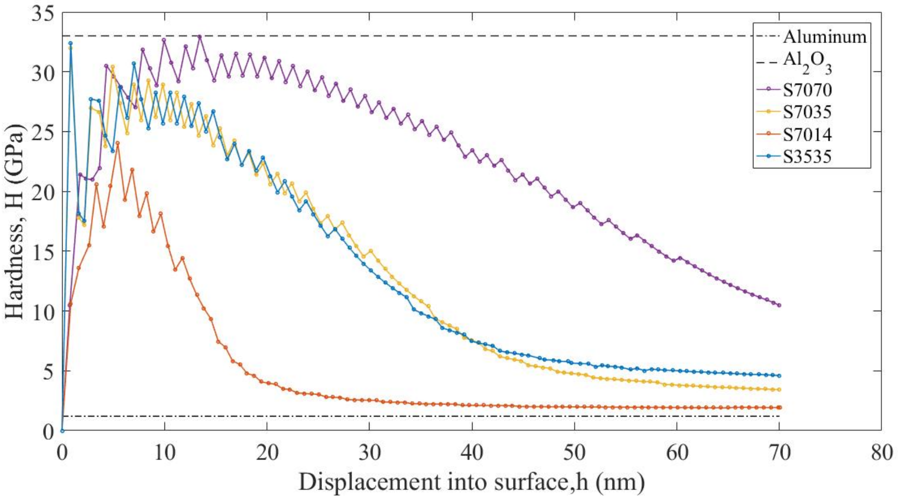

Figure 5.29: Hardness as a function of the penetration depth for different alumina contents

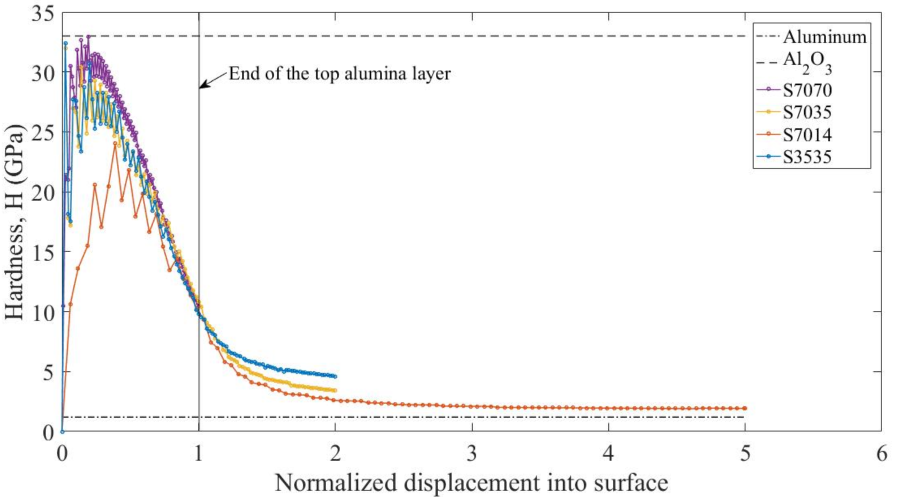

Figure 5.30: Hardness as a function of a normalized penetration depth with the first layer of alumina for different alumina contents

The general tendency of these two graphs can be described as follow: at first, the hardness is really high. This is due to the top layer, which is alumina and has a high intrinsic hardness. The value found here is indeed close to the alumina simulated value. After a certain value (different for the different system), a big drop is observed. The aluminum layer which is under the top alumina layer begins to play its role, lowering the hardness value. After this drop, the values seems to reach a plateau which is the value of the hardness of the nanolaminates.

By looking at the different curves, it can be deduced that the more alumina in a sample, the higher its hardness, and the thinner the alumina the faster the plateau value is reached. This can explain the differences between S3535 and S7070, and why the plateau is reached in the thinner layers and not in the thicker ones. In order to compare the plateau values, it could have been relevant to go deeper into the material. This has been done in section C.3.

Also, on the comparison between S7035 and S3535, the two systems follow the same slope at the beginning because of the same top thickness of alumina. After a while, they both feel the effect of the aluminum layer underneath, and S7035 will reach a plateau value lower than the one of S3535 because of its higher aluminum content. In practice, the thickness of the aluminum layer should also have an influence because it is the soft layer that generally induces the size-dependent mechanisms. Plastic deformation starts in the soft layer via dislocation until these are induced in the harder layer. For hybrid composites, confining the soft (crystalline) layer decreases its grain size and increases the density of interfaces. Therefore, decreasing the aluminum layer thickness should tend to increase the hardness. [72, 124]

5.3.3.4 Elastic modulus

Figure 5.31 shows a plot of the elastic modulus value found during simulation for different alumina content. The Young modulus of the different systems are between the value of pure alumina and pure aluminum. They are compared to the isostress and isotrain models.

Normally the isostress model should be the true composite value when loaded along the indentation direction. However, the loading is not in perfectly uni-axial conditions. Some lateral forces due to the geometry are present, giving an hybrid loading to the systems. The two approximations of the Young modulus (isostrain and isostress) are taken under uni-axial loading, they do not take into account the lateral deformation constrain due to Poisson effect. However, they give a good approximation of the values. [35]

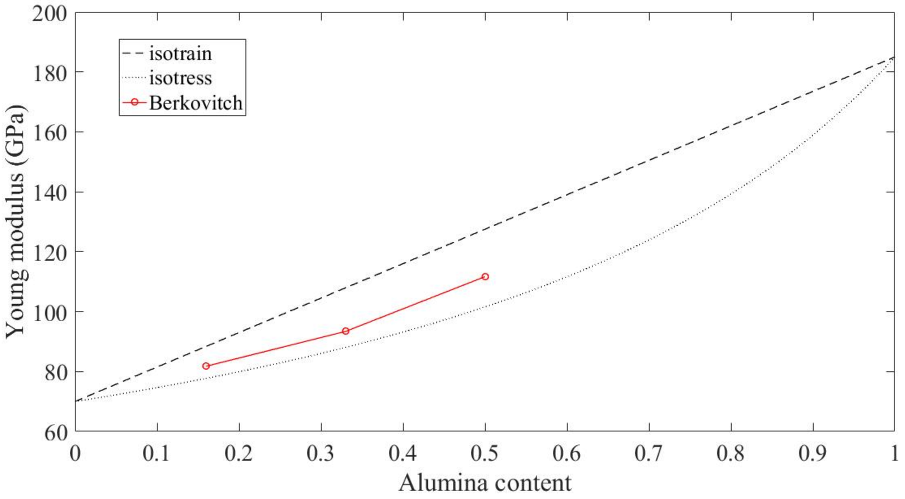

Figure 5.31: Evolution of the Young modulus with increasing alumina content, compared to the isostress and isostrain models for a penetration depth of 10%.

These two models have been numerically verified in literature by [125] confirming that the modulus and hardness measures in the direction parallel to the layers was shown to be greater than in the perpendicular and inclined directions.

5.3.4 Influence of the strain rate sensitivity

Because the final goal of the research is to analyse the erosion properties of nanolaminates, it is interesting to see how the material will behave with different strain rate, as in real life, the impacts done by erosion will be fast. To study this effect, the influence of the strain rate on the response of a material was measured.

The strain-rate sensitivity influence was measured on S7070 for a range of values. However, Figure 5.32 shows that with a difference of strain-rate on the order of 10^{-5}, no significant influence on the hardness is seen.

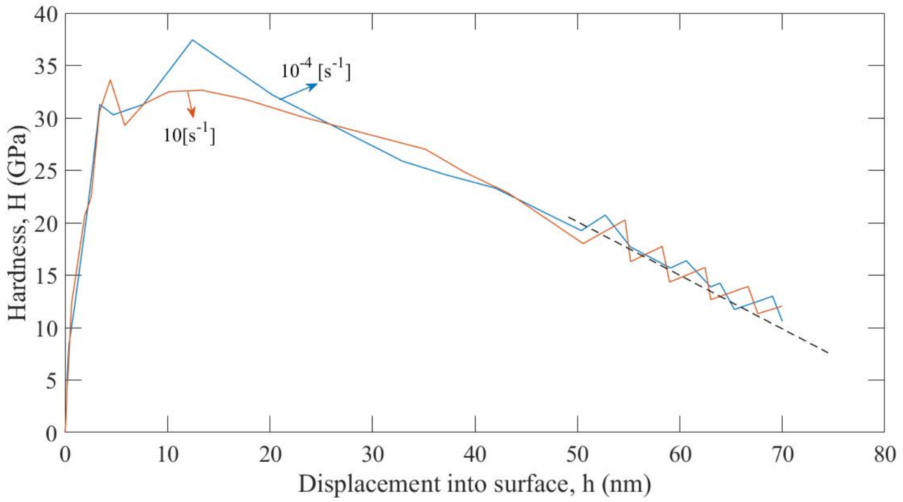

Figure 5.32: Evolution of the hardness for several deformation rate for S7070

In order to see if it was a disfunctioning of the used model, a comparison with some extremely rate-sensitive parameters was made, showing that the hardness was not influenced a lot by the strain-rate sensitivity of the aluminum (as illustrated in section C.5).

Some experiments were also made on pure aluminum, but the results were not relevant so they will not be further discussed. However, they are commented in section C.5.

5.3.4.1 Critics about the used model for the determination of the strain-rate sensitivity

The previous results do not allow a real analysis of the effect of the variation of the deformation rate on the hardness, despite the very wide range of deformation rates used. Before conclusions can be drawn about the results found, it is first necessary to criticize the model used in order to see if it is generating wrong results, or if the nanolaminate S7070 is non-sensitive to the deformation rate.

The model can in fact be criticised from several regards. First of all, the meshing would require better refinement to gain precision on the results. If the mesh is not refined enough, there is not a sufficient difference in the contact area and therefore the hardness is only slightly changed between the different indentations.

Secondly, it is the system chosen in itself that is not relevant for this analysis. Indeed, the choice of the S7070 system was made because it was the nano-laminated model that had shown the best scratch resistance and mechanical properties, and therefore seems to be the best choice for future use. However, it has been shown that at a penetration of 10% into the sample, this model does not yet show a hardness plateau. It is therefore difficult to compare the exact hardnesses as a function of the deformation rate, as only trends between the different slopes can be observed here, and these look very similar.

Also, the plasticity model that was chosen here was not perfectly adapted to the situation. Cowper-Symonds is a model that allows a good comparison of the variation of deformation rate when the deformation rate is high (i.e. for a dynamic indentation). In is not suitable for very low strain rates. In fact, there is a high increase of the yield stress for very low strain rates while in practice it is not the case. It would therefore be worthwhile to choose a model that better reflects the yield stress variation.

Finally, a very accurate model is necessary because in reality on indentation machines the deformation rates are limited to values between 10^{-3} and 1 [s^{-1}]. This is due to the thermal drift limit for the lower bound and the system dynamics for the upper bound. [3]

5.3.4.2 Strategy to measure the strain-rate sensitivity influence

In order to obtain more relevant results, it is important to think about a measurement strategy. This is developed below, and consists of three steps:

1. The first step would consist in confirming the value to strain rate sensitivity of PVD aluminum layers by experimentally measuring it. This step includes the measure for different aluminum layer thicknesses, in order to see if nanoscalling aluminum has an influence on its strain rate sensitivity. A simple model for the variation of the yield stress for several strain rates can then be build and entered as material properties in Abaqus.

2. The second step would then consist in refining the model to match to these experimental values. Once done, the strain-rate sensitivity of the overall model with several layer thicknesses can be investigated.

3. Finally, the strain-rate sensitivity of alumina should be measured the same way, in order to input its influence into the material properties.

By proceeding this way, and by having a more refined mesh, the study of strain-rate sensitivity should then be simulated more accurately, and conclusions could then be drawn.

---

[3] This is the case for the indenter that is used in the scope of this master thesis, but some nanoindenters allow to go up to deformation speed of $1000s^{-1}$.

5.3.5 Critics about the models

The developed models presented in this section are a first step into the numerical simulation of the mechanical properties of nanolaminates. They contain many assumptions, and the models need to be refined to best fit the experimental results so that they can be used as a basis for building a new design of experiments. This small subsection describes all the assumptions that were made which will need to be corrected to refine the numerical simulation.

1. The first and big assumption that was made relies on the definition of the material properties. In fact, the material parameters which are chosen are quite limited. First, it assumes that the strength in the aluminum layer will be the same regardless of layer size. However it has been demonstrated through Hall-Petch, and inverse Hall-Petch that this will not be true. So by changing the layer thickness, attention should be given to the change of material properties. Also, aluminum was taken as an elastic perfectly plastic material and the other materials were taken as perfectly elastic which is not realistic neither (as it has been proven with the difference in hardness value), and do not allow the study of parameters such as material failure.

2. Also, in the construction of the model, certain assumptions were made. The indenter was considered to be totally rigid, which in practice is not quite the case. However, it is a hypothesis which reduces enormously the calculation time and is not the most limiting from the result point of view. Also, perfect interfaces have been simulated, whereas in practice this will not be the case due to experimental imperfections. Moreover, the layers were considered to be homogeneous whereas in practice they have a certain texture due to the grain joints and grains, influencing the properties.

3. Finally, in real deposited samples, the layer geometry of the nanolayers is imperfect, and the wavy appearance will influence the properties of the nanolaminates. So in practice, both the indentation depth and the phase of the waveform have an influence on the Young modulus and on the hardness. [22]

5.3.6 Conclusions about the indentation analysis and plans for further investigations

The purpose of this section was to determine the Young modulus and the hardness of the different systems with numerical simulation. Several models with different goals were developed.

Firstly, the use of a spherical tip aims at looking at the stresses and strain under the indenter during the indentation. It shows that large compressive stresses develop in the aluminum inducing tensile stresses in alumina. The aluminum is in a totally plastic state at a 10% indentation and the plastic equivalent strain tends to concentrate at the interfaces.

Secondly, the use of a Berkovitch tip shows that hardness of the different laminates shows a plateau behavior corresponding to the hardness of the composite. The system with the larger bi-layer thickness and the higher content of alumina shows the highest hardness. Also, the Young modulus value of the different composites for an indentation depth of 10% was calculated, and the value found was between the alumina and aluminum values, and in between the isostress and isostrain models.

Finally, an investigation of the strain-rate sensitivity was done but did not show any relevant results. However, some reviews about the used parameters were made, and a plan for further investigations aiming at having better results is proposed.

To continue this study, as stated in the critics about the models, some refinement of the models should be done. Then, when the models have proven their reliability, some simulation can be run on the model developed at UCLouvain [107] on many systems in order to measure the influence of the bi-layers thickness, of the proportion of alumina, of the top and bottom layers and of the total number of layers on the mechanical properties of Al/Al_2O_3 nanolaminates.

Chapter 6

Conclusions and perspectives

This master thesis aimed at improving the understanding of the tribological and mechanical properties of the nanolaminate Al/Al_2O_3. It had two main objectives: defining the wear resistance of several experimental samples by a scratch test, and characterizing the hardness and Young modulus of these systems through numerical simulation.

As shown in the results and stated several time in this master thesis, the number of samples made and tested was very small due to COVID-19 that put an end to all the experimental work. No sufficient number of variations of the same parameters were studied and no repetition of the experiments have be drawn, so no conclusions can be taken with certainty. Nevertheless, it gives some trends followed by the different systems under specific loads.

Also, the simulations that have been carried out are simple models that do not allow a long-term analysis of the behaviour of nanolaminates. Nevertheless, they give first approximations of hardness and Young modulus, allowing to compare the mechanical properties of the different systems.

The main findings of this master thesis can be summarised as follows:

1. The scratch test performed under specific loading conditions showed that a higher proportion of alumina in a sample leads to a better scratch resistance.

2. SEM observations combined with the scratch test have shown that the failure in the nanolaminates occurs via the fracture of the coating, and that under the specific loading conditions, the adhesion between the layers is good.

3. In order to prepare further erosion tests, the wear volume taken away during scratch was calculated. It confirms the first conclusion, which is that under specific scratch conditions, the less alumina in a sample, the less mater removed during the scratch test, leading to a good wear resistance.

4. During indentation, two different tips were used, to evaluate different phenomena. The spherical tip showed that the compressive stresses were constrained in the aluminum layers and that the alumina layers were under tensile stresses during indentation.

   The test with the Berkovitch tip showed that the hardness of the composite reaches a plateau, at a value in between alumina and aluminum. Also, it shows that the elastic modulus is also in between the individual material values. In these two measures, the samples with a higher alumina value where the ones with a higher hardness and a higher Young modulus.

For all the experiments and simulations realised in this master thesis, alumina outperforms all the hybrids nanolaminates. In fact, it is the material with the higher hardness, the higher Young modulus and the best scratch resistance. It is followed by the sample which has an equal proportion of alumina and aluminum, which shows better properties than the other laminates thanks to its higher alumina content. However, the tests realised in the scope of this master thesis do not give a complete tribological profile of the materials, and the coatings should be tested in other conditions in order to compute their resistance to erosion.

In order to complete and go further than the results obtained in this thesis, the following strategy should be applied to the research. First, some characterization of the deposited sample must be done in order to know the state and the porosity of alumina layers, and the grain size in aluminum layers. Second, some other properties should be measured to complete the characterisation of the materials with a measure of the strength and the ductility through in-situ tensile/compression tests. Finally, with fully characterized sample, the erosion properties can be investigated, and the influence of all the different factors (such as the Young modulus, the ductility, ...) can be characterize in order to have a good understanding of the different erosion phenomena, and to produce coatings that are best suited to their function.

Appendix A

Materials and methods: additional information

A.1 Construction of the tip

In order to maintain a Berkovitch tip behavior while introducing a spherical extremity to allow convergence of the numerical model the idea was to have a radius of 10% of the maximal indentation depth. Also, the spherical tip should be sufficiently noded to avoid discontinuity. So the rounded part of the tip should contain at least 4 elements. This is why the part just under the tip must also have a great node refinement because in Abaqus, during a contact interaction between two surfaces, the top surface (also called master surface) must be less meshed than the bottom surface (slave surface).

The geometry used for this construction and implemented on Abaqus is detailed below.

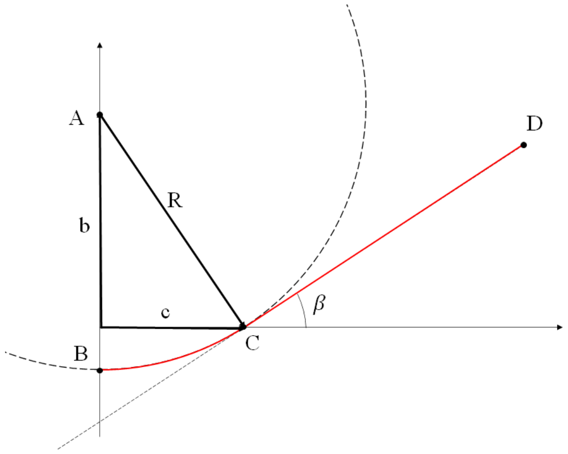

Figure A.1: Construction of the tip in Abaqus CAE

$$R = \frac{c}{sin(\beta)} \tag{A.1}$$

$$b = \frac{c}{tan(\beta)} \tag{A.2}$$

A.2 Standard cleaning

Standard cleaning is a technique used in the clean room in order to clean the silicon substrate so that that they can be used for subsequent applications, i.e. cleaned of all impurities. It takes place in several steps, according to a determined procedure. The substrate is soaked in a reaction of H_2SO_4 and H_2O_2 (to remove the organic residues form the wafers) until the bath temperature reaches 110° C. It is then rinsed with water for 10 minutes. The wafers are then passed through a HF (to remove the native silicone dioxide from wafers) bath for 15 seconds before being rinsed again with water for 5 minutes. After passing through a nitrogen water bath, they are dried in the oven, and are then ready to be used for a deposit.

A.3 Existing samples

Table A.1 lists all the samples which were made by magnetron sputtering. These can be used for further investigations.

Table A.1: Deposited sample by magnetron sputtering, in the purpose of this master thesis

	Deposition date	**Proportion Al_2O_3**	**Al_2O_3 layer**	**Al layer**	**Top layer**
Sample 1	10/02/2020	71,4%	500 nm	200 nm	Al
Sample 2	12/02/2020	28,6%	200 nm	500 nm	Al_2O_3
Sample 3	12/02/2020	28,6%	5 x (40 nm)	5 x (100 nm)	Al_2O_3
Sample 4	14/02/2020	28,6%	5 x (40 nm)	5 x (100 nm)	Al
Sample 5	17/02/2020	71,4%	5 x (100 nm)	5 x (40 nm)	Al_2O_3
Sample 6	17/02/2020	28,6%	10 x (20 nm)	10 x (50 nm)	Al_2O_3
Sample 7	19/02/2020	50%	5 x (70 nm)	5 x (70 nm)	Al_2O_3
Sample 8	24/02/2020	50%	10 x (35 nm)	10 x (35 nm)	Al_2O_3
Sample 9	10/03/20	100%	700 nm		Al_2O_3
Sample 10	09/03/20	33.3%	7x(35nm)	7x (70nm)	Al_2O_3
Sample 11	09/03/20	16.5%	8x(14nm)	8x (70nm)	Al_2O_3

Appendix B

Scratch: additional information

B.1 Raw scratch results

This section presents the raw results as obtained by the scratch test on several samples.

B.1.1 E7070

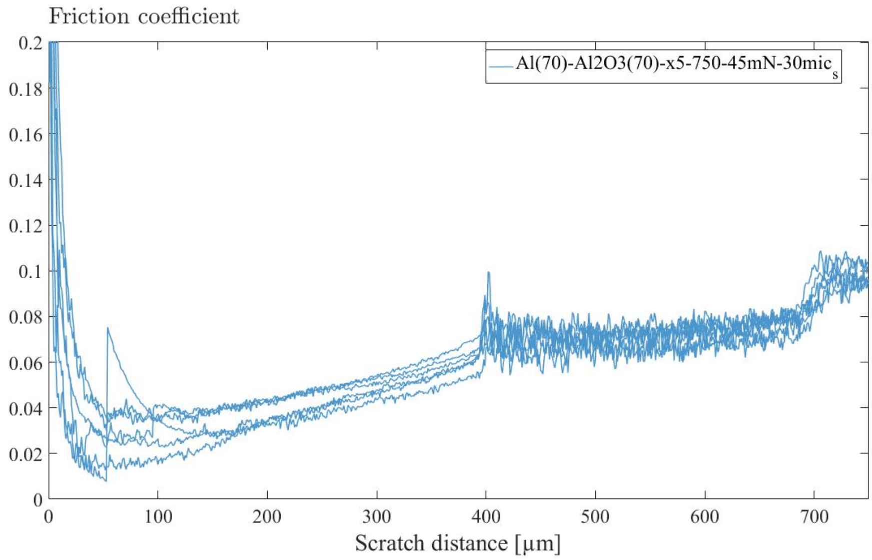

Figure B.1: Evolution of the friction coefficient of E7070 as the scratch distance increases

B.1.2 E3535

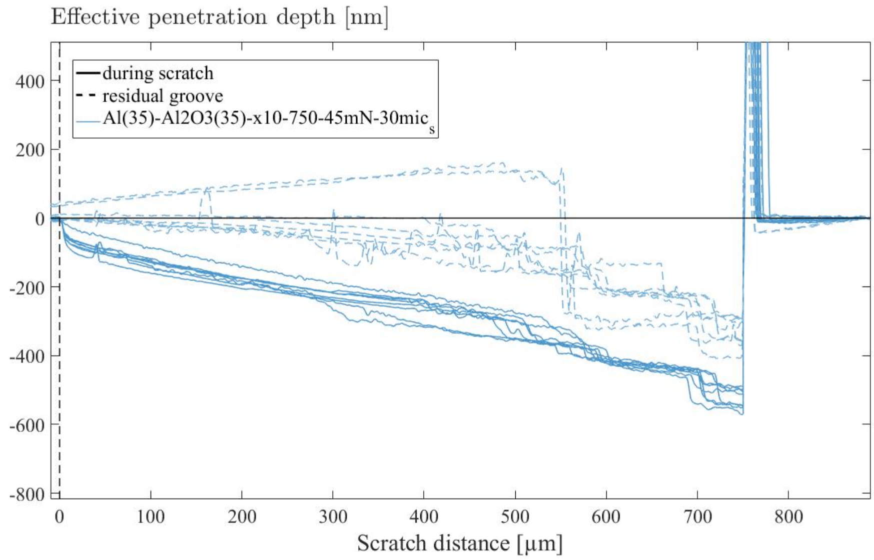

Figure B.2: Effective penetration depth as a function of the scratch distance of sample E3535

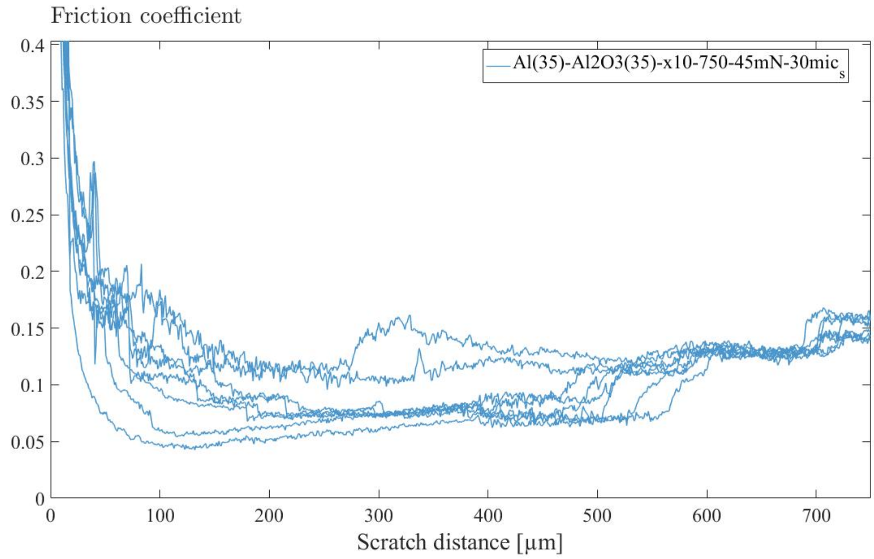

Figure B.3: Evolution of the friction coefficient of E3535 as the scratch distance increases

B.1.3 E7035

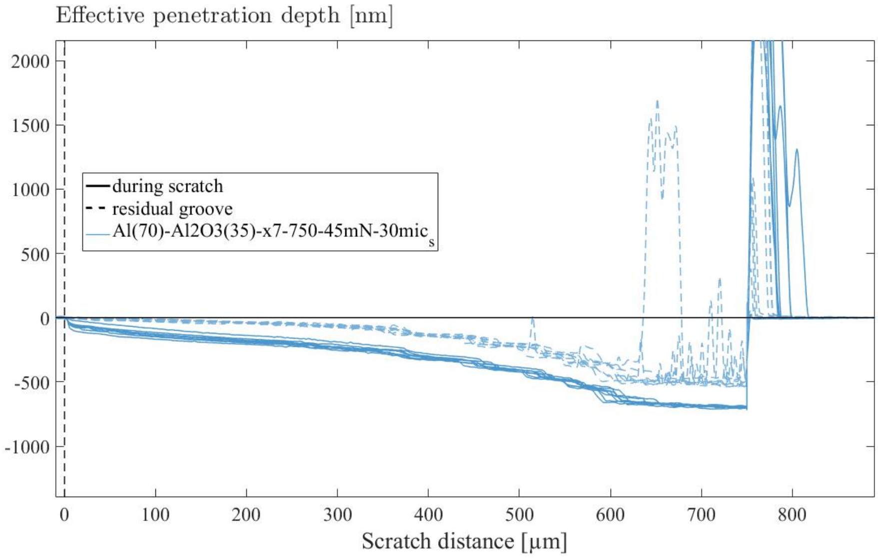

Figure B.4: Effective penetration depth as a function of the scratch distance of sample E7035

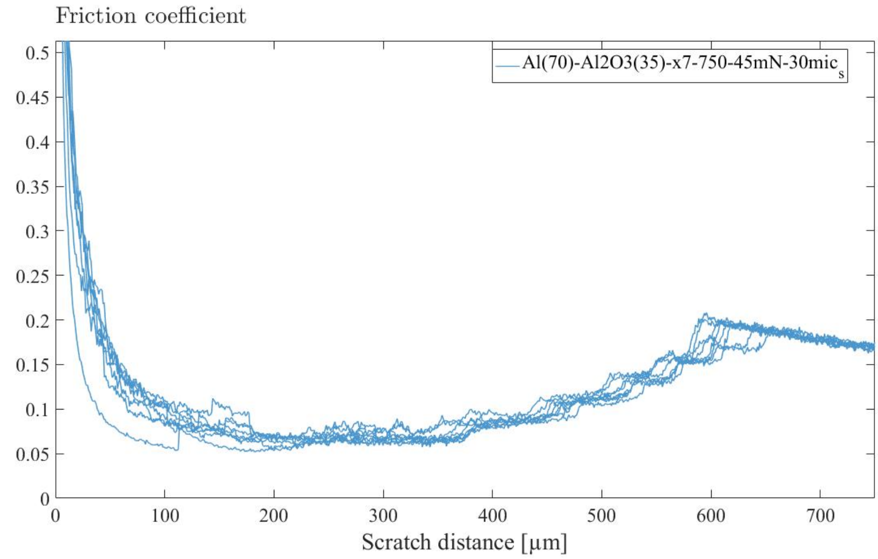

Figure B.5: Evolution of the friction coefficient of E7035 as the scratch distance increases

B.1.4 E7014

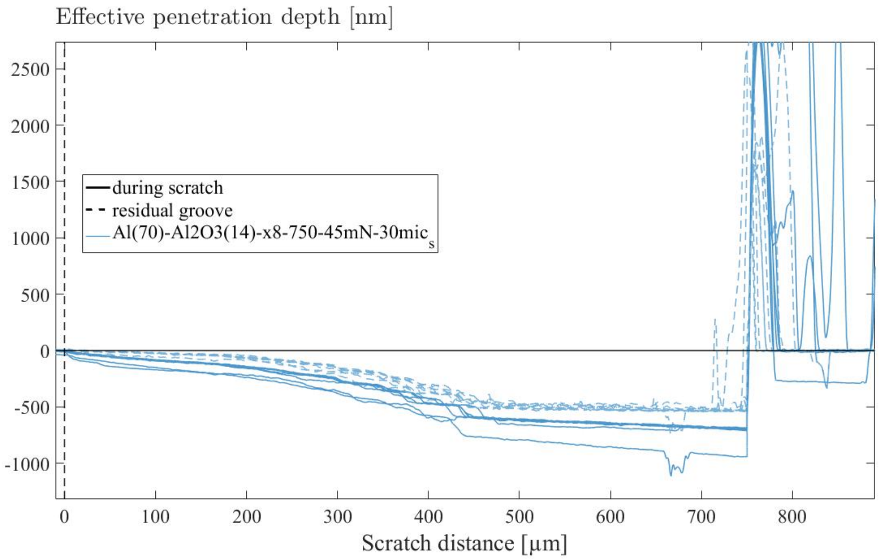

Figure B.6: Effective penetration depth as a function of the scratch distance of sample E7014

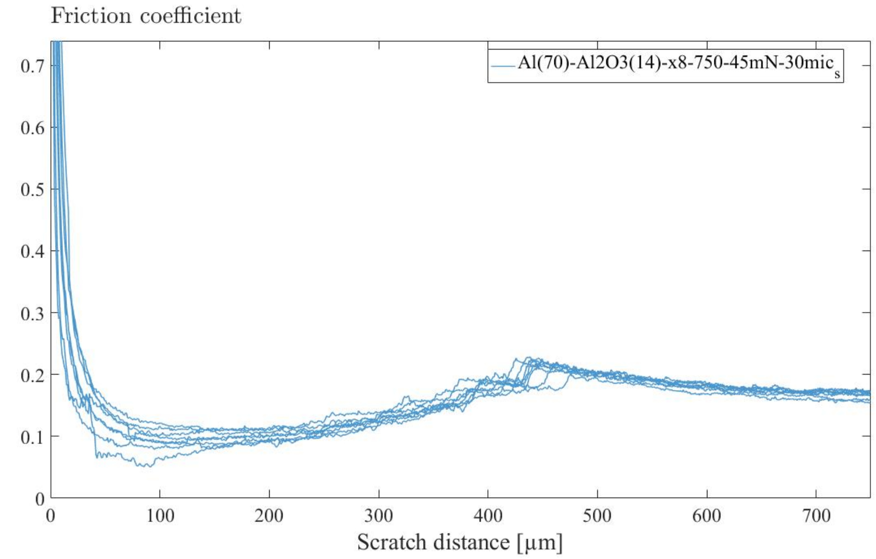

Figure B.7: Evolution of the friction coefficient of E7014 as the scratch distance increases

B.2 Raw SEM pictures

This section presents the SEM pictures as obtained by the scratch test on several samples. It illustrates than the same phenomena take place as in E7070.

The scratches than can be seen in B.8(a), are due to the post-scan of the surface, which may have taken some dust particles with the tip, scratching the surface.

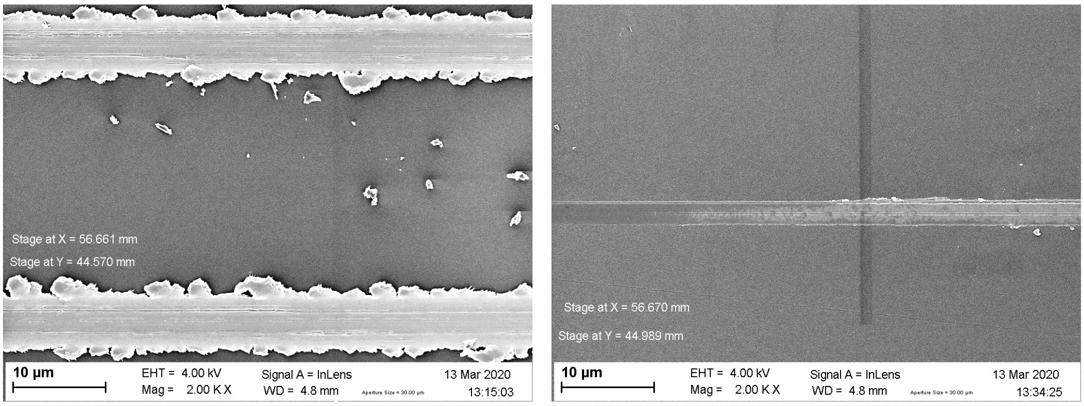

(a) scratches (b) Transition

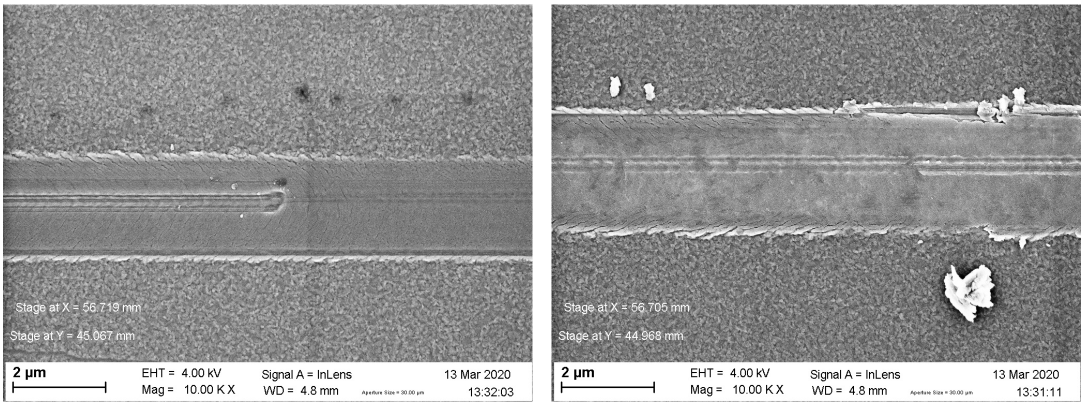

(c) Conformal cracking (d) After transition

Figure B.8: SEM images showing the failure phenomena in E7035

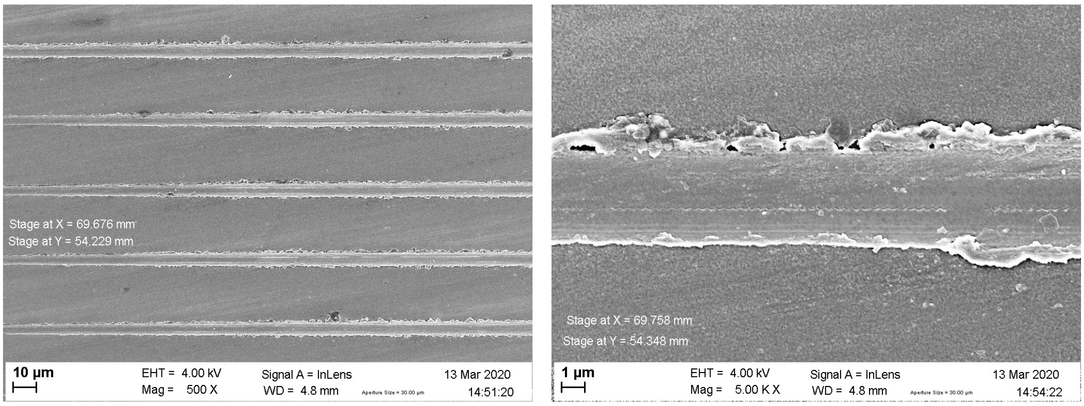

(a) Transition between the two regimes (b) Pile-up on the edges

Figure B.9: SEM images showing the failure phenomena in E7014

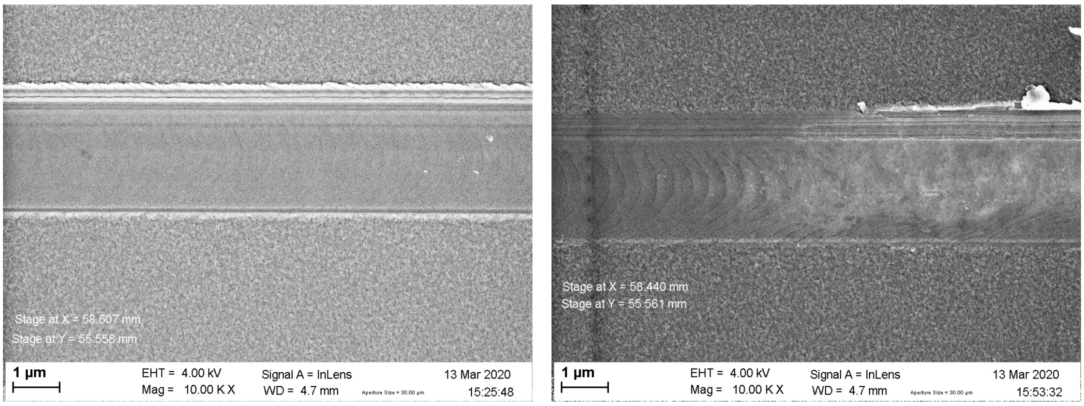

(a) Conformal cracking (b) Transition

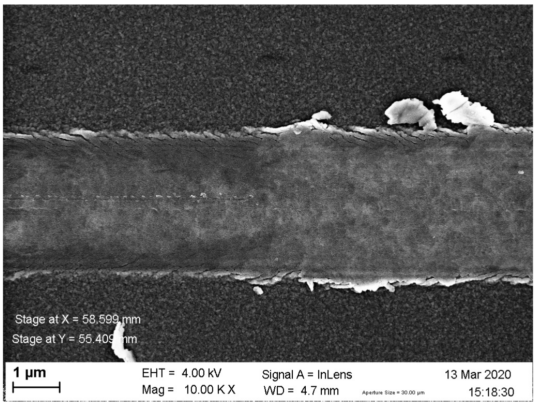

(c) After transition

Figure B.10: SEM images showing the failure phenomena in E3535

B.3 Elastic recovery

Here under are the results of the elastic recovery for different aluminum content and layer thicknesses. Due to offset curves in S3535, the elastic recovery is smoothed and does not show any jumps, leading to a perfect elastic behavior at the beginning of the track. In order to take conclusions of these graphs, further tests should be made.

B.3.0.1 Influence of the aluminum content

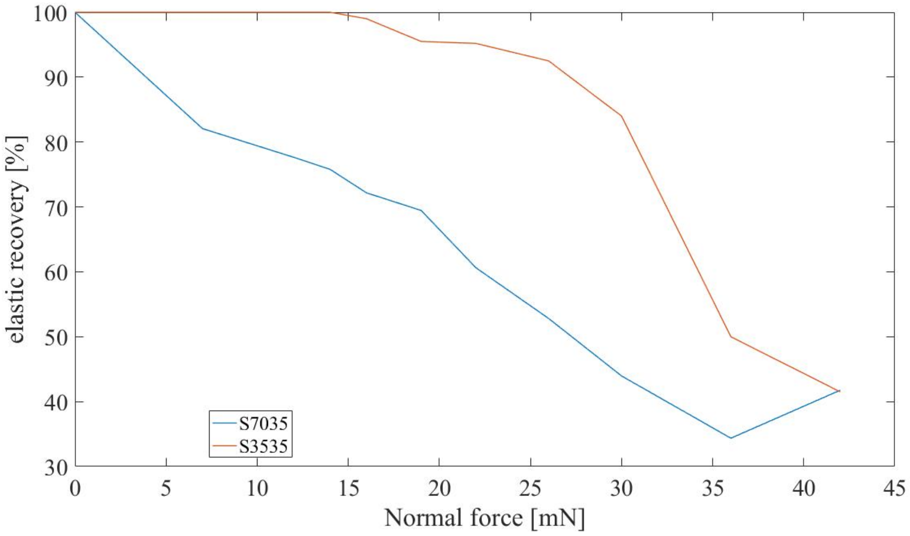

Figure B.11: Elastic recovery vs normal force for different alumina content

B.3.0.2 Influence of the layer thickness

.

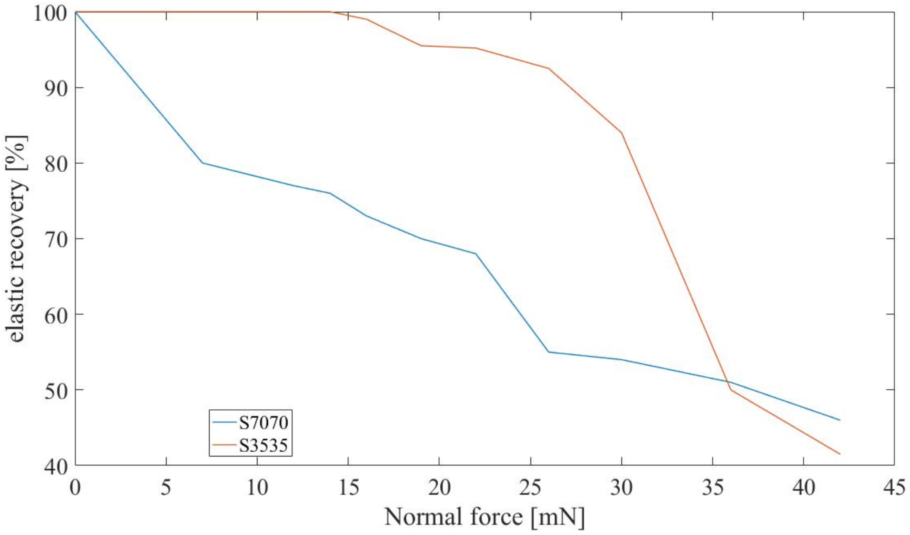

Figure B.12: Elastic recovery vs normal force for different alumina content

Appendix C

Indentation: additional information

C.1 Convergence analysis

C.1.1 Spherical tip - Convergence analysis

Table C.1: Number of nodes in the simulation for a certain minimal size of node x

	x	Total number of nodes
Test 1	0.07	4879
Test 2	0.035	14273
Test 3	0.02	34600
Test 4	0.014	59817
Test 5	0.01	104077
Test 6	0.009	125044
Test 7	0.007	190657
Test 8	0.0065	203732

C.1.2 Contact area calculation

In Abaqus, there is a very easy looking method to measure the contact area between two surfaces. This is called CAREA and is defined in the Abaqus help as "Total area in contact". This value was used at first, some tests were performed to check its value for a spherical model (by calculating with Hertz models, with the area of a spherical cap for a certain height, ...). It did not give any conclusive comparison. This is why, due to the lack of literature and definition of this function, another technique had to be developed.

C.1.3 Indentation S7070 - Berkovitch tip

Figure C.1 shows the experimental indentation made in E7070. The deformation rate was $\dot{\epsilon} = 0.05s^{-1}$.

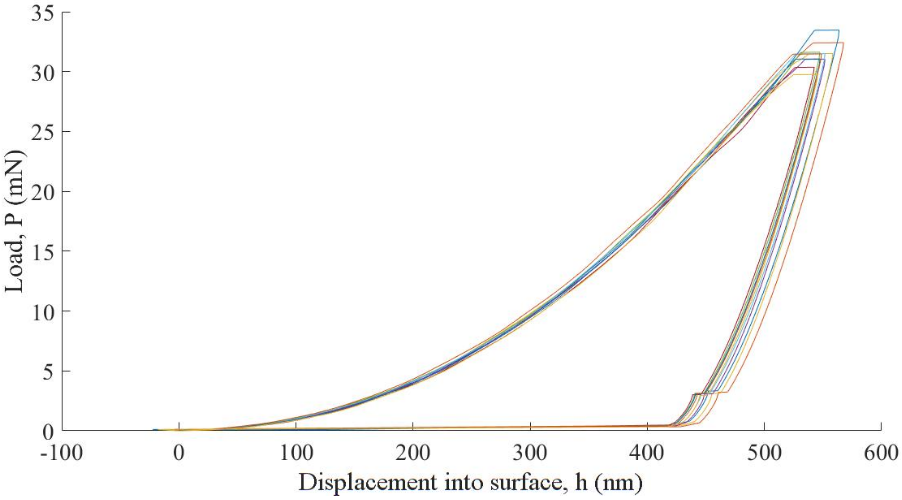

Figure C.1: Indentation of S7070 for a deformation rate of 0.05 s-1. All the values are not perfectly aligned due to experimental imperfections.

C.2 Comparison of the models

This section illustrates that the models constructed with the interface, and the one generating the inp code directly show both the same results.

C.2.1 Spherical analysis

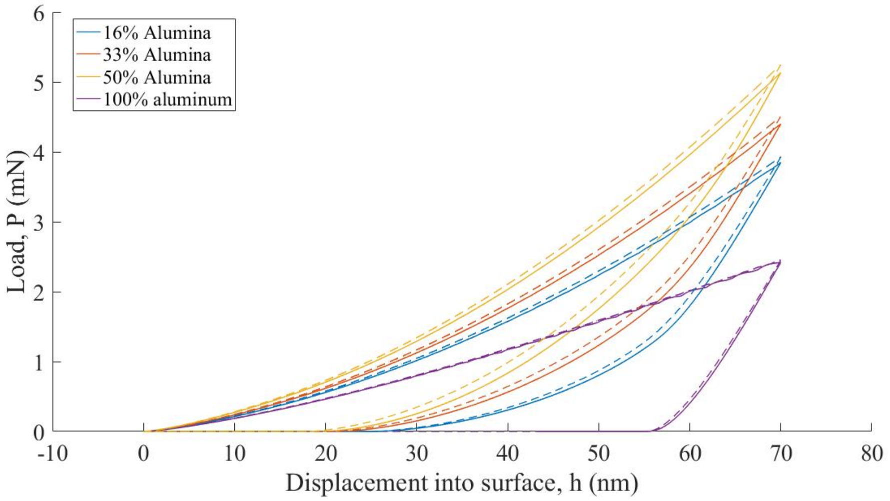

Figure C.2: Comparison of the model made by the graphical interface and the one made by the inp generator showing that the two models used are very similar. The dotted lines represent the INP model while the plain lines represent the CAE model.

C.2.2 Berkovitch analysis

For the Berkovitch analysis, only one model was build. Its results were compared to the INP generated models, and they were similar.

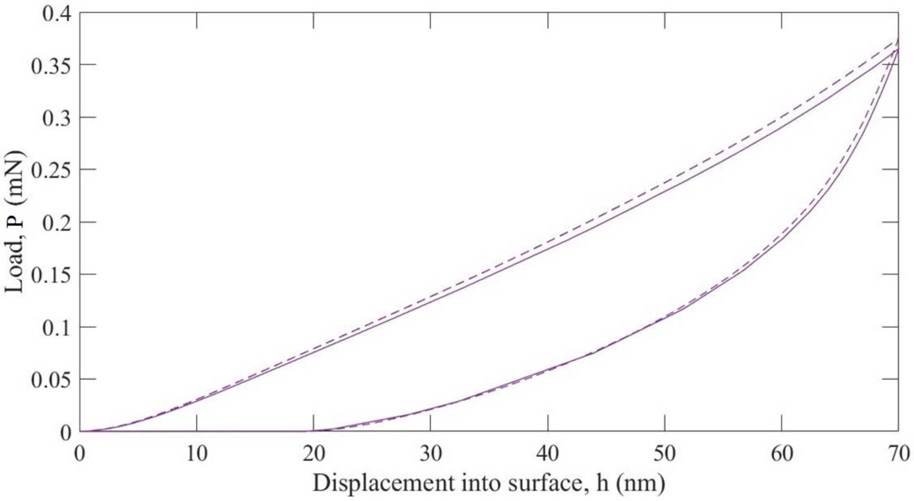

Figure C.3: Comparison of the model made by the graphical interface and the one made by the inp generator showing that the two models used are very similar. The dotted lines represent the INP model while the plain lines represent the CAE model.

C.3 Plateau value of 7070

Figure C.4 illustrates that when going deeper in the material S7070 a plateau value, as in the other laminates is also found. Its value in higher than in the other laminates due to its higher alumina content and to thicker layers.

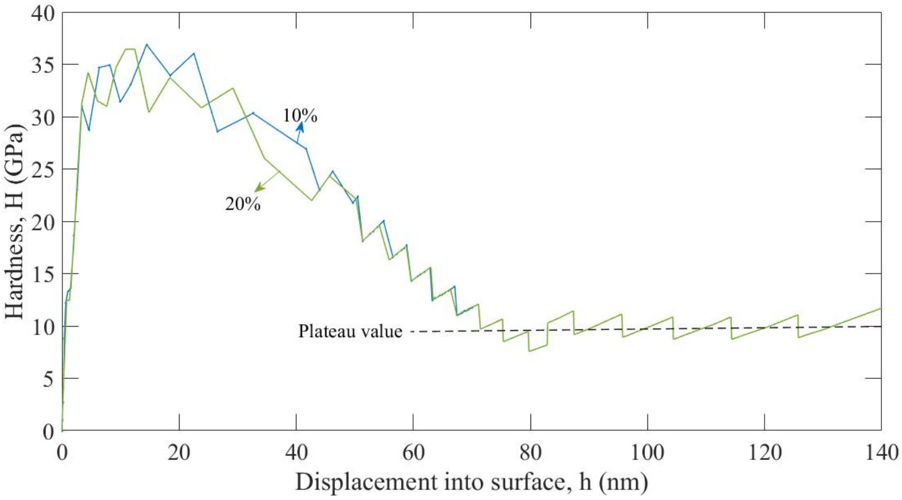

Figure C.4: Indentation in S7070 deeper in the material leading to a plateau value

C.4 Variation of the sphere radius

The figure here-under illustrates the continued growth of the hardness with the penetration depth, showing that no plateau value is reached.

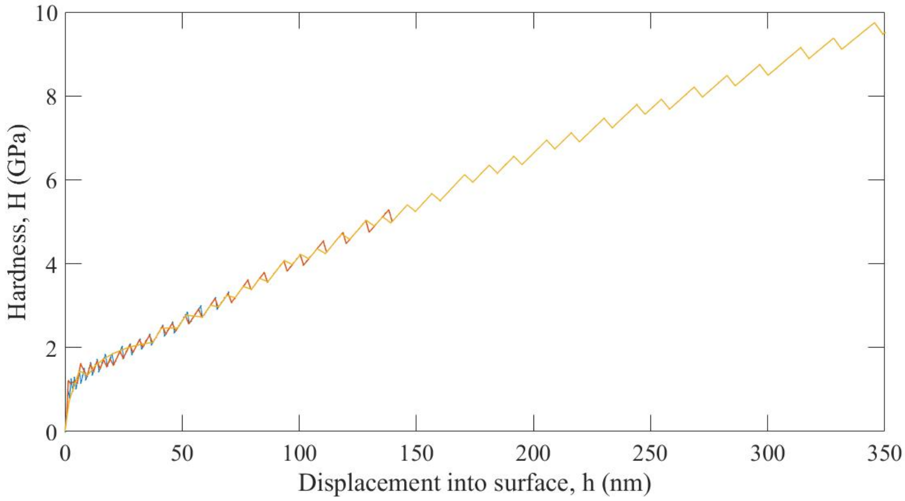

Figure C.5: Hardness vs penetration with several plots for a deeper indentation in the material. The blue line represents 10% of penetration depth, the red line 20% and the yellow line 50%.

The hardness however tends to decrease with smaller indenter tips due to lower contact area. Still, Figure C.6 shows that even with a smaller rounded tip, the hardness does not seem to reach a plateau, therefore a berkovitch tip will be necessary in order to obtain better results. The jumps in the graphs are due to the lack of refinement of the meshing.

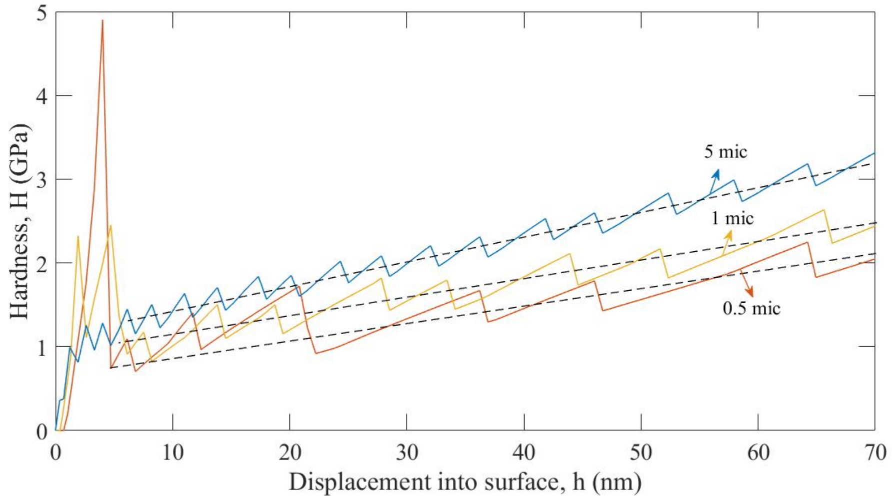

Figure C.6: Evolution of the hardness for several tip radius

C.5 Strain-rate sensitivity

C.5.1 Verification of the model

To prove the functioning of the model, an extreme case was taken: in the Cowper-Symonds model, a D value of 0.81 was taken, and an p value of 2. However, the changes in the results are not that different.

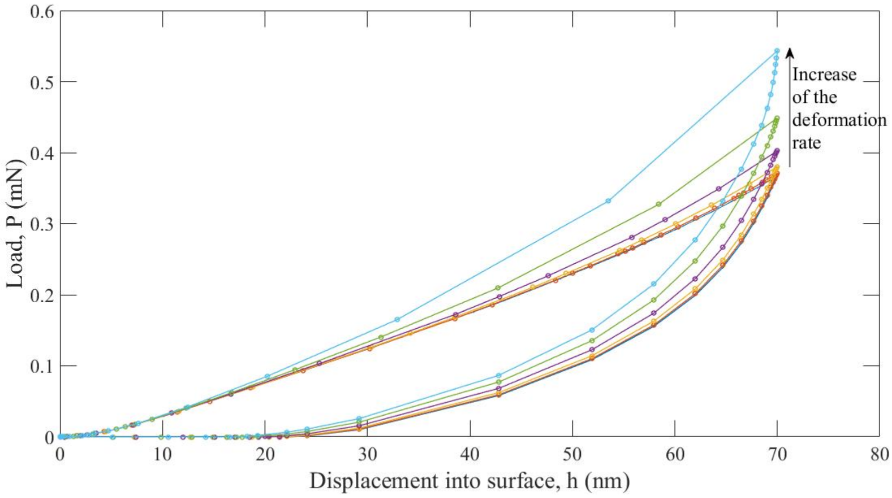

Figure C.7: Evolution load for a test test model to see how the materials and the simulation behave while introducing a sensitivity to the strain-rate

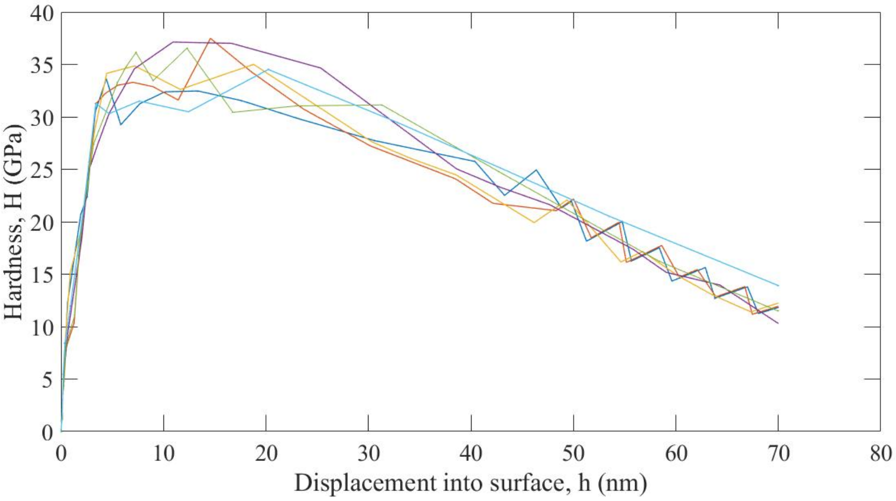

Figure C.8: Hardness of the test model to see how the materials and the simulation behave while introducing a sensitivity to the strain-rate

C.5.2 Real model

Investigation on the real model, showed a small difference in the load P found in indentation. This difference was not observed in the hardness variation. This is due to a too large mesh size, which makes it impossible to see the small differences in contact areas, whereas they are of great importance to see the differences in hardness.

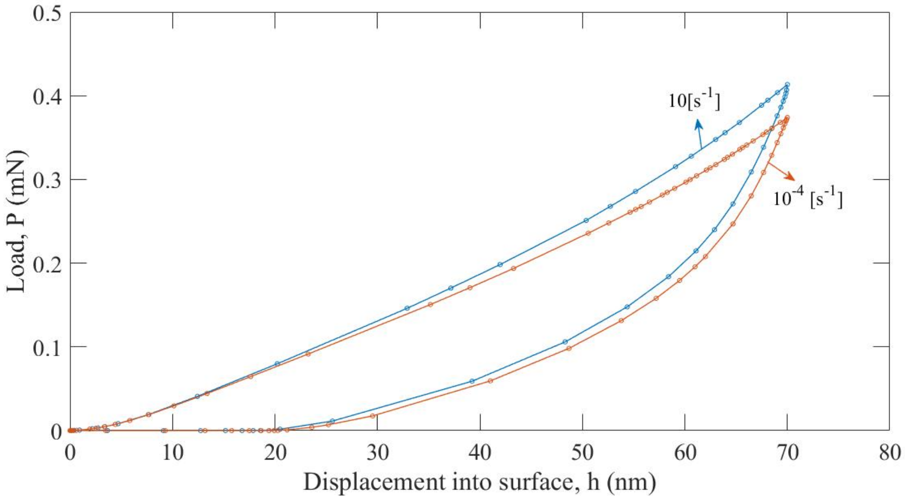

Figure C.9: Evolution of the load for different strain hardening rate

Variations in hardness for different deformation rates in aluminium give very special results. What would be expected is shown at the very beginning of the graph, then the hardness starts to rise in a very unexpected way. This error is surely due to the bad surface refinement which takes into account a too small contact area for a significant increase of the load.

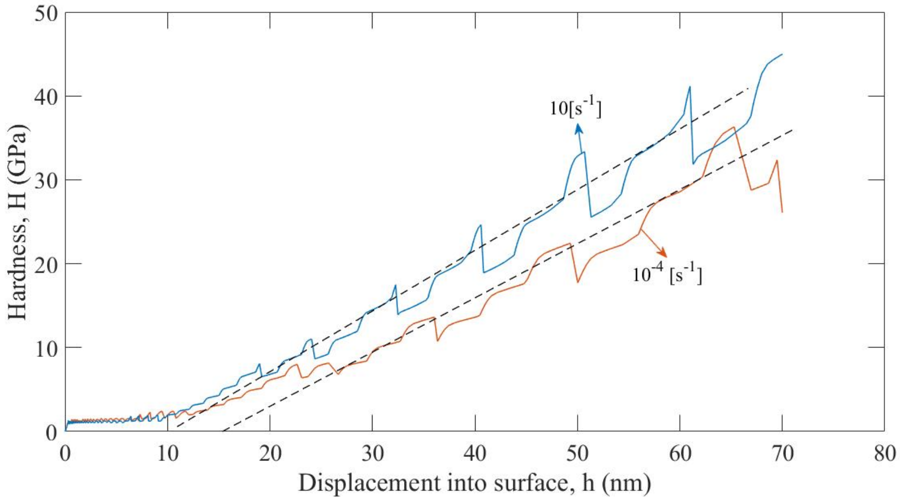

Figure C.10: Evolution of the hardness for different strain hardening rate for pure aluminum

Bibliography

1. Lim, H. & Hoag, S. W. Plasticizer effects on physical–mechanical properties of solvent cast Soluplus® films. *Aaps Pharmscitech* **14,** 903–910 (2013).
2. Holmberg, K. & Matthews, A. *Coatings tribology: properties, mechanisms, techniques and applications in surface engineering* (Elsevier, 2009).
3. Shipway, P. & Hutchings, I. Measurement of coating durability by solid particle erosion. *Surface and Coatings Technology* **71,** 1–8 (1995).
4. Julia-Schmutz, C. & Hintermann, H. Microscratch testing to characterize the adhesion of thin layers. *Surface and Coatings Technology* **48,** 1–6 (1991).
5. Tomastik, J. & Ctvrtlik, R. *Nanoscratch test—A tool for evaluation of cohesive and adhesive properties of thin films and coatings* in *EPJ Web of Conferences* **48** (2013), 00027.
6. Holmberg, K. *et al.* Tribological contact analysis of a rigid ball sliding on a hard coated surface: Part I: Modelling stresses and strains. *Surface and Coatings Technology* **200,** 3793–3809 (2006).
7. Steinmann, P., Tardy, Y. & Hintermann, H. Adhesion testing by the scratch test method: the influence of intrinsic and extrinsic parameters on the critical load. *Thin solid films* **154,** 333–349 (1987).
8. Bull, S. Failure mode maps in the thin film scratch adhesion test. *Tribology international* **30,** 491–498 (1997).
9. Perry, A. Scratch adhesion testing of hard coatings. *Thin solid films* **107,** 167–180 (1983).
10. Friedrich, K. & Schlarb, A. K. *Tribology of polymeric nanocomposites: friction and wear of bulk materials and coatings* (Elsevier, 2011).
11. Burnett, P. & Rickerby, D. The relationship between hardness and scratch adhession. *Thin solid films* **154,** 403–416 (1987).
12. Bull, S. Failure modes in scratch adhesion testing. *Surface and Coatings Technology* **50,** 25–32 (1991).
13. Bull, S. & Berasetegui, E. An overview of the potential of quantitative coating adhesion measurement by scratch testing. *Tribology International* **39,** 99–114 (2006).
14. Holmberg, K. *et al.* Tribological contact analysis of a rigid ball sliding on a hard coated surface: Part II: Material deformations, influence of coating thickness and Young's modulus. *Surface and Coatings Technology* **200,** 3810–3823 (2006).
15. Weil, K., Reimanis, I. & Lewinsohn, C. *Surfaces, Interfaces and Science of Ceramic Joining: Proceedings of the 106th Annual Meeting of The American Ceramic Society, Indianapolis, Indiana, USA 2004* (Wiley, 2012).
16. Bolshakov, A. & Pharr, G. Influences of pileup on the measurement of mechanical properties by load and depth sensing indentation techniques. *Journal of materials research* **13,** 1049–1058 (1998).

17. Baral, P. *Caractérisation mécanique des phénomènes dépendants du temps par nanoindentation instrumentée en température* PhD thesis (2018).
18. Pharr, G., Oliver, W. & Brotzen, F. On the generality of the relationship among contact stiffness, contact area, and elastic modulus during indentation. *Journal of materials research* **7,** 613–617 (1992).
19. Loubet, J., Bauer, M., Tonck, A., Bec, S. & Gauthier-Manuel, B. in *Mechanical Properties and Deformation Behavior of Materials Having Ultra-Fine Microstructures* 429–447 (Springer, 1993).
20. Ashby, M. F. & Cebon, D. Materials selection in mechanical design. *Le Journal de Physique IV* **3,** C7–1 (1993).
21. Oliver, W. C. & Pharr, G. M. An improved technique for determining hardness and elastic modulus using load and displacement sensing indentation experiments. *Journal of materials research* **7,** 1564–1583 (1992).
22. Jamison, R. D. & Shen, Y.-L. Indentation behavior of multilayered thin films: Effects of layer undulation. *Thin solid films* **570,** 235–242 (2014).
23. Hay, J. & Crawford, B. Measuring substrate-independent modulus of thin films. *Journal of Materials Research* **26,** 727–738 (2011).
24. Tang, G. Indentation analysis and mechanical modeling of multilayered composites (2009).
25. Lu, C.-J. & Bogy, D. The effect of tip radius on nano-indentation hardness tests. *International journal of solids and structures* **32,** 1759–1770 (1995).
26. Chen, W., Li, M., Zhang, T., Cheng, Y.-T. & Cheng, C.-M. Influence of indenter tip roundness on hardness behavior in nanoindentation. *Materials Science and Engineering: A* **445,** 323–327 (2007).
27. Králık, V. & Němeček, J. Comparison of nanoindentation techniques for local mechanical quantification of aluminium alloy. *Materials Science and Engineering: A* **618,** 118–128 (2014).
28. Pardoen, T. & Idrissi, H. *Deformation and fracture of materials - Textbook LMAPR2481* UCLouvain - EPL. 2018-2019.
29. Pardoen, T. & Idrissi, H. *Plasticity and metal forming - Textbook LMAPR2482* UCLouvain - EPL. 2018-2019.
30. Pardoen, T. Size and rate dependent necking in thin metallic films. *Journal of the Mechanics and Physics of Solids* **62,** 81–98 (2014).
31. Ritchie, R. O. The conflicts between strength and toughness. *Nature materials* **10,** 817–822 (2011).
32. Ferraro, C. *et al.* Strong and tough metal/ceramic micro-laminates. *Acta Materialia* **144,** 202–215 (2018).
33. Lesuer, D. *et al.* Mechanical behaviour of laminated metal composites. *International Materials Reviews* **41,** 169–197 (1996).
34. Chawla, K. *et al. Deformation mechanisms during indentation of nanoscale metallic/ceramic laminated composites* in *17th International Conference on Composite Materials, ICCM-17* (2009).
35. Tang, G., Singh, D., Shen, Y.-L. & Chawla, N. Elastic properties of metal–ceramic nanolaminates measured by nanoindentation. *Materials Science and Engineering: A* **502,** 79–84 (2009).

36. Bonetti, E., Pasquini, L. & Sampaolesi, E. The influence of grain size on the mechanical properties of nanocrystalline aluminium. *Nanostructured Materials* **9,** 611–614 (1997).
37. Valiev, R. Nanomaterial advantage. *Nature* **419,** 887–889 (2002).
38. Rickerby, D. S. & Matthews, A. *Advanced surface coatings: a handbook of surface engineering* (1991).
39. Wang, J., Zhou, Q., Shao, S. & Misra, A. Strength and plasticity of nanolaminated materials. *Materials Research Letters* **5,** 1–19 (2017).
40. Cordier, P. & Goryaeva, A. *Multiscale Modeling of the Mantle Rheology* 2018.
41. Bonora, N. *Mechanisms of deformation - Lecture 3 (Defects and dislocations)* Università degli studi di cassino e del Lazio Meridionale. 2018.
42. Chen, M. *et al.* Deformation twinning in nanocrystalline aluminum. *Science* **300,** 1275–1277 (2003).
43. Wikipedia. *Grain boundary strengthening* `https://en.wikipedia.org/wiki/Grain_boundary_strengthening`. Last accessed: 2020-16-04.
44. Elango, E. *A study of material Non-linearity during deformation using FEM sofware* PhD thesis (Apr. 2015).
45. Rollett, P. A. & De Graef, M. Microstructure-Properties(1), Materials Properties: Strength, Ductility (2007).
46. Smith, W. F., Hashemi, J. & Presuel-Moreno, F. *Foundations of materials science and engineering* (Mcgraw-Hill Publishing, 2006).
47. Carlton, C. & Ferreira, P. J. What is Behind the Inverse Hall-Petch Behavior in Nanocrystalline Materials? *MRS Proceedings* **976,** 0976–EE01–04 (2006).
48. Pande, C. & Cooper, K. Nanomechanics of Hall–Petch relationship in nanocrystalline materials. *Progress in Materials Science* **54,** 689–706 (2009).
49. Song, H., Guo, S. & Hu, Z. A coherent polycrystal model for the inverse Hall-Petch relation in nanocrystalline materials. *Nanostructured Materials* **11,** 203–210 (1999).
50. Carsley, J., Ning, J., Milligan, W., Hackney, S. & Aifantis, E. A simple, mixtures-based model for the grain size dependence of strength in nanophase metals. *Nanostructured Materials* **5,** 441–448 (1995).
51. Cavaliere, P. Mechanical properties of nanocrystalline materials. *Handbook of Mechanical Nanostructuring,* 1–16 (2015).
52. Koch, C. Optimization of strength and ductility in nanocrystalline and ultrafine grained metals. *Scripta Materialia* **49,** 657–662 (2003).
53. Yip, S. The strongest size. *Nature* **391,** 532–533 (1998).
54. Tian, L. & Li, L. A review on the strengthening of nanostructured materials. *International Journal of Current Engineering and Technology* **8** (2018).
55. Lim, Y. Y. & Chaudhri, M. M. The influence of grain size on the indentation hardness of high-purity copper and aluminium. *Philosophical Magazine A* **82,** 2071–2080 (2002).
56. Qi, Z. *et al.* The inverse Hall–Petch effect in nanocrystalline ZrN coatings. *Surface and Coatings Technology* **205,** 3692–3697 (2011).
57. Wang, Y. & Ma, E. Strain hardening, strain rate sensitivity, and ductility of nanostructured metals. *Materials Science and Engineering: A* **375,** 46–52 (2004).

58. Pardoen, T. *et al. Ductility of thin metallic films* in *Materials Science Forum* **633** (2010), 615–635.

59. Chen, M. Mechanical behavior of metallic glasses: microscopic understanding of strength and ductility. *Annu. Rev. Mater. Res.* **38,** 445–469 (2008).

60. Park, E. S. Understanding of the shear bands in amorphous metals. *Applied Microscopy* **45,** 63–73 (2015).

61. Argon, A. Plastic deformation in metallic glasses. *Acta metall.* **27,** 47–58 (1979).

62. Wang, Y., Li, J., Hamza, A. V. & Barbee, T. W. Ductile crystalline–amorphous nanolaminates. *Proceedings of the National Academy of Sciences* **104,** 11155–11160 (2007).

63. Jang, D. & Greer, J. R. Transition from a strong-yet-brittle to a stronger-and-ductile state by size reduction of metallic glasses. *Nature materials* **9,** 215–219 (2010).

64. Fan, Z. *et al.* "Ductile" fracture of metallic glass nanolaminates. *Advanced Materials Interfaces* **4,** 1700510 (2017).

65. Guo, H. *et al.* Tensile ductility and necking of metallic glass. *Nature materials* **6,** 735–739 (2007).

66. Greer, A., Cheng, Y. & Ma, E. Shear bands in metallic glasses. *Materials Science and Engineering: R: Reports* **74,** 71–132 (2013).

67. Deng, X., Chawla, N., Chawla, K. K., Koopman, M. & Chu, J. P. Mechanical behavior of multilayered nanoscale metal-ceramic composites. *Advanced Engineering Materials* **7,** 1099–1108 (2005).

68. Misra, A. & Hoagland, R. Plastic flow stability of metallic nanolaminate composites. *Journal of materials science* **42,** 1765–1771 (2007).

69. Sun, N., Wang, S., Silva, T. & Kos, A. B. High-frequency behavior and damping of Fe-Co-N-based high-saturation soft magnetic films. *IEEE transactions on magnetics* **38,** 146–150 (2002).

70. Yao, S.-H., Kao, W.-H., Su, Y.-L. & Liu, T.-H. On the tribology and micro-drilling performance of TiN/AlN nanolayer coatings. *Materials Science and Engineering: A* **386,** 149–155 (2004).

71. Larsson, M., Bromark, M., Hedenqvist, P. & Hogmark, S. Mechanical and tribological properties of multilayered PVD TiN/NbN coatings. *Surface and Coatings Technology* **91,** 43–49 (1997).

72. Abboud, M., Motallebzadeh, A., Verma, N. & Özerinç, S. Nanoscratch Behavior of Metallic Glass/Crystalline Nanolayered Composites. *JOM* **71,** 593–601 (2019).

73. Hwu, K. & Derby, B. Fracture of metal/ceramic laminates—II. Crack growth resistance and toughness. *Acta materialia* **47,** 545–563 (1999).

74. Sha, Z.-D., Branicio, P. S., Lee, H. P. & Tay, T. E. Strong and ductile nanolaminate composites combining metallic glasses and nanoglasses. *International Journal of Plasticity* **90,** 231–241 (2017).

75. Pardoen, T. & Lucas, S. Tough hybrid nanolaminates: research project". *FNRS* (2018).

76. Ma, Y., Peng, G., Chen, H., Jiang, W. & Zhang, T. On the nanoindentation hardness of Cu-Zr-Al/Cu nanolaminates. *Journal of Non-Crystalline Solids* **482,** 208–212 (2018).

77. Mearini, G. & Hoffman, R. Tensile properties of aluminum/alumina multi-layered thin films. *Journal of electronic materials* **22,** 623–629 (1993).

78. Deng, X. *et al.* Nanoindentation behavior of nanolayered metal-ceramic composites. *Journal of Materials Engineering and Performance* **14,** 417–423 (2005).

79. Leng, Y. & Courtney, T. Fracture behavior of laminated metal-metallic glass composites. *Metallurgical transactions A* **21,** 2159–2168 (1990).

80. Ritchie, R. O. Mechanisms of fatigue-crack propagation in ductile and brittle solids. *International journal of Fracture* **100,** 55–83 (1999).

81. Wiklund, U., Hedenqvist, P. & Hogmark, S. Multilayer cracking resistance in bending. *Surface and Coatings Technology* **97,** 773–778 (1997).

82. Berger, M., Wiklund, U., Eriksson, M., Engqvist, H. & Jacobson, S. The multilayer effect in abrasion—optimising the combination of hard and tough phases. *Surface and Coatings Technology* **116,** 1138–1144 (1999).

83. Axen, N. & Jacobson, S. A model for the abrasive wear resistance of multiphase materials. *Wear* **174,** 187–199 (1994).

84. Axén, N., Jacobson, S. & Hogmark, S. Principles for the tribological evaluation of intrinsic coating properties. *wear* **203,** 637–641 (1997).

85. Barnett, S. *Nanolayered hard coatings for high-temperature applications* in *Society of Vacuum Coaters 45 th Annual Technical Conference, Lake Buena Vista* (2002), 59–63.

86. Voevodin, A. & Zabinski, J. Superhard, functionally gradient, nanolayered and nanocomposite diamond-like carbon coatings for wear protection. *Diamond and Related Materials* **7,** 463–467 (1998).

87. Larsson, M., Bromark, M., Hedenqvist, P. & Hogmark, S. Deposition and mechanical properties of multilayered PVD Ti- TiN coatings. *Surface and Coatings Technology* **76,** 202–205 (1995).

88. Alpas, A., Embury, J., Hardwick, D. & Springer, R. The mechanical properties of laminated microscale composites of Al/Al 2 O 3. *Journal of Materials Science* **25,** 1603–1609 (1990).

89. Mercier, D. *et al.* Investigation of the fracture of very thin amorphous alumina film during spherical nanoindentation. *Thin Solid Films* **638,** 34–47 (2017).

90. Northwood, D. & Alpas, A. Mechanical and tribological properties of nanocrystalline and nanolaminated surface coatings. *Nanostructured materials* **10,** 777–793 (1998).

91. Koski, K., Hölsä, J. & Juliet, P. Voltage controlled reactive sputtering process for aluminium oxide thin films. *Thin Solid Films* **326,** 189–193 (1998).

92. Ko, S. *et al.* Mechanical properties and residual stress in porous anodic alumina structures. *Thin solid films* **515,** 1932–1937 (2006).

93. Asmani, M., Kermel, C., Leriche, A. & Ourak, M. Influence of porosity on Young's modulus and Poisson's ratio in alumina ceramics. *Journal of the European ceramic society* **21,** 1081–1086 (2001).

94. Spriggs, R. Expression for effect of porosity on elastic modulus of polycrystalline refractory materials, particularly aluminum oxide. *Journal of the American Ceramic Society* **44,** 628–629 (1961).

95. Knudsen, F. Effect of porosity on Young's modulus of alumina. *Journal of the American Ceramic Society* **45,** 94–95 (1962).

96. Van der Rest, A. *et al.* Mechanical behavior of ultrathin sputter deposited porous amorphous Al2O3 films. *Acta Materialia* **125,** 27–37 (2017).

97. Shi, F. in *Magnetron Sputtering* (IntechOpen, 2018).

98. Tuyaerts, R. Internal stress and opto-electronic properties of pure and Al-doped ZnO thin films deposited by reactive sputtering.

99. Materials, P. H. P. *Coating - How the PVD sputtering process works* `https://www.youtube.com/watch?v=8mVK5dwyoEY`. Last accessed: 2020-12-05.

100. Wuhrer, R. & Yeung, W. Grain refinement with increasing magnetron discharge power in sputter deposition of nanostructured titanium aluminium nitride coatings. *Scripta Materialia* **50,** 813–818 (2004).

101. Koski, K., Hölsä, J. & Juliet, P. Properties of aluminium oxide thin films deposited by reactive magnetron sputtering. *Thin Solid Films* **339,** 240–248 (1999).

102. Koski, K., Hölsä, J. & Juliet, P. Deposition of aluminium oxide thin films by reactive magnetron sputtering. *Surface and Coatings Technology* **116,** 716–720 (1999).

103. Ding, Y., Northwood, D. & Alpas, A. Fabrication of microlaminated Al/Al2O3 composites by magnetron sputtering for tribological applications. *Surface and Coatings Technology* **62,** 448–453 (1993).

104. Huang, L.-Y., Xu, K.-W. & Lu, J. Evaluation of scratch resistance of diamond-like carbon films on Ti alloy substrate by nano-scratch technique. *Diamond and related materials* **11,** 1505–1510 (2002).

105. Of Cambridge, U. *The Scanning Electron Microscope (SEM)* `https://www.eng-atoms.msm.cam.ac.uk/RoyalSocDemos/SEM`. Last accessed: 2020-13-05.

106. Ul-Hamid, A. *A Beginners' Guide to Scanning Electron Microscopy* (Springer, 2018).

107. Baral, P. *Model under developpement* UCLouvain. 2020.

108. Lide, D. R. *CRC handbook of chemistry and physics: a ready-reference book of chemical and physical data* (CRC press, 1995).

109. *MEMSnet* `https://www.memsnet.org/material`. Last accessed: 2020-08-05.

110. *MatWeb: Your Source for Materials Information* `http://www.matweb.com`. Last accessed: 2020-08-05.

111. Wang, M. & Shan, A. Effect of strain rate on the tensile behavior of ultra-fine grained pure aluminum. *Journal of alloys and compounds* **455,** L10–L14 (2008).

112. Wong, W., Gupta, M. & Lim, C. Enhancing the mechanical properties of pure aluminum using hybrid reinforcement methodology. *Materials Science and Engineering: A* **423,** 148–152 (2006).

113. Read, D. T. & Dally, J. W. Mechanical behavior of aluminum and copper thin films. *Asme-Applied Mechanics division* **187,** 41–41 (1994).

114. Auerkari, P. *Mechanical and physical properties of engineering alumina ceramics* (Technical Research Centre of Finland Espoo, 1996).

115. Shackelford, J. F., Han, Y.-H., Kim, S. & Kwon, S.-H. *CRC materials science and engineering handbook* (CRC press, 2016).

116. Wang, H. *Internal communication* UCLouvain. 2020.

117. Cowper, G. R. & Symonds, P. S. *Strain-hardening and strain-rate effects in the impact loading of cantilever beams* tech. rep. (Brown Univ Providence Ri, 1957).

118. Yamada, H., Hotta, M., Kami, T., Ogasawara, N. & Chen, X. *Effect of dynamic strain rate on micro-indentation properties of pure aluminum* in *EPJ Web of Conferences* **94** (2015).

119. Zok, F. & Miserez, A. Property maps for abrasion resistance of materials. *Acta materialia* **55,** 6365–6371 (2007).

120. Meyers, M. A., Mishra, A. & Benson, D. J. Mechanical properties of nanocrystalline materials. *Progress in materials science* **51,** 427–556 (2006).

121. Singh, D. R. & Chawla, N. Scratch resistance of Al/SiC metal/ceramic nanolaminates. *Journal of Materials Research* **27,** 278–283 (2012).

122. Puricelli, L., Galluzzi, M., Schulte, C., Podestà, A. & Milani, P. Nanomechanical and topographical imaging of living cells by atomic force microscopy with colloidal probes. *Review of Scientific Instruments* **86,** 033705 (2015).

123. Johnson, K. Contact mechanics cambridge univ. *Press, Cambridge* **95,** 365 (1985).

124. Zhang, J. *et al.* Mechanical properties of crystalline Cu/Zr and crystal–amorphous Cu/Cu–Zr multilayers. *Materials Science and Engineering: A* **552,** 392–398 (2012).

125. Mayer, C. *et al.* Orientation dependence of indentation behavior in Al–SiC nanolaminate composites. *Materials Letters* **168,** 129–133 (2016).

UNIVERSITÉ CATHOLIQUE DE LOUVAIN
École polytechnique de Louvain
Rue Archimède, 1 bte L6.11.01, 1348 Louvain-la-Neuve, Belgique | **www.uclouvain.be/epl**